CDT
Centre de Développement Technologique
École Polytechnique de Montréal

CORROSION-FATIGUE OF Mn-Ni-Al BRONZE PROPELLER ALLOYS

FINAL REPORT

by:

Ivan Dickson, Louis Handfield,
Serge Lalonde, Yves Blanchette and Jean-Paul Baïlon
Department of Metallurgical Engineering
ECOLE POLYTECHNIQUE DE MONTREAL

Work on this project was conducted under the auspices of
Physical Metallurgy Research Laboratories
Canada Centre for Mineral and Energy Technology
Energy, Mines and Resources Canada

DSS FILE NUMBER	:	03SQ.23440-2-9017
DSS CONTRACT SERIAL NUMBER	:	0SQ82-00189
CANMET PROJECT NUMBER	:	420251
CANMET SCIENTIFIC AUTHORITY	:	Dr. M. Sahoo

March 1985

102 pp.

MICROMEDIA

This report should be cited by D.S.S.
File no. 03SQ.23440-2-9017

CDT
Centre de
Développement
Technologique
École Polytechnique
de Montréal

TABLE OF CONTENTS

		Page
LIST OF FIGURES		ii
SUMMARY		1
1.	INTRODUCTION	3
2.	EXPERIMENTAL PROCEDURE	4
3.	RESULTS	5
3.1	Microstructures	5
3.2	Crack growth as a function of ΔK	6
3.3	Crack growth as a function of ΔK_{eff}	18
3.4	Threshold values	23
3.5	Fractographic observations	25
3.6	Metallographic observations of crack paths	36
3.7	Influence of β-grain boundaries in HT material as observed by metallography	44
3.8	Secondary cracking in the near-threshold region, HT material	46
4.	DISCUSSION	49
4.1	Influence of alloy condition on crack propagation curves in air	49
4.2	Fatigue crack propagation in the 3.5% NaCl solution	51
4.3	The influence of the R-ratio and crack growth as a function of ΔK_{eff}	52
4.4	Corrosion-fatigue mechanism	53
4.5	Threshold values	54
4.6	Oscillations in the log da/dN vs log ΔK curves	57
4.7	The influence of the Mn content	58
5.	CONCLUSIONS	59
ACKNOWLEDGMENTS		62
REFERENCES		63
APPENDIX		64

LIST OF FIGURES

Page

FIGURE 1: Microstructure of the 14% Mn AC alloy. The size of the β-grains can be seen by the band of white α-grains at their boundaries. Mag 100X 7

FIGURE 2: Microstructure of the 12% Mn NSC alloy. The black particles correspond to the iron-rich precipitates. 100 X 7

FIGURE 3: Microstructure of the 14% Mn HT alloy. The amount of β-phase is sufficiently important that the boundaries between β-grains can be distinguished using polarized illumination. 100 X 8

FIGURE 4: Crack growth results obtained for the 12% Mn AC alloy 10

FIGURE 5: Crack growth results obtained for the 14% Mn AC alloy 10

FIGURE 6: Crack growth results obtained for the 12% Mn NSC alloy 12

FIGURE 7: Crack growth obtained for the 14% Mn NSC alloy 12

FIGURE 8: Comparison of some crack growth curves for the NSC and AC alloys 14

FIGURE 9: Crack growth results obtained in air for the 12% Mn HT alloy 14

FIGURE 10: Crack growth results obtained in 3.5% NaCl solution for the 12% Mn HT alloy 16

FIGURE 11: Crack growth results obtained for the 14% Mn HT alloy 16

FIGURE 12: Comparison of some crack growth curves for the HT and NSC alloys 19

FIGURE 13: Crack growth rates as a function of ΔK_{eff} for the tests performed in air on the AC and NSC materials ... 19

LIST OF FIGURES

Page

FIGURE 14: Crack growth rates as a function of ΔK_{eff} for the AC materials tested in the 3.5% NaCl solution 22

FIGURE 15: Crack growth rates as a function of ΔK_{eff} for the NSC materials tested in 3.5% NaCl solution 22

FIGURE 16: Crack growth rates as a function of ΔK_{eff} for the tests performed in air on the HT materials 24

FIGURE 17: Crack growth rates as a function of ΔK_{eff} for the tests performed in 3.5% NaCl solution on the HT materials 24

FIGURE 18: Sharp transition in appearance of fracture surface produced on the 12% NSC alloy tested in 3.5% NaCl solution after ultrasonic cleaning 29

FIGURE 19: The sharp transition on Fig. 18 also corresponds to a sharp decrease in the number of finer macroscopic river or ridge lines on the fracture surface 29

FIGURE 20: Macroscopic aspect of the fracture surface produced on 12% Mn HT alloy tested in air (lower specimen) and in 3.5% NaCl solution (upper specimen) 31

FIGURE 21: Ductile striations at high growth rates in the 12% Mn AC alloy tested in air. Crack propagation proceeds in a straightforward fashion from α-grain to α-grain. The macroscopic propagation direction is indicated by a large arrow 31

FIGURE 22: Ductile striations at high growth rates in the 12% Mn NSC alloy tested in 3.5% NaCl solution. Fine slots at the α-β boundaries proceed ahead of the macroscopic crack front. As a result, the local propagation directions (small arrows) in the α-grains can even propagate back towards the macroscopic crack front 32

LIST OF FIGURES

Page

FIGURE 23: Effect of slotting at α-β interfaces on initiating cracking in α-grains ahead of the macroscopic crack front in 12% Mn NSC alloy tested in 3.5% NaCl 32

FIGURE 24: Bypassed α-grain by the faster crack propagation in the β-phase for the 14% Mn HT alloy tested in air. Local propagaion directions in an α-grain are indicated by small arrows 35

FIGURE 25: Variable interstriation spacings observed at high growth rates on a β-microfacet for the 14% Mn HT alloy tested in air. The interstriation spacing is largest towards the center of the microfacet 35

FIGURE 26: Microfractographic aspect of the 12% Mn HT alloy tested in air. Many of the β-microfacets present only fine river lines. Some of the α-grains, which occur as round islands within the β-matrix, can be easily recognized. The lateral propagation in these α-grains indicates that the microscopic crack front leads in the flat β-microfacets 37

FIGURE 27: Flattened ductile striations observed for the higher growth rates in the 14% Mn HT alloy tested in 3.5% NaCl solution. The microstructure has little influence on the local crack growth 37

FIGURE 28: Slots (small arrows) at α-β interfaces seen on the profile of the crack surface, 12% NSC alloy tested in the 3.5% NaCl solution, R = 0.1, f = 20 Hz 39

FIGURE 29: Large and fine secondary cracks observed on the 12% Mn HT alloy tested in air. The devious aspect of the crack path is seen. Some of the fine cracks stop on meeting α-grains, go along α-β interfaces and along interfaces with blackish particles. 100 X 39

FIGURE 30: Aspects of the path of a secondary crack in 14% Mn HT bronze tested in air. Sections of the crack path in the β-phase tend to be parallel to two orientations of elongated α-grains. 50 X 40

LIST OF FIGURES

Page

FIGURE 31: Details of the path of a secondary crack in 12% Mn HT bronze tested in air 40

FIGURE 32: End of a secondary crack in 12% Mn HT bronze tested in air. Each of two crack branches terminates on meeting an α-grain. The crack in the β-phase is generally parallel to one of the orientations of elongated α-grains. 100 X 42

FIGURE 33: Relatively straight secondary cracks parallel to three orientations of elongated α-grains in 12% Mn HT alloy tested in 3.5% NaCl solution (f = 20 Hz, R = 0.1). 50 X 42

FIGURE 34: Secondary crack in 14% Mn HT alloy tested in air parallel to the profile of the crack surface. The secondary crack terminates soon after crossing a β-grain boundary. 50 X 43

FIGURE 35: Relatively straight secondary crack parallel to crack surface profile and to one orientation of elongated α-grains in 14% Mn HT alloy tested in 3.5% NaCl solution (f = 20 Hz, R = 0.1). The crack deviates only slightly on meeting α-grains except when it meets several closely spaced α-grains. 64 X 43

FIGURE 36: Secondary cracks observed in 14% Mn HT alloy tested in 3.5% NaCl solution (f = 20 Hz, R = 0.1) parallel to two orientations of elongated α-grains, although few elongated grains are found for one of these orientations. One of the secondary cracks can be seen to terminate on meeting an α-grain at a β-grain boundary. 100 X 45

FIGURE 37: Deviation of the crack surface profile and crack branching at a β-grain boundary in the 12% Mn HT alloy tested in 3.5% NaCl solution 45

FIGURE 38: Extensive crack branching near the crack surface in the threshold region of the 12% Mn HT alloy tested in the 3.5% NaCl solution 47

LIST OF FIGURES

Page

FIGURE 39: Extensive crack branching in the region of a crack surface deviation within a β-grain, 12% Mn HT alloy tested in 3.5% NaCl solution. The secondary cracks in the β-phase and the profile of the cracks surface are parallel to the orientations of elongated α-grains 47

FIGURE 40: Slip traces produced in an α-grain by microhardness indentations are parallel to the cracks within the α-grains, 12% Mn HT alloy tested in 3.5% NaCl solution 48

CDT
Centre de
Développement
Technologique
École Polytechnique
de Montréal

SUMMARY

The fatigue crack propagation behaviour of Mn-Ni-Al bronzes containing 12 and 14% Mn in air and in 3.5% NaCl aqueous solution was studied for three material conditions: as-cast (AC), normalized and slowly cooled (NSC) and normalized and subsequently annealed for 2 hr at 690°C followed by water quenching (HT material). Accelerated crack propagation was shown to occur in the NaCl solution for the higher growth rates. At the lower rates, the fatigue crack propagation was slower in the salt solution than in air as a result of corrosion-product induced crack closure effects. The HT alloys had the highest resistance to fatigue crack propagation as a result of their microstructure, which contained relatively large amounts of β-phase. The corrosion-fatigue mechanism consisted of cracking in α-grains met by the propagating crack being facilitated. In the case of AC and NSC material, this occurred as a result of fine and narrow slots proceeding ahead of the macroscopic crack front along α -β interfaces. In the case of HT material, this occurred as a result of the crack in the β-phase being able to cross α-β interfaces more easily and with less deviation. For the same material condition, there was generally little difference in the resistance ot fatigue crack propagation for the two alloys (12 and 14% Mn), whether in air or in the 3.5% NaCl solution.

Threshold values were determined or estimated. The HT condition generally gave the highest threshold values, followed by the NSC condition and the AC condition. The β-grain size was the microstructural parameter which appeared to have the most important influence on the threshold, with a large β-grain size resulting in a high threshold value. This can be explained in terms of the tendency for an increase in grain size during crystallographic cracking to reduce the effective value of stress intensity factor by roughness-induced crack closure effects, by crack deviation and crack branching effects and by the

CDT
Centre de
Développement
Technologique
École Polytechnique
de Montréal

requirement to maintain a continuous crack front across the thickness. The threshold values in the AC and NSC materials decreased on increasing the R-ratio, as a result of the decreased crack closure component. The threshold values in the HT material did not decrease significantly on increasing the R-ratio, which result was interpreted as being associated with more important crack deviation and crack branching effects. Such effects were demonstrated on metallographic sections of the crack surface profile. It was also demonstrated that such effects were responsible in the HT materials for sudden decreases in macroscopic propagation rate, when the crack arrived at some boundaries of large β-grains.

The crack closure component was subtracted by analysis of the load-crack mouth opening displacement hysteresis loops. Comparison of the crack growth results on a ΔK_{eff} basis more clearly showed the corrosion fatigue effects at high growth rates. The influence of the R-ratio was shown to influence the results on the AC and NSC materials only through its influence on the crack closure effects.

1. INTRODUCTION

Many of the important current fatigue problems are in fact corrosion-fatigue problems with an aggressive environment accelerating the fatigue crack initiation and/or propagation with respect to the behaviour in ordinary air. This reference environment itself can be considered as aggressive in comparison to fatigue in sufficiently inert environments, such as high vacuum. Because of the practical importance of corrosion fatigue, there is considerable interest in characterizing fatigue behaviour in aggressive environments and in improving our understanding of the mechanisms by which such environments shorten the fatigue life.

The present report considers the corrosion-fatigue behaviour of Mn-Ni-Al bronzes, which are ship propeller materials. For this application, good resistance to corrosion-fatigue in salt water is obviously important. A number of previous studies have been carried out on the corrosion-fatigue behaviour of ship propeller bronzes (1-5), principally on that of Ni-Al bronzes. Less is known on that of the Mn-Ni-Al bronzes, although the preliminary results obtained in the present study on the 12% Mn-Ni-Al bronze in the as-cast and normalized and slowly cooled conditions have been published (5).

The present report focusses on the influence of the environment (air compared to 3.5% NaCl aqueous solution), the R - or load-ratio (R = 0.1 and R = 0.5), the cycling frequency (f = 1 Hz and f = 20 Hz), the material condition (as-cast material and two heat-treated conditions) on the fatigue crack propagation behaviour of two Mn-Ni-Al bronzes, differing essentially in their Mn content (12% Mn compared to 14% Mn).

2. EXPERIMENTAL PROCEDURE

Plates 295 mm x 148 mm x 25 mm were cast in sand moulds at the Physical Metallurgy Research Laboratories, CANMET, employing a central riser. Two compact tension specimens of thickness B = 22.3 mm and width W = 101 mm could be machined from each plate. Material in the as-cast condition will be referred to as AC material. Some of the plates were normalized at 900°C for 2 hours followed by slow-cooling (10°C/hr) to 230°C, which will be referred to as the NSC condition Some of the plates were given a further heat-treatment, developed to improve the impact toughness of this alloy (6), of a 2 hour anneal at 690°C followed by water quenching. Material having received this heat-treatment will be referred to as HT material. These heat treatments were performed at CANMET.

The tests were performed on either an MTS or an Instron servohydraulic machine, employing a sinusoidal wave form, a cycling frequency of either 1 or 20 Hz, and an R - or load-ratio ($R = K_{min}/K_{max}$) of either 0.1 or 0.5. A desk-top computer was employed for test control and data acquisition. The crack lengths were calculated from the sample compliance and were verified with optical crack length measurements using a travelling microscope. For some tests in the 3.5% NaCl solution, the crack length could not be properly followed optically. The crack length at the end of the portion of the test in the salt solution, as calculated from the compliance, was compared to that measured on the fracture surface. Except for one specimen, for which a crack length difference of the order of 1 mm was obtained between the optical and compliance measurements, the difference was generally less than 0.5 mm and more typically of the order of 0.2 - 0.3 mm. Good agreement was obtained in the crack rates based on both optical and compliance measurements.

Typical compositions of plates employed are given in Table 1.

TABLE 1: Typical plate compositions (wt %)

	Mn	Ni	Al	Fe
12% Mn Alloy	12.0	2.1	7.8	3.1
14% Mn Alloy	14.3	2.1	8.0	3.5

The tests in the 3.5% NaCl solution were performed under freely corroding conditions by circulating this solution at a rate of 0.5 liter/min from a 3.6 liter reservoir into a plexiglass corrosion-fatigue cell, attached to the sample using electronic grade silicone glue (i.e, glue not releasing acetic acid during setting) The salt solution in the reservoir was changed every 48 hours.

3. RESULTS

3.1 Microstructures

The microstructures of Mn-Ni-Al bronze alloys have previously been investigated by Couture and Sahoo (6). These are multiphase alloys consisting primarily of a f.c.c. α-phase and a b.c.c. β-phase. Iron-rich precipitates are also present. In the present study, the AC material consisted of α-grains approximately 50 and 30 μm in diameter respectively for the 12 and 14% Mn alloys, each surrounded by a thin layer of β-phase. Some of the α-grains were elongated in Widmanstätten patterns, the observation of which allowed a rough estimate of the size

of the matrix β-grains as 0.5 mm in the 12% Mn AC alloy. The β-grain boundaries (Figure 1) could be more easily observed in the 14% Mn AC alloy, where the β-grain size was approximately 0.3 mm.

The NSC microstructure was quite similar in aspect (Figure 2) to the AC microstructure. The average diameter of the α-grains was approximately 0.1 mm and 0.08 mm in the 12% and 14% Mn alloys respectively. From the Widmanstätten patterns, the size of the β-grains was estimated as 3-4 mm in the 12% Mn and 2 mm in the 14% Mn alloy.

As shown in Figure 3, the alloys in the HT condition differed from the other two conditions by the larger amount of β-phase present (≈ 55% for the 12% Mn alloy and ≈ 65% for the 14% Mn alloy). The microstructure could now be clearly seen to correspond largely to a β-matrix encapsulating islands of α-phase. The average β-grain size was of the order of 7 mm and 3 mm respectively in the 12 and 14% Mn alloys. The respective average α-grain sizes were of the order of 0.1 and 0.08 mm.

3.2 Crack growth as a function of ΔK

It should first be noted that all individual crack growth curves showing the data points can be found in Appendix 1. The present section only presents the line curves taken as representative of the results.

The log da/dN vs log ΔK curves for the 12% Mn as-cast (AC) material are shown in Figure 4. This figure includes results in air at f = 20 Hz and R = 0.1 and 0.5 and in the NaCl solution at R = 0.1 and 0.5 and f = 1 and 20 Hz. At R = 0.1, the crack growth rates at low ΔK values are slower in the 3.5% NaCl solution than in air and the threshold or ΔK_{th} values, are higher in the salt solution. At high

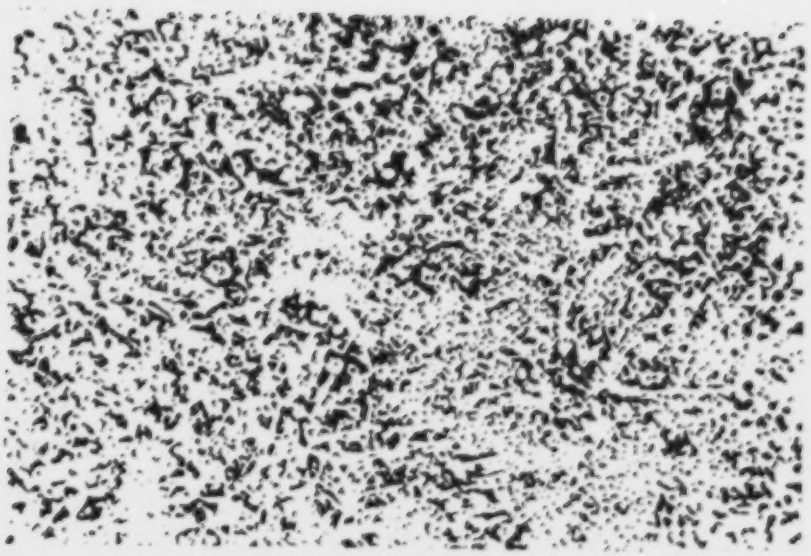

FIGURE 1: Microstructure of the 14% Mn AC alloy. The size of the β-grains can be seen by the band of white α-grains at their boundaries . Mag 100 X.

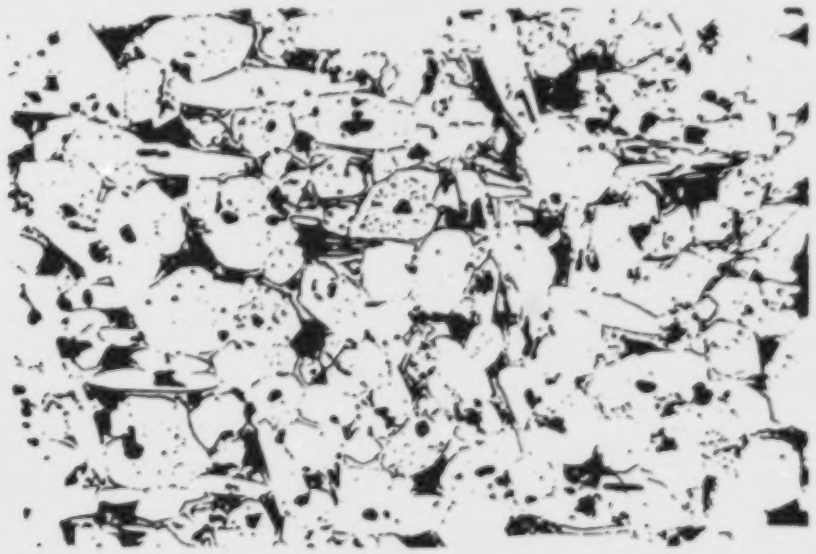

FIGURE 2: Microstructure of the 12% Mn NSC alloy. The black particles correspond to the iron-rich precipitates. 100 X.

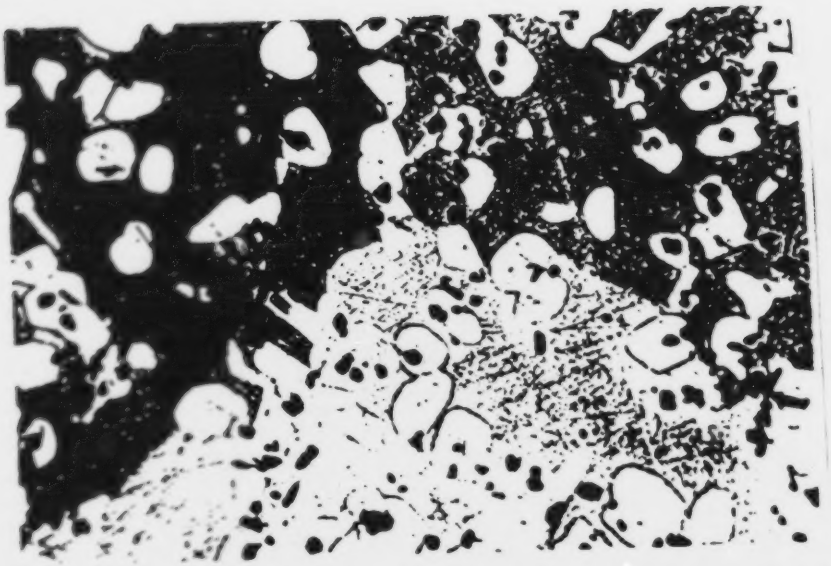

FIGURE 3: Microstructure of the 14% Mn HT alloy. The amount of β-phase is sufficiently important that the boundaries between β-grains can be distinguished using polarized illumination. 100 X.

growth rates, however, the relative positions of the curves obtained in air and in 3.5% NaCl solution generally change, suggesting the occurrence of corrosion-fatigue crack propagation effects at these higher rates. The only exception is the R = 0.1, f = 20 Hz curve in salt solution, which only rejoins the curve obtained in air. The occurrence of corrosion-fatigue at high ΔK values in the salt solution is also indicated by the increased crack growth rates above $\sim 3 \times 10^{-5}$ mm/cycle obtained at 1 Hz compared to at 20 Hz.

The tendencies obtained at R = 0.5 in this 12% Mn AC material are similar. Compared to those obtained in air, the crack growth rates in the salt solution are slower for the low growth rates and higher for the high growth rates. For the high growth rates obtained at 1 Hz in the NaCl solution, the R = 0.5 curve rejoins the R = 0.1 curve. For these high rates, crack closure effects should be least important.

Figure 5 presents the results obtained on the 14% Mn AC material. The same tendencies are observed for this higher Mn alloy as for the 12% Mn alloy. Slower crack growth is obtained in the salt solution at low growth rates in comparison to air and corrosion-fatigue effects are indicated at high growth rates. For R = 0.1, the crack growth curves at 1 and 20 Hz in 3.5% NaCl solution can be compared. The ΔK_{th} value at 1 Hz is somewhat higher than at 20 Hz, and, above $da/dn \sim 5 \times 10^{-5}$ mm/cycle, the crack growth rates become higher at 1 Hz, where they agree well with those obtained, for the same test conditions, in the 12% Mn AC alloy.

Comparing Figures 4 and 5 in detail, there is generally little difference between the crack growth rates in the two AC alloys. The crack growth rates in air were somewhat lower for the 14% Mn alloy, but the curves tended to come together at the high growth rates. For

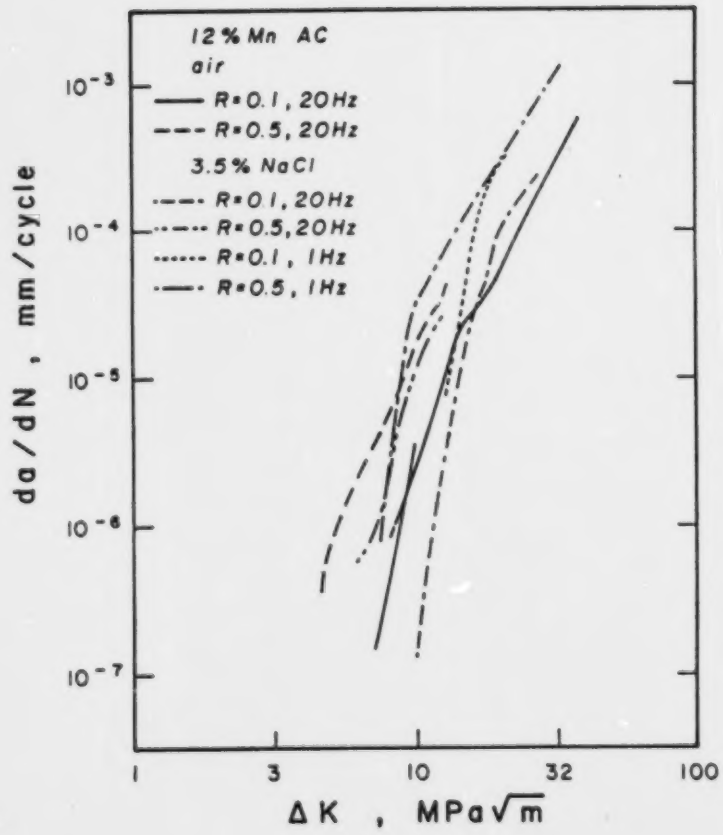

FIGURE 4: Crack growth results obtained for the 12% Mn AC alloy

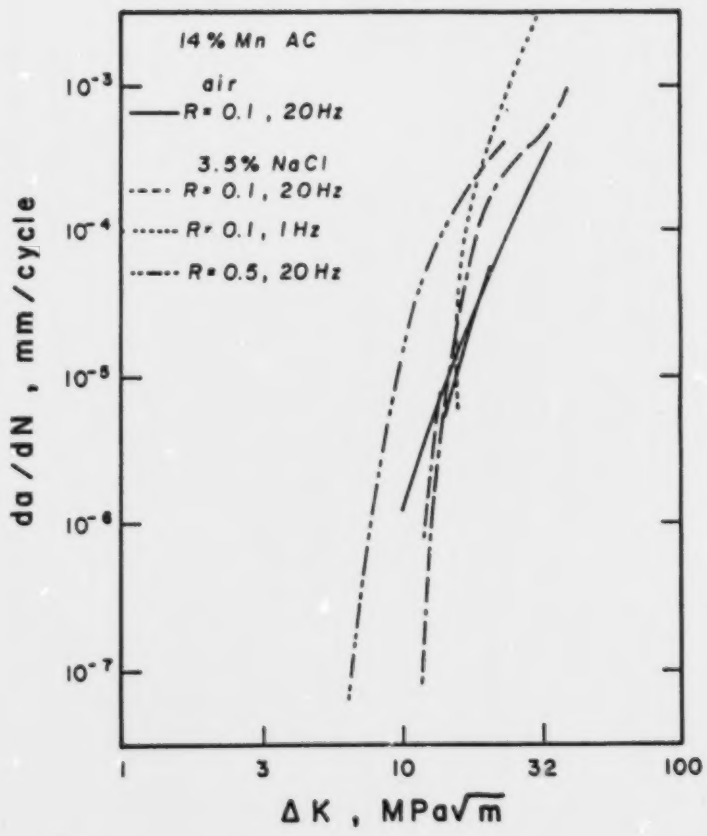

FIGURE 5: Crack growth results obtained for the 14% Mn AC alloy.

CDT
Centre de Développement Technologique
École Polytechnique de Montréal

the tests in 3.5% NaCl solution, the growth rates in the near-threshold region are similar while the high growth rates tend to be somewhat faster at the same ΔK value for the 14% Mn alloy.

The crack growth results for the normalized and slowly-cooled (NSC) alloys are presented in Figures 6 and 7. The results in the salt solution for the 12% Mn alloy (Figure 6) tested at R = 0.1 and f = 20 Hz show a considerably higher ΔK_{th} value than in air, while above $\sim 10^{-4}$ mm/cycle the curves cross over and somewhat faster crack growth is obtained in the 3.5% NaCl solution. The pair of duplicate tests in each environment show rather good agreement. At R = 0.5, the growth rates in the salt solution tend to be faster at f = 1 Hz than at f = 20 Hz for da/dN values above 10^{-4} mm/cycle.

The results on the 14% Mn NSC alloy (Figure 7) show again for R = 0.1 and f = 20 Hz a higher threshold value in the NaCl solution than in air with the crack growth rates becoming faster in this solution than in air above da/dN $\sim 5 \times 10^{-5}$ mm/cycle.

The results obtained on the two NSC alloys for similar testing conditions are generally very similar both in air (R = 0.1, f = 20 Hz) and in the 3.5% NaCl solution (R = 0.1, f = 20 Hz and R = 0.5, f = 1 Hz). The main difference obtained was somewhat faster crack growth in air for the 12% Mn allcy at intermediate growth rates (10^{-6} mm/cycle < da/dN < 10^{-4} mm/cycle). The high growth rates in the salt solution appeared to be very slightly higher in the 14% Mn alloy than in the 12% Mn alloy, although this difference is too small to be considered as significant. The influence of the difference in Mn content appeared to be less important than in the case of the AC materials.

Comparing the results for the AC and NSC conditions (Figure 8), the general trend is that, for the NSC materials, the ΔK_{th} value is

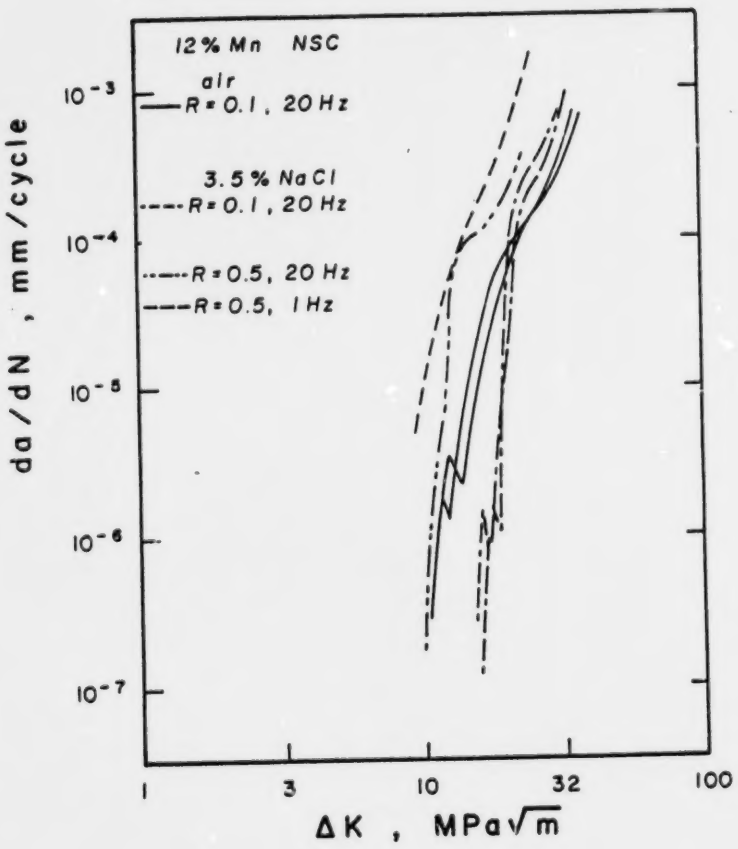

FIGURE 6: Crack growth results obtained for the 12% Mn NSC alloy.

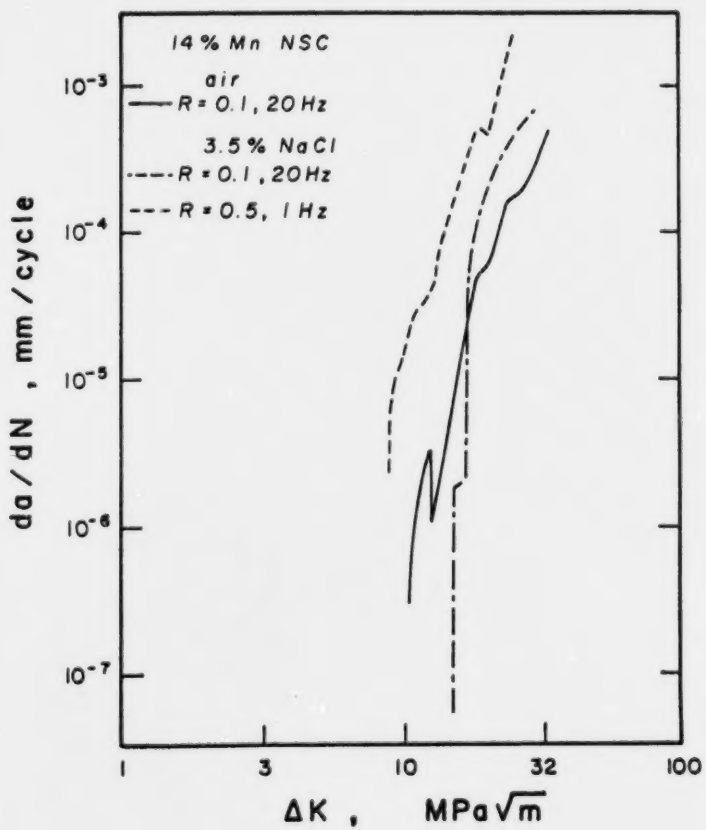

FIGURE 7: Crack growth results obtained for the 14% Mn NSC alloy.

CDT
Centre de Développement Technologique
École Polytechnique de Montréal

higher and the crack growth slower at the lower rates than for the AC materials, whether at R = 0.1 or at R = 0.5. In air (R =0.1, 20 Hz) above da/dN ≈ 5 x 10^{-4} mm/cycle, essentially the same crack growth rates are obtained for these two material conditions. The same agreement at high growth rates can also be seen for the tests in the 3.5% NaCl solution in comparing the f = 20 Hz and R = 0.1 results on the 12 or 14% Mn NSC material with the 14% AC material. For these conditions, the test on the 12% Mn AC material did not indicate an accelerated propagation rate in comparison to the test in air. The tests at R = 0.5 and 1 Hz in NaCl solution also suggested that the NSC material may be more susceptible to corrosion-fatigue crack propagation effects.

Three tests were carried out in air at f = 20 Hz and R = 0.1 on 12% Mn bronze in the HT condition, and the results are reported in Figure 9. In the first test indicated 1, the very crystallographic cracking caused the macroscopic crack plane obtained to deviate more and more from the desired crack plane, putting some doubt on the validity of the measurements obtained at higher rates (da/dN > 2 x 10^{-5} mm/cycle). The second test, indicated 2, was performed on a sample, for which a portion of a test had been carried out at R = 0.5. The crack growth curves obtained in the threshold region and at intermediate crack growth rates showed good agreement with the previous test. The good agreement in the threshold region, where the material should be most sensitive to effects of the previous loading history, indicates that the differences in the other regions of the curve were not an effect of previous loading history. A third test, indicated 3 in Figure 9, was carried out and generally showed good agreement with the results of the first test up to 3 x 10^{-5} mm/cycle.

The result from the portion of the test carried out in air at f = 20 Hz and R = 0.5 is also indicated in Figure 9. The crack growth rates at R = 0.5, in the 10^{-6} to 10^{-5} mm/cycle range correspond to lower ΔK values, however, the lowest measurement obtained rejoins that obtained at R = 0.1, which is an unusual result.

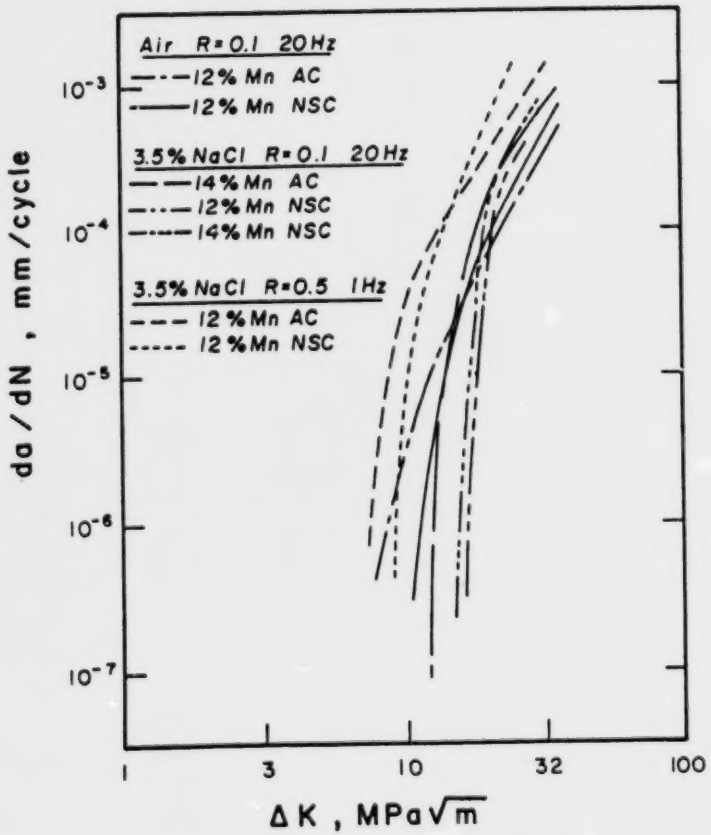

FIGURE 8: Comparison of some crack growth curves for the NSC and AC alloys.

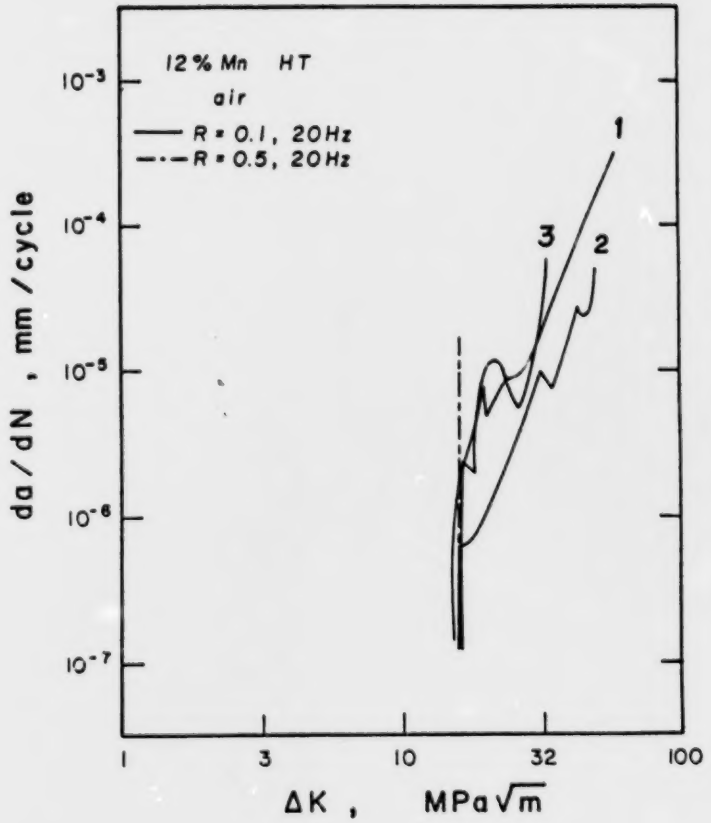

FIGURE 9: Crack growth results obtained in air for the 12% Mn HT alloy.

For da/dN values near the range of 10^{-6} mm/cycle to 10^{-5} mm/cycle, the crack growth curves obtained at R = 0.1 and f = 20 Hz showed oscillations in da/dN as ΔK increased, with the increasing value of da/dN at times suddenly decreasing by 30-60% and then slowly reincreasing.

All of these effects point out the difficulty in obtaining highly reproducible results for very crystallographic cracking in this material with a large fracture facet size, which can be taken as an effective grain size. For such a facet size, the present sample thickness which is almost twice that employed in many studies, can be considered as still insufficient to minimize the influence of the individual grain orientations. As well, the very crystallographic cracking and large facet size caused the average crack plane to deviate from the desired crack plane as the test progressed, making it difficult with the increasing ΔK procedure employed to obtain results at high growth rates.

The crack growth curves obtained in the 3.5% NaCl solution for the 12% Mn bronze in the HT condition are compared in Figure 10 to the last set of results (curve 3) obtained in air at R = 0.1 and f = 20 Hz. The tests performed in the salt solution were at R = 0.1, f = 20 Hz and at R = 0.5, f = 1 Hz. Of these two tests, that at R = 0.5, f = 1Hz gave crack growth at somewhat lower values of ΔK at the lower growth rates (3×10^{-6} to 10^{-5} mm/cycle). The two curves coincided for intermediate rates (10^{-5} to 10^{-4} mm/cycle) and the curve at R = 0.5, f = 1 Hz again gave crack growth at somewhat lower values of ΔK for da/dN values $> 10^{-4}$ mm/cycle. In comparison to the tests carried out in air, higher threshold values and slower crack growth in the near-threshold region were obtained in the NaCl solution. The curves for R = 0.1, 20 Hz cross over towards da/dN $\simeq 10^{-5}$ mm/cycle, above which crack growth is faster in the salt solution.

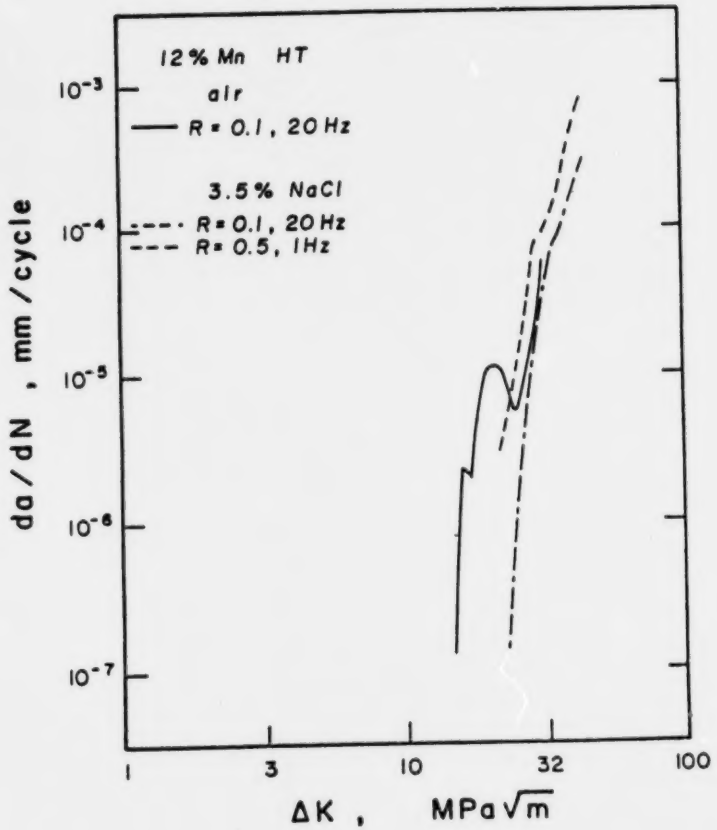

FIGURE 10: Crack growth results obtained in 3.5% NaCl solution for 12% Mn HT alloy.

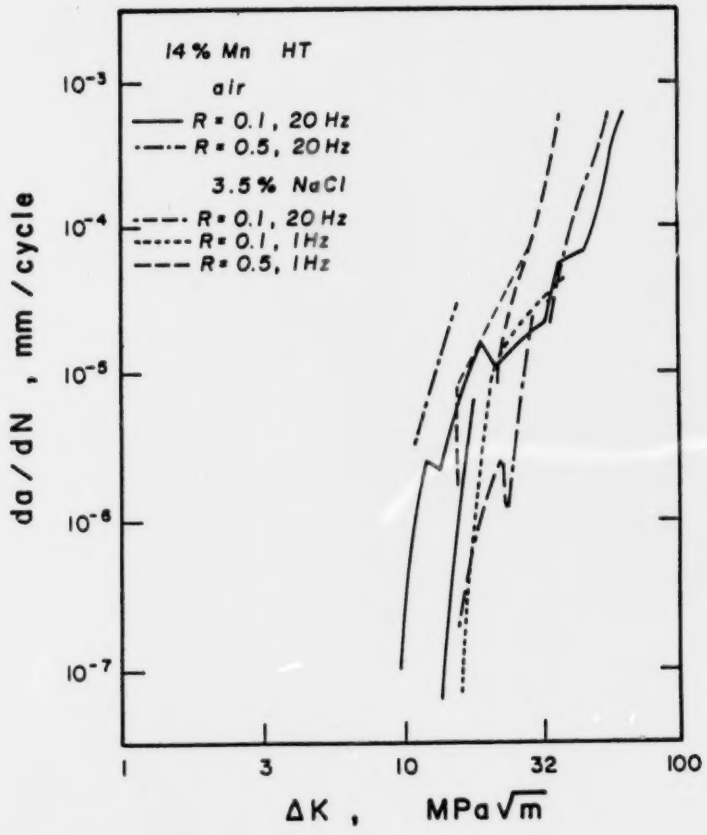

FIGURE 11: Crack growth results obtained for the 14% Mn HT alloy.

CDT
Centre de Développement Technologique
École Polytechnique de Montréal

The results of the tests carried out on the 14% Mn bronze in the HT condition are presented in Figure 11. These tests consisted of a test in air at f = 20Hz and R = 0.1, and three tests in the NaCl solution, one at f = 20 Hz and R = 0.1 and two at f = 1 Hz, one at R = 0.1 and one at R = 0.5. Comparison of the two tests carried out at f = 20 Hz and R = 0.1 shows a higher threshold value and slower crack growth in the near-threshold region in the NaCl solution than in air. The two curves approximately coincided in the range 2×10^{-5} mm/cycle < da/dN < 5×10^{-5} mm/cycle and faster crack growth rate was obtained in the salt solution for higher growth rates. The crack growth curve obtained in the 3.5% NaCl solution at f = 1 Hz and R = 0.1 showed considerable dispersion in da/dN values but agreed with that at f = 20 Hz and R = 0.1 in the salt solution in the near-threshold region. Crack growth at lower ΔK values was obtained at f = 1 Hz in the 10^{-6} mm/cycle < da /dN < 10^{-5} mm/cycle range and at higher da/dN values the two curves coincided. For these higher values, however, a fatigue crack started propagating from one of the two holes for the loading pins in the specimen and its presence no doubt influenced the apparent compliance in the hysteresis loops measured, making the da/dN data obtained of doubtful quality for da/dN > 2×10^{-5} mm/cycle for the test at f = 1 Hz and R = 0.1.

The test on the 14% Mn HT material performed in the NaCl solution at f = 1 Hz and R = 0.5 was entirely performed using a ΔK decreasing procedure. The test was commenced at da/dN ≃ 8×10^{-6} mm/cycle and the threshold approached. The lowest da/dN value thus obtained was 1.7×10^{-6} mm/cycle. Instead of performing a ΔK increasing procedure, the ΔK value was then increased to obtain the highest da/dN values on the curve and the remaining portion of the curve obtained employing a ΔK decreasing procedure but without taking the type of precautions employed in threshold measurements. With such a procedure, crack retardation effects can be expected, associated with a crack

propagating in a plastic strain zone produced at a higher ΔK value. The relatively high growth rates obtained for the ΔK values employed in the high da/dN ($> 10^{-4}$ mm/cycle) portion of the curve, where crack closure effects should be least important, indicate that this was not a problem for these high growth rates. The two portions of the curve in the da/dN $\simeq 10^{-5}$ mm/cycle range, however, do not rejoin each other. The indication is that crack retardation effects were important for the intermediate crack growth rates (10^{-5} mm/cycle $<$ da/dN $<$ 8×10^{-4} mm/cycle). An estimate of the true behaviour in the intermediate range can be obtained by interpolating between the portion of the curve below da/dN $\simeq 8 \times 10^{-5}$ mm/cycle and the portion above da/dN $\simeq 8 \times 10^{-4}$ mm/cycle, as indicated by the dashed curve in Figure 11. Comparison of this curve with that obtained in the NaCl solution at f = 20 Hz and R = 0.1 shows that the curve at f = 1 Hz and R = 0.5 presents faster crack growth rates for all values of ΔK.

Figure 12 compares some of the crack growth curves for the HT materials with some of the curves for the NSC materials. The HT material curves, especially for the higher da/dN crack growth rates, lie to the right of the curves for the NSC material, i.e. to the side of lower growth rates and higher ΔK values. In the near-threshold region the curves for the two material conditions are more similar.

3.3 Crack growth as a function of ΔK_{eff}

At low crack growth rates, crack closure effects have a particularly strong influence on log da/dN vs log ΔK curves, since for a portion of the crack intensity range, the crack in the vicinity of the crack tip is closed and no cycling of this region is produced during this portion of ΔK. This ineffective portion of ΔK can be subtracted from ΔK by measuring K_{op}, the K value at which the crack tip becomes opened. The partially closed crack has a compliance indicative of a crack length shorter than the true length. As the amount of length

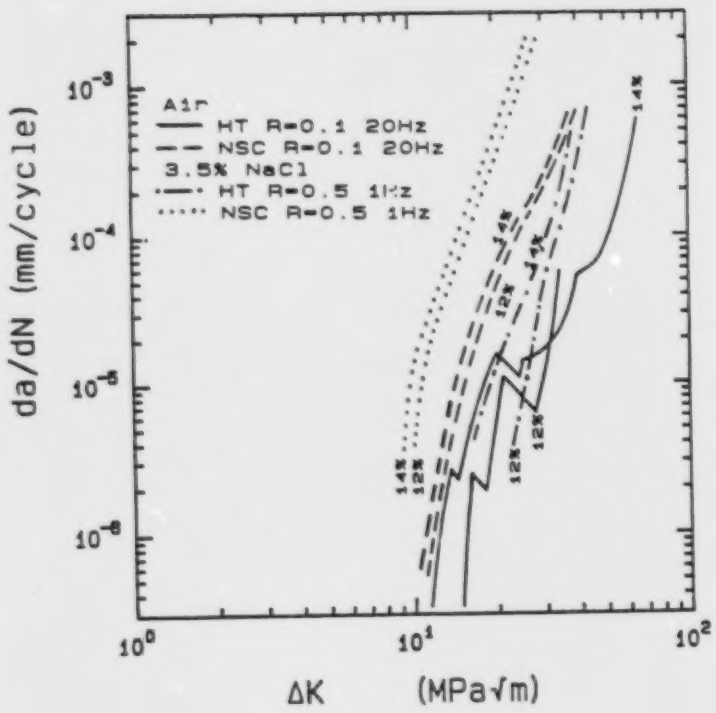

FIGURE 12: Comparison of some crack growth curves for the HT and NSC alloys.

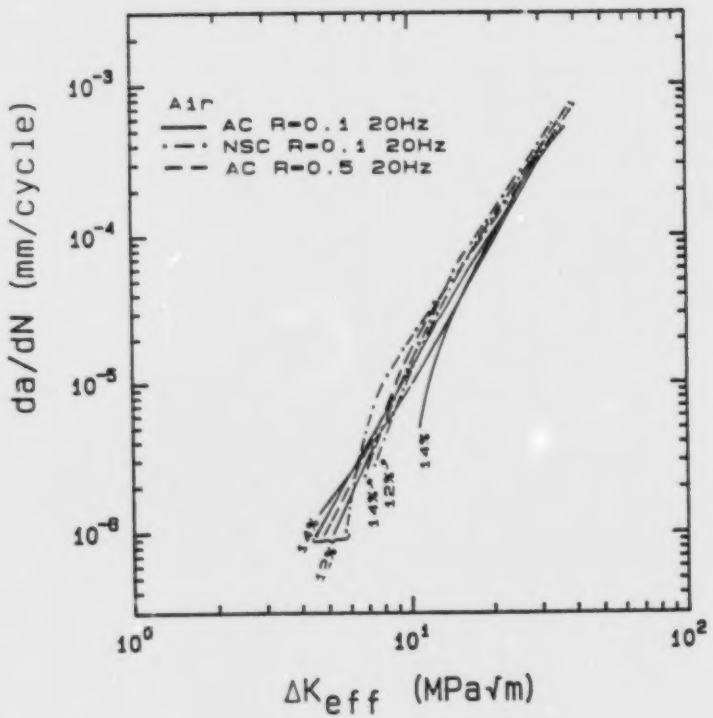

FIGURE 13: Crack growth rates as a function of ΔK_{eff} for the tests performed in air on the AC and NSC materials.

over which the crack is closed decreases, the compliance increases accordingly. Once the crack tip is opened, a constant compliance and linear elastic behaviour are obtained until the plastification of the crack tip regions influence. The value of K_{op}, can thus be obtained by determining the value of K at which the compliance becomes constant and linear elastic behaviour is first obtained. The effective value of stress intensity range, $\Delta K_{eff} = K_{max} - K_{op}$, thus obtained is somewhat of a misnomer since this measurement only corrects for the crack closure component. Other factors such as crack deviation and crack branching can cause the stress intensity acting at the crack tip to be less than the ΔK calculated conventionally based on the load range and the crack length.

Most methods of determining K_{op} presuppose the portion of ΔK in which linear elastic behaviour will be obtained. Recent work has been carried out at Ecole Polytechnique (7) in order to develop a more objective method of determining K_{op}. Different methods were tried on the present data. The method finally judged to be the most logical consisted of supposing that the crack mouth opening displacement (CMOD) vs load (P) curve consisted of three portions, with the linear elastic portion being the intermediate portion. The CMOD vs P data was treated in order to fit this data (using a least squares technique and a Taylor series about the extremities of the linear portion) to this three stage CMOD vs P curve which is treated as a cubic curve at low P, the linear intermediate portion and a parabolic portion at high P. Since a Taylor's series development is employed, only the part of the curved regions close to the linear portion is fitted. A condition imposed is that linear and curved portions must join together at a point of common slope, and this point is taken as an extremity of the linear portion. The lower of these two extremities corresponds to P_{op}, and to the corresponding CMOD value. For the higher curved region, corresponding to plastification, the apparent compliance actually increased, and this effect has also been found by other workers (8) on other materials.

All data previously reported in the progress reports have been retreated using this improved treatment, both to redetermine the ΔK values based on the compliance of the linear elastic portion and to redetermine ΔK_{eff} values.

The results of these log da/dN vs ΔK eff results are summarized in Figures 13 to 17. The individual crack growth curves plotted on both a ΔK and a ΔK_{eff} basis can be found in appendix I.

Figure 13 reports the log da/dN vs log ΔK curves obtained for tests in air on the two bronzes in the AC and NSC conditions. Only data for da/dN values greater than $\approx 3 \times 10^{-6}$ mm/cycle are reported, since at lower rates considerable precision is lost in the measurements of the value of ΔK_{eff} associated with the crack closure component becoming increasingly important as da/dN decreased. Figure 13 indicates that a single curve essentially describes, on a ΔK_{eff} basis, all the data obtained in air on the AC and NSC materials. In particular, this shows that the influence of the R-ratio on the log da/dN vs log ΔK curves for the AC and NSC materials tested in air is simply that of a decreased non-effective portion of ΔK associated with the increase in R-ratio and in K_{min}.

Figures 14 and 15 report the log da/dN vs log ΔK_{eff} curves obtained for tests in the 3.5% NaCl solution for the two bronzes in the AC and NSC conditions, respectively, and compares these results with the single curve obtained in air. For the AC condition (Figure 14), all the results obtained in the NaCl solution show accelerated crack propagation on a ΔK_{eff} basis compared to the tests in air for da/dN > 10^{-5} mm/cycle. Except for the test on the 14% Mn bronze tested at f = 20 Hz and R = 0.1 for which ΔK_{eff} appears underestimated, the remaining

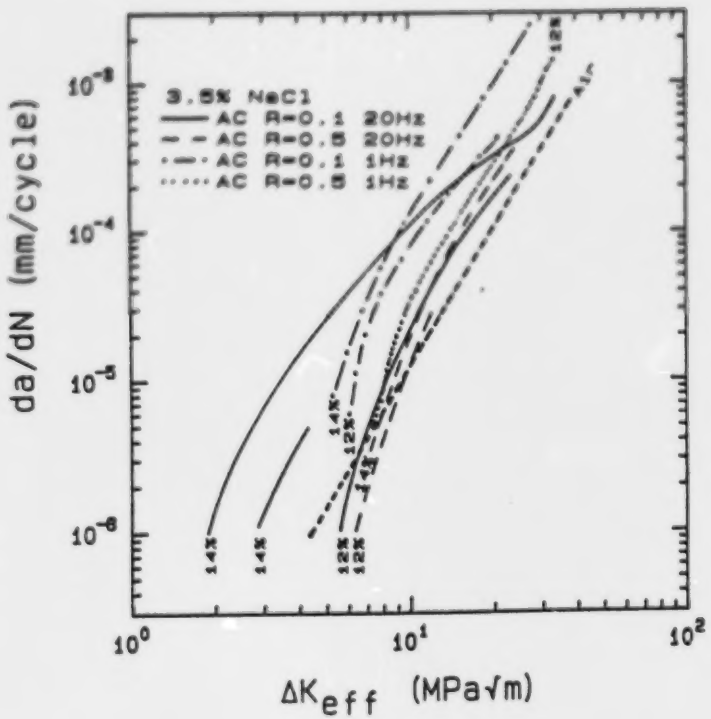

FIGURE 14: Crack growth rates as a function of ΔK_{eff} for the AC materials tested in the 3.5% NaCl solution.

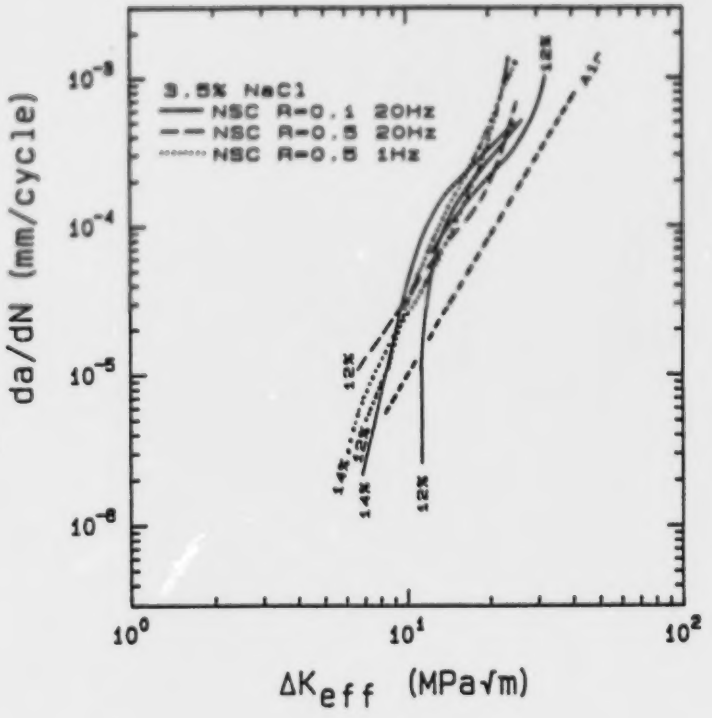

FIGURE 15: Crack growth rates as a function of ΔK_{eff} for the NSC materials tested in the 3.5% NaCl solution.

curves suggest faster crack growth rates in the NaCl soluiton for da/dN > 10^{-5} mm/cycle for tests at 1 Hz compared to tests at 20 Hz. For the tests in the NaCl solution on the NSC material (Figure 15), quite similar behaviour is obtained. For this condition, all curves in the NaCl solution show accelerated crack growth at high da/dN values (generally da/dN > 10^{-5} mm/cycle) compared to the log da/dN vs log ΔK_{eff} curve in air. The crack growth rates obtained in the NaCl solution at 1 Hz is higher than at 20 Hz for da/dN values greater than ≈ 10^{-4} mm/cycle. In both Figures 14 and 15, the crack growth data at R = 0.1 and 0.5 in the NaCl solution also agree well on a ΔK_{eff} basis.

Figures 16 and 17 report the log da/dN vs log ΔK_{eff} basis obtained for the HT materials tested in air and in 3.5% NaCl solution respectively. Considerable scatter was obtained in this data, especially for the tests carried out in air, for which a large facet size was generally obtained. Accelerated crack growth in the HT material tested in the NaCl solution compared to that tested in air is also seen for da/dN values > 3 x 10^{-5} mm/cycle. The improved resistance to fatigue crack growth in both the air and salt water environments for these HT material compared to the AC and NSC material can also be seen on a ΔK_{eff} basis.

3.4 Threshold values

A considerable portion of the fatigue testing time in the present study was spent obtaining crack growth results at very low propagation rates (da/dN < 10^{-5} mm/cycle). In some of the tests, crack growth rates were obtained for da/dN values of the order of 10^{-7} mm/cycle. Obtaining similar ultra-low crack growth rates in all tests would have required even more testing time. The threshold values are therefore reported (Tables 2 and 3) both as the value ΔK_{th}, obtained by extrapolating the log da/dN vs log ΔK curve to a rate of 10^{-7} mm/cycle

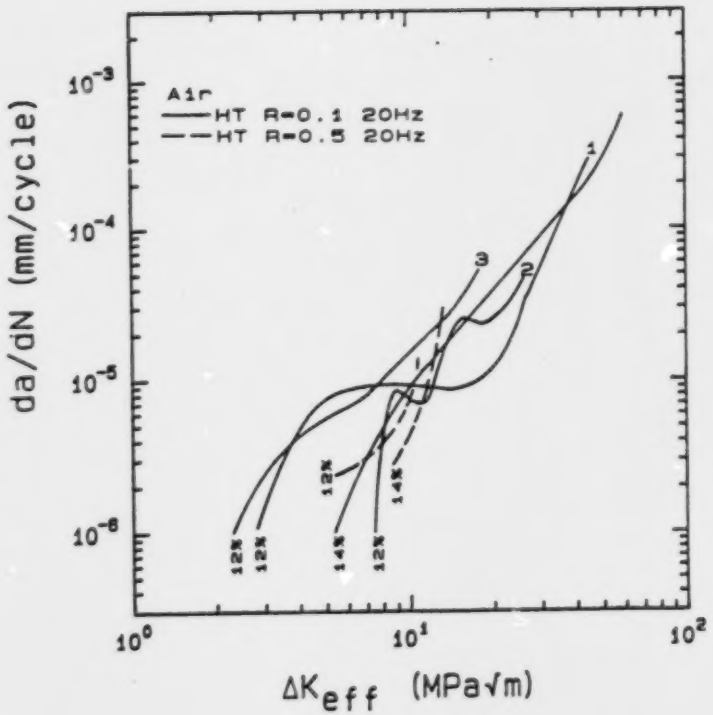

FIGURE 16: Crack growth rates as a function of ΔK_{eff} for the tests performed in air on the HT materials.

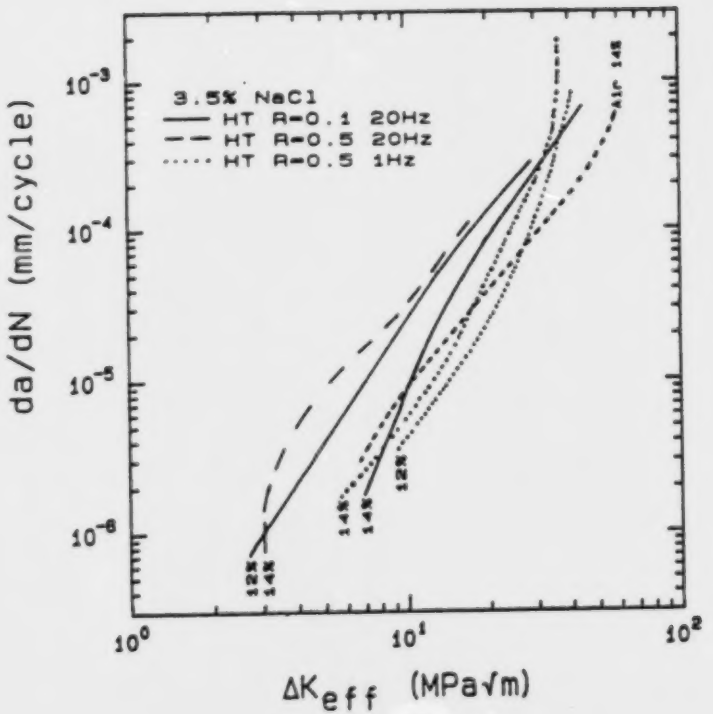

FIGURE 17: Crack growth rates as a function of ΔK_{eff} for the tests performed in 3.5% NaCl solution on the HT materials.

and as the lowest value of ΔK actually attained, ΔKth^*, accompanied by the corresponding measurement of da/dN, indicated in Tables 2 and 3 as da/dN*.

It should also be noted that in treating the hysteresis loops in order to obtain objective measurements of effective stress intensity factor, ΔK_{eff}, the portion of the load-crack mouth opening displacement hysteresis loops which shows linear elastic behaviour for an open crack was redetermined by best-fit techniques without any prior supposition as to which portion of the curve should be linear. The slope of the linear portion determined in this manner should be that from which the compliance and thus the crack length can best be measured, or at least measured most objectively. All previous results, which were in part based on presupposing which portion of the loop was linear, were then reanalyzed employing this more objective method of determining the compliance and crack length.

The threshold measurements thus obtained are presented in Table 2 for the 12% Mn alloy and in Table 3 for the 14% Mn alloy. These results differ somewhat from those previously reported in the progress reports on this study. Since crack closure effects are particularly important in the threshold region, it is in this region that the use of compliance measurements to determine crack lengths and ΔK values is most susceptible to imprecision.

3.5 Fractographic Observations

The fracture surfaces especially those produced in the NaCl solution were covered with corrosion product. For the surface produced in air, this corrosion product could be removed easily by ultrasonic cleaning in a liquid soap-water solution. The portion of fracture

TABLE 2

Threshold Values

12% Mn Alloy

Plate No	Condition	Environment	f Hz	R	$\Delta K_{th}'$ MPa(m)$^{1/2}$	ΔK_{th}^* MPa(m)$^{1/2}$	da/dN mm/cycle
2419-1-B1	as-cast	lab air	20	0.1	7.2	7.6	1.6×10^{-7}
2419-1-B2	as-cast	lab air	20	0.1	NE	8.7 [1]	8.4×10^{-7}
2419-1-B2	as-cast	lab air	20	0.1	NE	7.6* [2]	8.4×10^{-7}
2419-1-B1	as-cast	3.5% NaCl	20	0.1	9.9	10.0	1.3×10^{-7}
2419-1-A1	as-cast	3.5% NaCl	1	0.1	NE	13.4	6.8×10^{-6}
2419-1-A2	as-cast	lab air	20	0.5	4.6	4.6	3.8×10^{-7}
2419-1-A2	as-cast	3.5% NaCl	20	0.5	4.9	6.6	5.6×10^{-7}
2419-1-A2	as-cast	3.5% NaCl	1	0.5	6.4	7.4	8.8×10^{-7}
2628-1-A2	NSC	lab air	20	0.1	9.2* [1]	9.1	7.5×10^{-7}
2628-1-A2	NSC	lab air	20	0.1	8.7 [2]	8.9	2.7×10^{-7}
2628-1-A1	NSC	lab air	20	0.1	NE	10.4	6.0×10^{-7}
2628-1-B1	NSC	lab air	20	0.1	11.5	11.5	5.0×10^{-7}
2628-1-A2	NSC	3.5% NaCl	20	0.1	15.1	15.3	2.6×10^{-7}
2628-1-B2	NSC	3.5% NaCl	20	0.1	16.6	16.6	1.6×10^{-7}
2628-2-A2	NSC	3.5% NaCl	20	0.5	10.4	10.4	1.7×10^{-7}
2628-2-A1	NSC	3.5% NaCl	1	0.5	NE	9.9	5.1×10^{-7}
2628-3-A1	HT	lab air	20	0.1	15.7	15.7	2.0×10^{-7}
2628-3-A3	HT	lab air	20	0.1	16.8	16.8	1.3×10^{-7}
2628-3-A2	HT	lab air	20	0.1	15.1	15.2	1.5×10^{-7}
2628-2-B	HT	3.5% NaCl	20	0.1	20.9	20.9	1.5×10^{-7}

* based on optical measurements
1,2 indicates two threshold measurements for same basic test.
NE not extrapolated

TABLE 3

Threshold Values

14% Mn Alloy

Plate No	Condition	Environment	f Hz	R	$\Delta K_{th}'$ MPa(m)$^{1/2}$	ΔK_{th}^* MPa(m)$^{1/2}$	da/DN* mm/cycle
2541-3-A1	as-cast	lab air	20	0.1	8.1*	8.9	4.2×10^{-6}
2541-3-A1	as-cast	lab air	20	0.1	NE	10.2	1.2×10^{-6}
2535-1-A1	as-cast	3.5% NaCl	20	0.1	12.6	12.6	$1.0 \quad 10^{-7}$
2535-1-A2	as-cast	3.5% NaCl	20	0.1	11.7	12.7	8.5×10^{-7}
2535-1-A2	as-cast	3.5% NaCl	1	0.1	NE	15.2	2.5×10^{-6}
2541-3-A2	as-cast	3.5% NaCl	20	0.5	6.8	6.7	8.0×10^{-8}
2624-2-A1	NSC	lab air	20	0.1	11.0	11.0	3.0×10^{-7}
2624-2-A2	NSC	3.5% NaCl	20	0.1	15.8	15.7	8.0×10^{-8}
2624-2-A3	NSC	3.5% NaCl	1	0.5	NE	9.1	2.6×10^{-6}
2624-2-B	HT	lab air	20	0.1	10.2	10.2	1.2×10^{-7}
2624-1-B	HT	3.5% NaCl	20	0.1	15.8	16.6	2.3×10^{-7}
2624-3-A2	HT	3.5% NaCl	1	0.1	16.1	16.0	7.0×10^{-8}
2624-3-A1	HT	3.5% NaCl	1	0.5	16.2	16.2	1.7×10^{-6}

* based on optical measurements
1,2 indicates two threshold measurements for same basic test.

surface produced in the NaCl solution at higher growth rates in all materials could also be cleaned thus, although the cleaning times required were longer. After cleaning, these fracture surfaces produced in the salt solution presented a sharp transition (Figure 18) from covered by blackish oxide film to well-cleaned surface, this transition corresponding very well to the change towards da/dN values of 3×10^{-5} to 10^{-4} mm/cycle in the slope of the log da/dN curve from the very steep slope extending from the near-threshold region to the more gradual slope at high propagation rates. This transition in colour of cleaned fracture surface also corresponded in NSC material to a sharp decrease (Figure 19) in the number of finer macroscopic ridge lines (i.e., those barely visible with the naked eye). In the scanning electron microscope, these macroscopic lines were seen to correspond to groups of finer ridge lines and the transition appeared to correspond to the cracking becoming less crystallographic, although the fractographic details could not be observed on the portion that remained covered with corrosion product. The thickness of corrosion product on the fracture surfaces produced in NaCl solution appeared particularly important for the HT alloys.

For the AC materials, especially those tested in the NaCl solution, fine facets (≈ 0.7 mm for the 12% Mn alloy and ≈ 0.3 mm for the 14% Mn alloy) could be observed macroscopically on portions of the fracture surfaces.

For NSC material some large facets (≈ 5 mm in diameter for the 12% Mn alloy and ≈ 4 mm in diameter for the 14% Mn alloy) could be seen on portions of the fracture surfaces. These facets tended to disappear for the highest growth rates and also tended to be less observable on the fracture surfaces produced in air. For HT material tested in air, the fracture surfaces consisted entirely of large facets (≈ 8 mm for the 12% Mn alloy and ≈ 4 mm for the 14% Mn alloy) with a

FIGURE 18: Sharp transition (arrows) in appearance of fracture surface produced on the 12% NSC alloy tested in 3.5% NcCl solution after ultrasonic cleaning. Magnification 1.3 X.

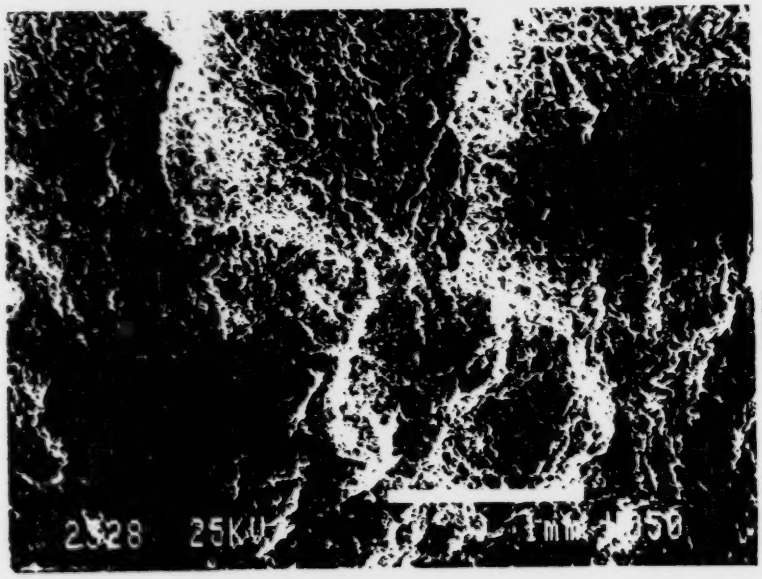

FIGURE 19: The sharp transition on Fig. 18 also corresponds to a sharp decrease in the number of finer macroscopic river or ridge lines on the fracture surface.

tendency for the macroscopic river lines on these facets to be arranged somewhat in fan-shapes within individual grains (Figure 20). For the HT material tested in air, the portion of the fracture surface produced at low growth rates in air was not covered with darkish corrosion product. For the HT material tested in the salt solution, the large facets were less clearly present at the low growth rates, where the fracture surface remained covered with dark corrosion product after cleaning. As well for the 12% Mn alloy, the large facets produced in the NaCl solution were approximately half the size of those produced in air. Changing the environment to air then resulted in the immediate approximate doubling of the facet size. For the 14% Mn alloy, the facet size in both environments was more comparable.

In general the size of the large facets observed on the fracture surfaces agreed with the size of the β-grains determined metallographically although the former tended to be somewhat larger, possibly because the fracture facets more often crossed the thicker portions of the β-grains than did the metallographic sections.

The microfractographic details were studied by scanning electron microscopy, although for the test in the salt solution, only the portions of the fracture surface which had been successfully cleaned could be thus studied. For the AC and NSC materials, cracking occurred primarily in the α-phase. For tests in air or in salt solution where the crack growth was not accelerated with respect to air, the main feature was that the crack propagation direction could be followed in a straightforward fashion from α-grain to α-grain (Figure 21). At lower rates, the cracking in the α-phase was very crystallographic. At sufficiently high rates crystallographic striations could be observed. At higher rates ($da/dN > 10^{-4}$ mm/cycle), the striations in the α-phase became non-crystallographic.

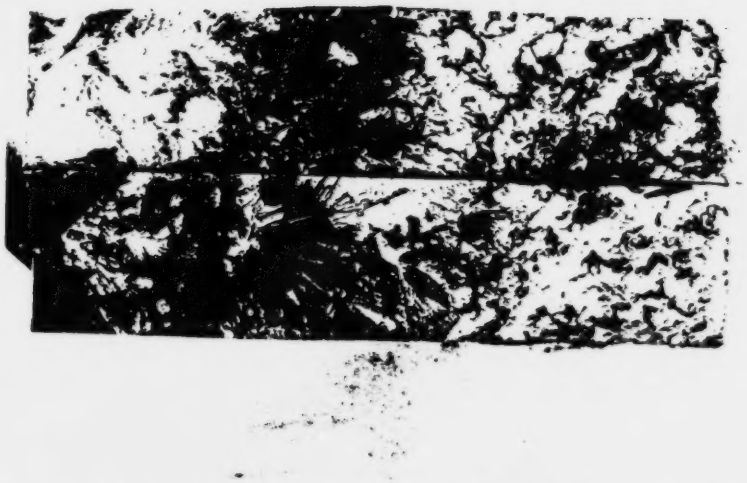

FIGURE 20: Macroscopic aspect of the fracture surface produced on the 14% Mn HT alloy tested in air (lower specimen) and in 3.5% NaCl solution (upper specimen). Magnification 1.1 X.

FIGURE 21: Ductile striations at high growth rates in the 12% Mn AC alloy tested in air. Crack propagation proceeds in a straightforward fashion from α-grain to α-grain. The macroscopic propagation direction is indicated by a large arrow.

FIGURE 22: Ductile striations at high growth rates in the 12% Mn NSC alloy tested in 3.5% NaCl solution Fine slots at the α-β boundaries proceed ahead of the macroscopic crack front. As a result the local propagation directions (small arrows) in the α-grains can even propagate back towards the macroscopic crack front.

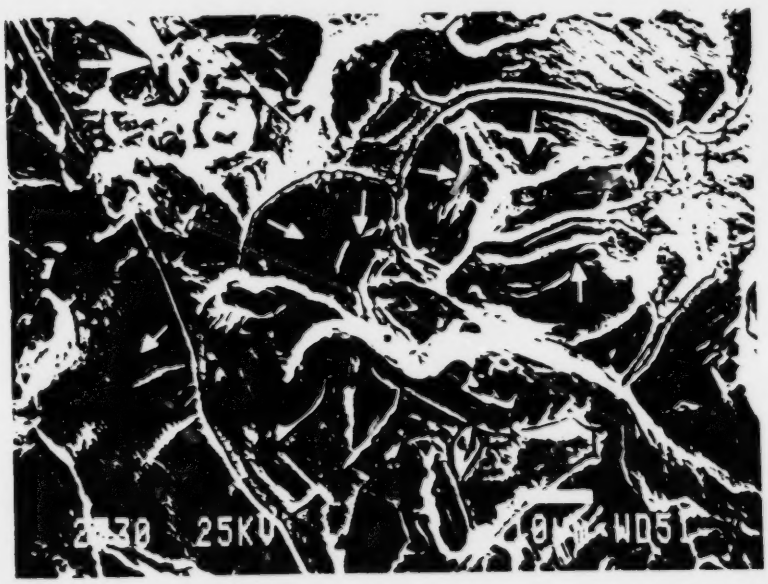

FIGURE 23: Effect of slotting at α-β interfaces on initiating cracking in α-grains ahead of the marcroscopic crack front in 12% Mn NSC alloy tested in 3.5% NaCl.

For the fracture surfaces in the salt solution corresponding to accelerated crack growth with respect to air, the microfractographic features within the α-grains were identical to that observed at similar growth rates in the tests in air. The important difference was that slotting had occurred at the α - β interfaces and proceeded ahead of the macroscopic crack front. This resulted in fatigue cracking in the α-grain initiating from the slots extending ahead of the macroscopic crack front (Figures 22 and 23) and propagating laterally into the α-grains or even propagating back towards the macroscopic crack front (Figure 22). Some α-grains which had been surrounded by slots at the α - β interfaces fractured like low-cycle fatigue specimens with fatigue cracking initiating at several sites along the perimeter of the α-grain. These crack initiation sites can be recognized since the regions of crack growth resulting from neighbouring initiation sites are separated by ridge lines and since the interstriation spacing increases as the crack propagates.

For the HT material tested in air, the larger facets observed macrofractographically were seen by scanning electron microscopy to consist of a large number of smaller facets, many of which resembled the aspect of the larger facets and many of which appeared to be parallel. For the 14% Mn alloy with its higher volume of β-phase, the α-grains could be distinguished quite easily since they generally occurred as islands within the very crystallographic β microfacets which covered the majority of the fracture surface. In the enclosed α-facets, the fracture surface was generally much more irregular but still crystallographic. Cracking in the β-phase could be seen to tend to partially or occasionally to completely bypass the α-grains (Figure 24). In the latter case, these α-grains could fracture from several initiation sites along the α - β interface. In somes cases, the α-grains fractured largely by decohesion at the α - β interfaces.

At the higher growth rates, fatigue striations could be observed on the β-facets. The interstriation spacing was irregular and influenced by the local microstructure (Figure 25). Often the interstriation spacing increased towards the center of a microfacet only to redecrease on approaching an α-grain. Striations could at times also be found on α-facets, with the interstriation spacing typically 3 - 10 times finer than that in the surrounding β-facets. The general indication was that the presence of the α-grains hindered the fatigue crack propagation in the 14% Mn HT alloy.

For 12% Mn HT alloy, the higher amount of α-phase present resulted in almost 50% of the fracture surface passing through this phase. From observing the facets in the large β-grains for which the α and β microfacets could be distiguished more easily, it was found that the β microfacets were smoother than the α-facets which contained pronounced river lines. Crack propagation appeared to lead in the β microfacets where it often occurred almost parallel to the macropropagation direction for the large β-grain. From the α - β interfaces, crack propagation then spread laterally into the α-grains also in a crystallographic manner but with more pronounced river lines (Figure 26).

Although difficulty was experienced in cleaning the fracture surfaces of the HT material tested in NaCl solution, the portions of fracture surface produced at the higher growth rates, where the results of the mechanical tests indicated corrosion-fatigue effects, were cleaned sufficiently to permit reasonable observations of the basic microfractographic features. The presence of the α-phase appeared to have little influence on hindering fatigue crack growth in this environment. Cracking in the β-phase generally did not tend to bypass that in the α-grains. The fracture surface in the α-grains was generally smooth, covered with ductile striations, and often coincided well with the

FIGURE 24: Bypassed α-grain by the faster crack propagation in the β-phase for the 14% Mn HT alloy tested in air. Local propagation directions in an α-grain are indicated by small arrows.

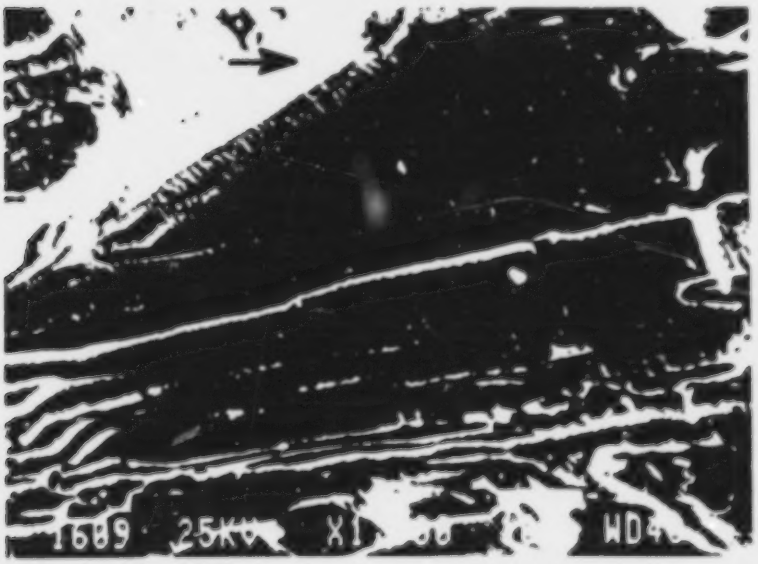

FIGURE 25: Variable interstriation spacings observed at high growth rates on a β-microfacet for the 14% Mn HT alloy tested in air. The interstriation spacing is largest towards the center of the microfacet.

plane of the fracture surface in the surrounding β-facets (Figure 27). The interstriation spacing in the α-grains was generally similar to that in the neighbouring β-facets. In the 14% Mn alloy, the fracture surface produced in the NaCl solution appeared to more frequently cross α-grains than those produced in air. Some α-grains were surrounded by slots similar to that observed for the AC and NSC material tested in salt solution, and their presence occasionally caused fatigue initiation in an α-grain to proceed from more than one site along the perimeter of this grain. More often the fatigue cracking in the α-grains proceeded parallel to the local macroscopic crack propagation direction. Striations in the β-phase were also more marked for testing in NaCl solution than for testing in air, although the striations in the NaCl solution appeared to have a more ductile aspect and a more regular interstriation spacing than those produced in air.

The general aspects of the microfractographic features for the higher propagation rates in the HT alloy tested in 3.5% NaCl solution indicate that cracking occurred more uniformly and in a more straightforward fashion than for cracking in air.

3.6 Metallographic observations of crack paths

Metallographic sections were also prepared intersecting the fracture surface near mid-thickness parallel to the crack propagation direction. The fracture surface was first covered with several coats of lacquer which was then hardened at ≈ 150°C (hardening at ≈ 60° was employed for later observations) to prevent rounding of the edges during metallographic polishing. In this manner it was confirmed metallographically that the cracking in the AC and NSC materials occurred essentially in the α-phase. In the 14% Mn HT material cracking occurred primarily in the β-phase, while, in the 12% Mn HT material, cracking occurred almost equally in both phases. Crack branchings were

FIGURE 26: Microfractographic aspect of the 12% Mn HT alloy tested in air. Many of the β-microfacets present only fine river lines. Some of the α-grains, which occur as round islands within the β-matrix, can be easily recognized. The lateral propagation in these α-grains indicates that the microscopic crack front leads in the flat β-microfacets.

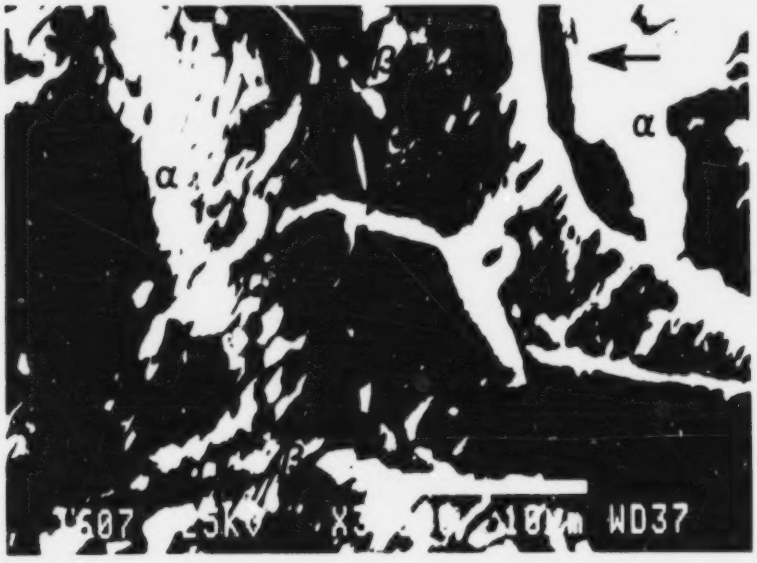

FIGURE 27: Flattened ductile striations observed for the higher growth rates in the 14% Mn HT alloy tested in 3.5% NaCl solution. The microstructure has little influence on the local crack growth.

frequently observed in the 14% Mn HT alloy but were rare in the 12% Mn HT alloy. The slots at the α-β interfaces responsible for the corrosion fatigue effect in the AC and NSC materials were also observed thus (Figure 28). These were always narrow slots generally extending less than 20 μm from the fracture surface.

For the bronzes in the HT condition, the larger amount of β-phase present resulted in more important amounts of cracking in the b.c.c. β-phase. For the 12% Mn HT material, the amount of cracking occurring in both phases is quite similar (Figure 29). For the 14% Mn HT material, the majority of the cracking occurs in the β-phase (Figure 30). For these two materials quite frequent secondary cracks could be found at least at the lower crack growth rates. Observations pertaining to the influence of the α-grains on the crack propagation could then be obtained from viewing the secondary cracks as well as the profile of the fracture surface on the longitudinal metallographic sections.

In the 12% Mn HT alloy tested in air, the crack path was rather devious (Figure 29), especially in the α-grains (Figure 31). The crack path also appeared to change frequently by small steps between parallel planes in the β-phase, possibly as a result of the crack front frequently meeting α-grains in which propagation was difficult. Aspects of the cracks within the α-grains at times suggested that the cracking in some α-grains came from opposite (Figure 31) sides of the grain perimeter and met somewhere in the middle, with one crack stopping on encountering the other. The very tortuous crack paths in the α-grains appeared to be largely responsible for the devious crack paths within the large β grains. The crack surface profile was microscopically rough, reflecting the numerous small changes in crack plane. The crack path within the large β-grains tended to be roughly

CDT
Centre de
Développement
Technologique
École Polytechnique
de Montréal

FIGURE 28: Slots (small arrows) at α-β interfaces seen on the profile of the crack surface, 12% NSC alloy tested in the 3.5% NaCl solution, R = 0.1, f = 20Hz.

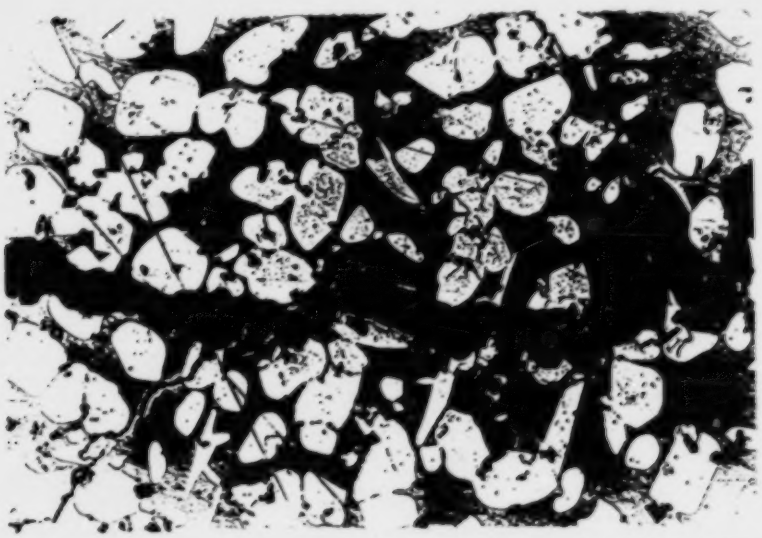

FIGURE 29: Large and fine secondary cracks observed on the 12% Mn HT alloy tested in air. The devious aspect of the crack path is seen. Some of the fine cracks stop on meeting α-grains, go along α-β interfaces and along interfaces with blackish particles. 200 X.

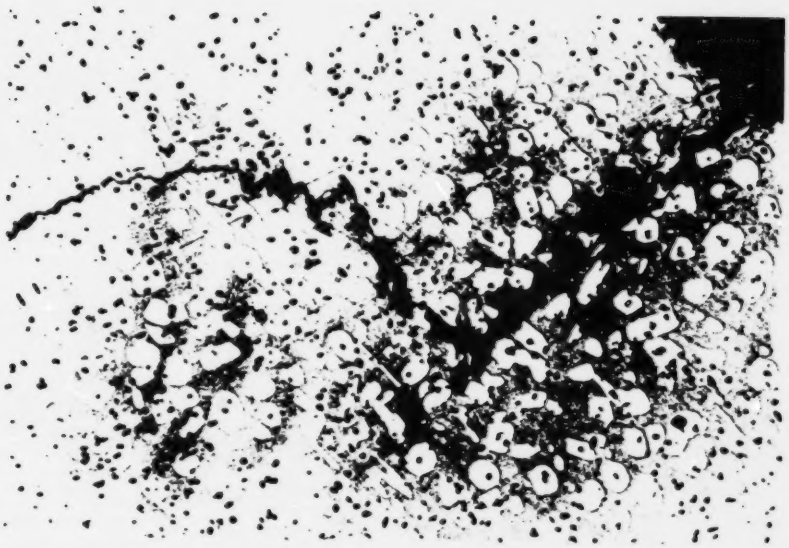

FIGURE 30: Aspects of the path of a secondary crack in 14% Mn HT bronze tested in air. Sections of the crack path in the β-phase tend to be parallel to two orientations of elongated α-grains. 50 X.

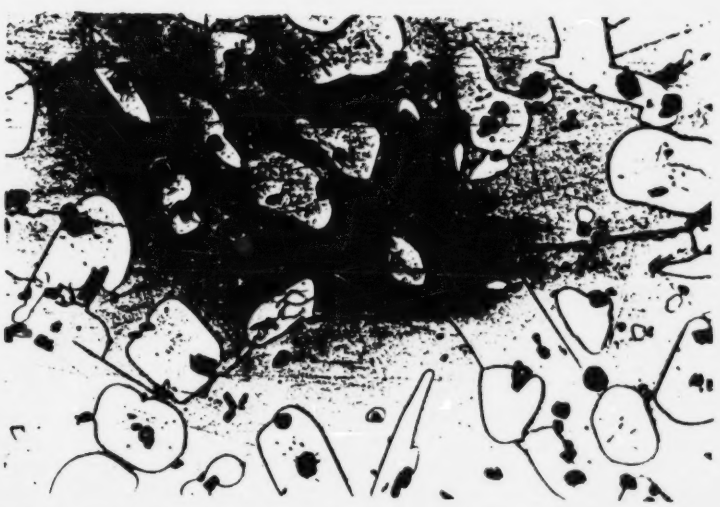

FIGURE 31: Details of the path of a secondary crack in 12% Mn HT bronze tested in air. 100 X.

parallel to certain non-identified crystallographic planes. A number of segments in the β-phase of secondary cracks were roughly parallel (Figures 30 and 33) to one or two of the orientations of elongated α-grains arranged in Widmanstätten patterns and to straight apparently crystallographic interfaces of non-elongated α-grains. Some tendency was noted for the crack path within α-grains to be near or at times apparently at α-β interfaces (Figures 29 and 31). The end of a secondary crack often corresponded to a crack in the β-phase stopping on meeting an α-β interface (Figure 32).

For the 12% Mn HT alloy tested in the NaCl solution the crack path within the larger α-grains was straighter (Figure 33) and more clearly crystallographic within the β-phase. The orientations of different secondary cracks within a β-grain were more clearly parallel to the different orientations of elongated α-grains. The crack path within the α-grains was less devious and often did not deviate or only deviated slightly from that in the β-phase. There was also less tendency for the crack path within α-grains to be situated near α-β interfaces.

In the 14% Mn HT material, the crack path obtained in air (Figures 30 and 34) was also more devious than that obtained in the NaCl solution (Figures 35 and 36). For the tests in air, the crack path almost always changed directions in entering α-grains and the crack path within the α-grains was often tortuous. The crack path within the β-phase often changed directions slightly, but was straighter than that in the 12% Mn HT bronze tested in air. For the tests in NaCl solution, the crack path in the 14% Mn HT bronze was also straighter than in the 12% Mn alloy. In general, the crack in the 14% Mn alloy tested in salt solution had less tendency to deviate in crossing α-grains. Some secondary cracks could still be seen to terminate at α-β interfaces on meeting α-grains (Figure 36).

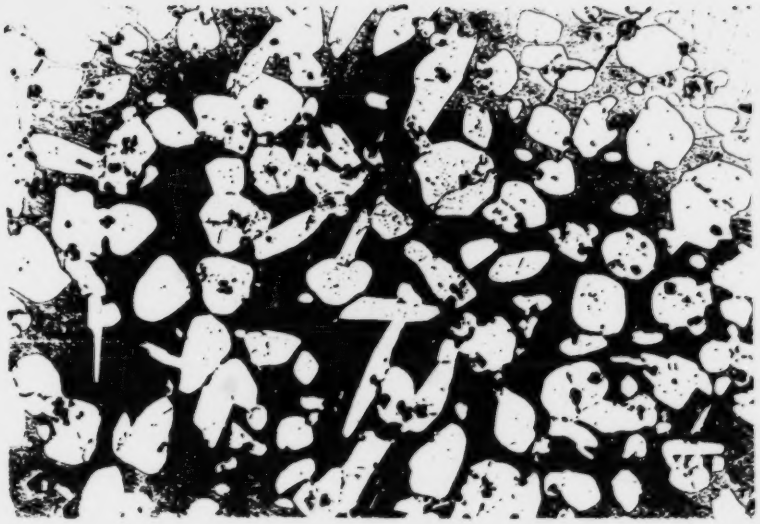

FIGURE 32: End of a secondary crack in 12% Mn HT bronze tested in air. Each of two crack branches terminates on meeting an α-grain. The crack in the β-phase is generally parallel to one of the orientations of elongated α-grains. 100 X.

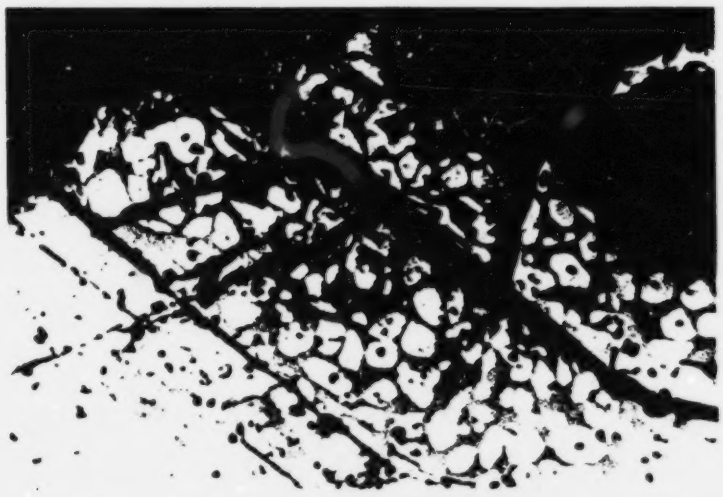

FIGURE 33: Relatively straight secondary cracks parallel to three orientations of elongated α-grains in 12% Mn HT alloy tested in 3.5% NaCl solution (f = 20 Hz, R = 0.1). 50 X.

CDT
Centre de
Développement
Technologique
École Polytechnique
de Montréal

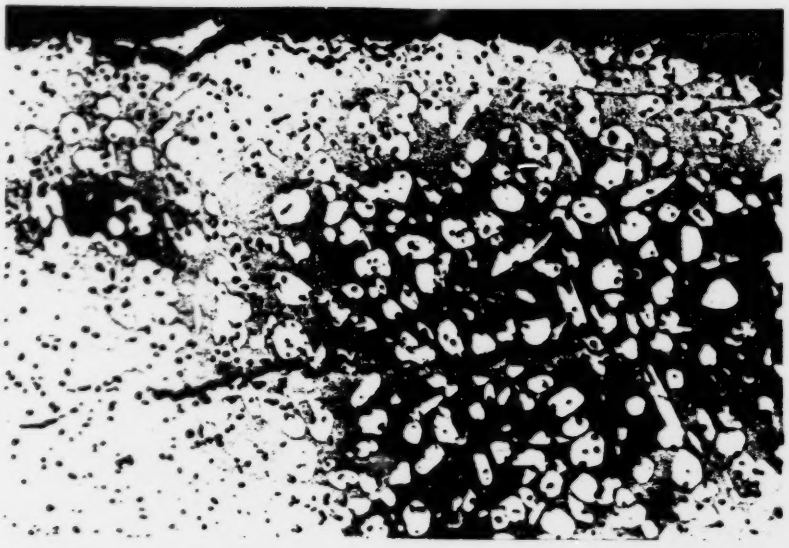

FIGURE 34: Secondary crack in 14% Mn HT alloy tested in air parallel to the profile of the crack surface. The secondary crack terminates soon after crossing a β-grain boundary. 50 X.

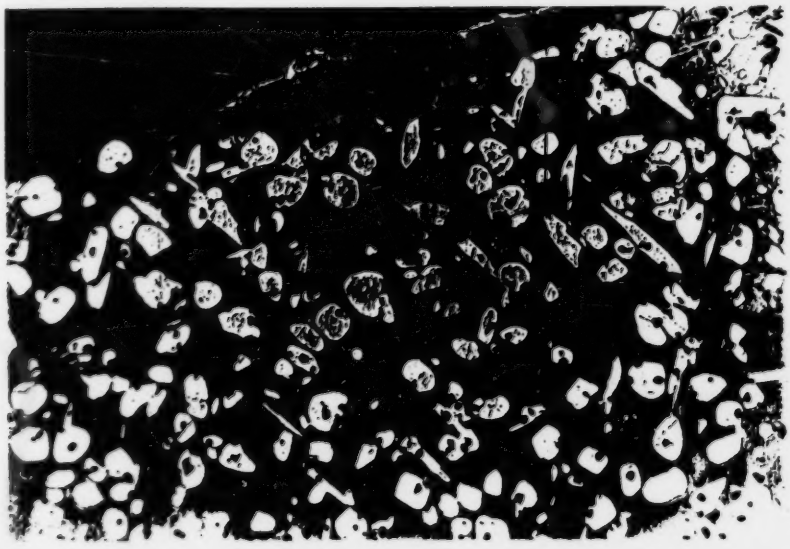

FIGURE 35: Relatively straight secondary crack parallel to crack surface profile and to one orientation of elongated α-grains in 14% Mn HT alloy tested in 3.5% NaCl solution (f = 20 Hz, R = 0.1). The crack deviates only slightly on meeting α-grains except when it meets several closely spaced α-grains. 64 X.

The influence of the blackish iron-rich particles on the fatigue crack path was also studied on these metallographic sections. The exact crack path within such particles could not be easily observed because both appeared black. In general, however the presence of these black particles did not have any influence on the straighter cracks obtained in the tests in the NaCl solution. If such a particle was in the path of a straight crack, the crack appeared to cut across the particle. Cracks generally did not appear to deviate to meet such particles, although very occasionally a crack appeared to deviate very slightly to go along the interface of a black particle situated very near the crack path. The more devious crack paths obtained in air showed a somewhat greater tendency to deviate slightly to go along an interface of a black particle situated very close to the crack path. Even for the tests in air, these black particles appeared to have only a very minor influence on the crack paths.

3.7 Influence of β-grain boundaries in HT material as observed by metallography

Secondary cracks were seen to have considerable difficulty in propagating across β-grain boundaries (Figures 34 and 36) in the HT materials. For the lower crack growth rates, the crack profile observed on the metallographic sections generally showed pronounced deviations (Figure 37) in macroscopic crack path on crossing grain boundaries. This was often accompanied (Figure 37) by the formation of relatively large secondary cracks (i.e. crack branching) near this β-grain boundary. Moreover, good agreement was found between the sites at which the crack crossed β-grain boundaries with an important deviation in the crack surface profile accompanied by important crack branching was observed at mid- thickness and the crack lengths at which sudden decreases in crack growth rates were observed in the approximate da/dN

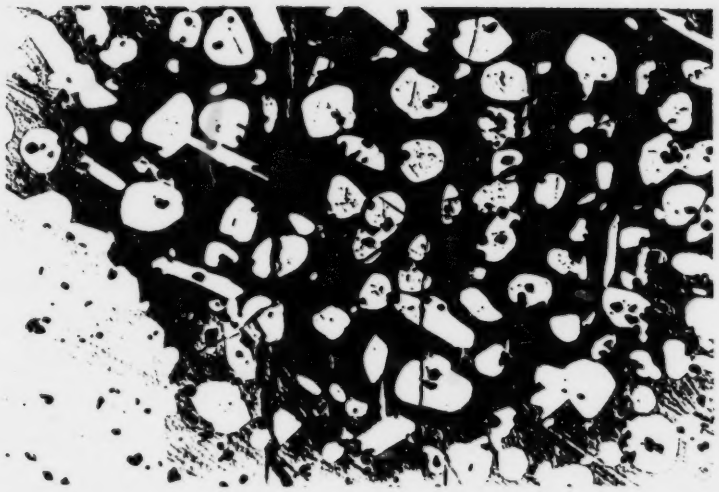

FIGURE 36: The secondary cracks observed in 14% Mn HT alloy tested in 3.5% NaCl solution (f = 20 Hz and R = 0.1) are parallel to two orientations of elongated α-grains, although few elongated grains are found for one of these orientations. One of the secondary cracks can be seen to terminate on meeting an α-grain at a β-grain boundary. 100 X.

FIGURE 37: Deviation of the crack surface profile and crack branching at a β-grain boundary in the 12% Mn HT alloy tested in 3.5% NaCl solution.

range of 10^{-6} to 10^{-5} mm/cycle. At higher ΔK values, the deviations at β-grain boundaries tended to be less severe and generally unaccompanied by important amounts of crack branching.

3.8 Secondary cracking in the near-threshold region, HT material

For cracking in the threshold region, patterns of very extensive secondary cacks were observed metallographically in the region close to the fracture surface for the HT alloys tested in NaCl solution. Examples are shown in Figures 38 and 39. Crystallographic series of cracks are present in both the α-grains and β-phases. The cracks in the α-phase are often arranged in triangular patterns with angles of close to 60° between the different crack orientations suggesting cracking on (111) planes. The (111) orientation of these cracks produced at low ΔK in the α-phase was verified by microhardness indentations produced in a few of the α-particles (Figure 40). The cracks in the α-phase were parallel to the slip traces thus produced, confirming the (111) orientation. The β-phase was considerably harder and well-resolvable slip lines were not produced by the microhardness indentations in this phase. Many of the crystallographic cracks in the β-phase were parallel to elongated Widmanstatten type α-grains.

This very important secondary cracking at low growth rates in the HT alloys tested in the 3.5% NaCl solution also appeared associated with crack deviations within α-grains (Figure 39), which permits to explain the smaller macroscopic facet size observed for tests in the 3.5% NaCl compared to tests in air.

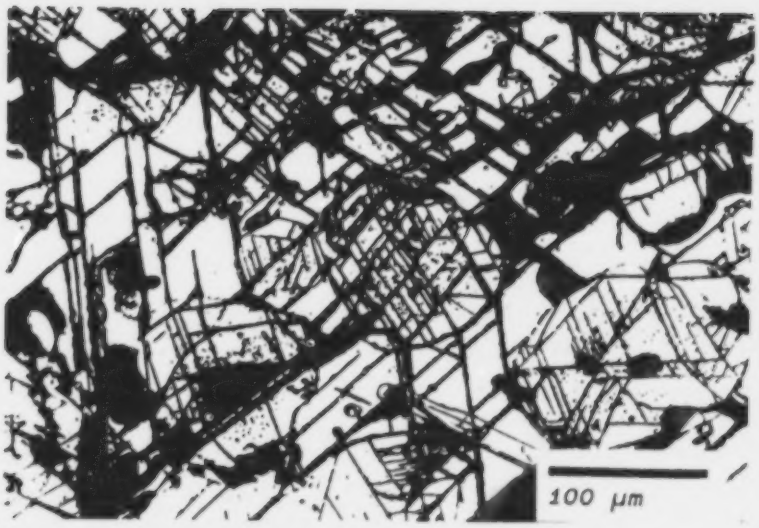

FIGURE 38: Extensive crack branching near the crack surface in the threshold region of the 12% Mn HT alloy tested in the 3.5% NaCl solution.

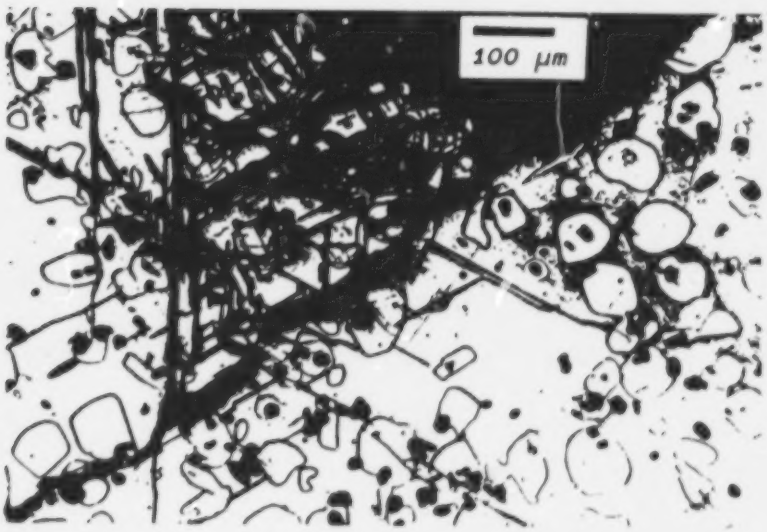

FIGURE 39: Extensive crack branching in the region of a crack surface deviation within a β-grain, 12% Mn HT alloy tested in 3.5% NaCl solution. The secondary cracks in the β-phase and the profile of the cracks surface are parallel to the orientations of elongated α grains.

FIGURE 40: Slip traces produced in an α-grain by microhardness indentations are parallel to the cracks within the α-grains, 12% Mn HT alloy tested in 3.5% NaCl solution.

4. DISCUSSION

4.1 Influence of alloy condition on crack propagation curves in air

Comparing first the influence of the AC and NSC alloy conditions on the fatigue crack growth in air, the curves obtained indicate that the NSC alloys have a higher threshold value than the AC alloys but these curves then rejoin at high growth rates. The influence of alloy condition on the threshold will be discussed in the following section (4.2). At high growth rates, the microstructure which otherwise is not radically different except for grain size no longer influences, as is often the case in the Paris law region of the log da/dN vs log ΔK curve.

Crack propagation in the HT materials is considerably more difficult than in the AC and NSC materials. The fractographic and metallographic observations indicate that this effect is associated largely with the more important amount of crack propagation that must then occur in the β-phase of the HT materials, while in the AC and NSC materials the β ligaments between α-grains are thin compared to the size of the α-grains. As well, as indicated by the fractographic observations, the duplex microstructure of the HT alloys is such that the presence of the α-grains hinders the fatigue crack propagation in air. This latter effect was much less important (but according to the metallographic observations of secondary cracks not completely absent) for the tests in the NaCl solution, where the resistance to crack propagation in the HT alloys still remained superior to that in air for the AC and NSC alloys. This result confirms the importance of the β-phase in imparting good fatigue crack propagation resistance to the HT materials. Lastly, for the HT materials, the fatigue crack propagation

remained highly crystallographic even for the highest growth rates employed. Crack deviation effects which tend to decrease the effective ΔK value for mode I cracking should then influence the crack growth rates for the entire range studied.

The crack growth curves for the 12 and 14% Mn bronzes in the HT condition tested in air at f = 20 Hz and R = 0.1 agree well with each other for da/dN values > 10^{-5} mm/cycle although one of the three curves for the 12% Mn alloys lies to the right of the other curves. From the fractographic observations as well as from the metallographic observations on secondary cracks, the α-grains more frequently encountered by the propagating crack in the 12% Mn alloy had a more important influence on the crack morphology and favored a more tortuous crack path in both the α and β-phases. For the 14% Mn alloy, the crack in the larger β ligaments between α-grains is relatively straight which was seen to aid this crack in crossing the α-grains with less changes in propagation direction. The more tortuous crack path in the 12% Mn alloy did not appear to result in significantly slower crack growth rates compared to the 14% Mn alloy; however, only one test was performed in air in this latter alloy. The higher percentage of β-phase in the 14% Mn HT alloy may have compensated for the less tortuous crack path in this 14% Mn alloy, since it appears clear that the presence of this phase is responsible for an important portion of the good resistance to fatigue crack propagation of these alloys in the HT condition. These aspects underline the complicated nature of the influence of the characteristics of this duplex microstructure on the resistance to fatigue crack propagation. For the low-growth rates, as discussed in section 4.5, the β-grain size appears to become the dominant parameter influencing the near-threshold behaviour and the threshold values.

The iron-rich black particles do not significantly influence the fatigue crack propagation because their size is small with respect

to the crack segments and they are too dispersed to have a strong influence.

4.2 Fatigue Crack Propagation in the 3.5% NaCl Solution

All the tests in the 3.5% NaCl solution with the exception of the test on the 12% Mn AC alloy at f = 20 Hz and R = 0.1 indicated accelerated crack growth at high growth rates (da/dN > 10^{-4} mm/cycle) in this environment relative to the rates obtained in air. Decreasing the frequency to 1 Hz resulted in a further acceleration of these crack growth rates. These results clearly indicate the occurrence of corrosion-fatigue effects at these high growth rates in the NaCl solution.

At the low growth rates, the opposite effect was obtained. The crack growth was slower and the ΔK_{th} values higher in the NaCl solution than in air. As well, the fracture surfaces produced at the low growth rates in the NaCl solution were covered with darkish corrosion product which was not removed by the ultrasonic cleaning procedure employed. After cleaning, a sharp transition was observed on these fracture surfaces produced in NaCl solution between the portion that has not been successfully cleaned and that which had. This transition always corresponded well to the change in slope in the log da/dN vs log ΔK curve from the very steep slope extending from the near-threshold region to a less steep slope. The indication is, as confirmed by ΔK_{eff} measurements on the 12% Mn AC and NSC alloys, that the high ΔK_{th} values and the initially very steep slope of the log da/dN vs log ΔK curve obtained in the NaCl solution are the result of corrosion product wedging effects. The darkish colour of this corrosion product and its

strong adherence to the fracture surface in comparison to that produced at higher da/dN values suggest that this is a product of fretting corrosion.

4.3 The influence of the R-ratio and crack growth as a function of ΔK_{eff}

Increasing the R-ratio from R = 0.1 to R = 0.5 can be seen to decrease ΔK_{th} and to accelerate the crack growth at the lower rates but to have less of an influence on the high crack growth rates. The ΔK_{eff} measurements on AC and NSC materials indicated that the increase in R-ratio corresponded entirely to a decrease in crack closure effects, thus reducing the difference between the applied and the effective ΔK values. At high growth rates, crack closure effects are small even at R = 0.1, and the influence of the R-ratio tends to disappear even on a ΔK basis.

By subtracting the crack closure effects, the comparison of the crack growth data on a ΔK_{eff} basis allows a clearer observation of the accelerated crack growth obtained for the tests in the NaCL solution. In this solution, the corrosion product crack closure effects are important at both low and intermediate values of da/dN. As a result on a ΔK basis the accelerated corrosion-fatigue crack propagation at intermediate da/dN values is largely masked by the corrosion-product induced closure effects. This is particularly true at f = 20 Hz and R = 0.1, where the corrosion-fatigue effect is not very pronounced and the crack closure effects are important. The comparison on a ΔK_{eff} basis also indicate that the corrosion-fatigue effects are also essentially a function of ΔK and not of K_{max} or of the mean value of K, since the R-ratio is not seen to influence the crack propagation rate in the NaCl solution.

4.4 Corrosion-fatigue mechanism

As demonstrated by both the fractographic and metallographic observations, the corrosion-fatigue mechanism responsible for the accelerated crack growth rates in the NaCl solution in the AC and NSC material corresponds to fine narrow slots at the α-β interfaces proceeding ahead of the macroscopic crack front and helping to initiate ductile fatigue cracking in the neighbouring α-grains. While this mechanism was previously referred to as a dissolution mechanism (5), since it appears similar to effects observed in Ni-Al bronzes (4), the crack growth rates involved are high for such a mechanism, and this slotting more probably results from a stress sorption mechanism. In these AC and NSC alloys, crack propagation in air occurs in a straightforward fashion and the occurrence of slotting at the α-β interfaces results in more irregular cracking when corrosion-fatigue propagation occurs. An unusual feature on this corrosion-fatigue effect is that it appeared to become progressively more important as the crack growth rate increased.

For the HT materials, the situation is, in some aspects, quite different. It is cracking in air which results in less straightforward cracking, because important amounts of cracking are occurring in both phases and the crack propagation in the β-phase experiences difficulty in crossing the α - β boundaries and in fracturing the α-grains. As a result, the local microscopic crack propagation rate varies considerably. In these HT materials, as for the AC and NSC materials, corrosion-fatigue acts to facilitate crack initiation and propagation in the α-grains. As a result, the α-grains largely lose their ability to hinder fatigue crack growth in these HT materials and the local variations in microscopic cracking rate largely disappear. This effect is at least partially responsible for the significant acceleration of the macroscopic crack propagation rate observed at higher

da/dN values for the HT material in the NaCl solution. From the present study, it could not be determined whether the accelerated crack growth also resulted in part from a corrosion-fatigue mechanism affecting the β-phase of this HT material.

4.5 Threshold values

Comparing the influence of the material condition on the threshold values obtained in air at f = 20 Hz and R = 0.1, the lowest threshold values for the 12% Mn alloys are obtained for the AC material, the intermediate values for the NSC material and the highest values for the HT material. This relative order is in agreement with that of the β-grain sizes and thus shows agreement with the usual rule that a larger grain size results in a larger threshold value. That the β-grain size acts as the effective grain size, as concerns the influence of microstructure on the threshold value, is indicated by the β-grain size controlling the facet size on the fracture surfaces. The relative variation being influenced by the β-grain size is also indicated for the 14% Mn alloy, where the AC material has the lowest ΔK_{th} value in air at f = 20 Hz and R = 0.1 and the NSC and HT materials have quite similar threshold values and quite similar β-grain sizes, with both the ΔK_{th} and the grain size being somewhat larger for the HT material. The relative order of the β-grain sizes does not completely explain these threshold values and, for example, cannot explain the larger ΔK_{th} values obtained for the 14% Mn AC material compared to the 12% Mn AC material.

For the 12% Mn HT tested in air at f = 20 Hz and R = 0.1, particularly high ΔK_{th} values were obtained. This is consistent with the large crystallographic facets obtained giving a macroscopically rough fracture surface as well as important crack deviation (9) effects on crossing grain boundaries. These crack deviation effects were shown

to be responsible above ΔK_{th} for sudden decreases in da/dN as the mid-thickness portion of the crack arrived at β-grain boundaries. Moreover, the α-grains in this alloy tested in air favour a microscopically rough fracture surface because of the deviations in crack path within the α-grains and the frequent encounters between the propagating crack and such grains. The rough fracture surface obtained on both a macroscopic and a microscopic scale should give rise to strong roughness-induced crack closure effects, with the crack deviation and crack branching effects also making additional contributions favouring a large difference between the effective value of ΔK and the applied value (i.e., the value calculated by simply taking into account the crack length and the load range, ΔP).

Testing in the NaCl solution results in increased ΔK_{th} values and this is associated with corrosion-product wedging effects resulting form the testing in this environment. The important influence of the corrosion product produced during fatigue propagation in the 3.5% NaCl solution was demonstrated by noting that in the AC and NSC materials, the change in slope of the log da/dN vs log ΔK curve from the threshold region to a less steep slope at higher ΔK corresponded well with the demarcation line on the fracture surface separating the region produced at lower da/dN values which could not be effectively cleaned ultrasonically and that produced at higher da/dN values which could be properly cleaned.

The influence of increasing the R-ratio from 0.1 to 0.5 to decrease considerably the threshold value in the AC and NSC materials can be attributed to the reduced crack closure effects obtained at the higher R-ratio and the decreased non-effective portion ($K_{op} - K_{min}$) of the ΔK range obtained by increasing K_{min}. The relationship between the occurrence of crack closure and the influence of the R-ratio was demonstrated in the present study, where similar log da/dN vs log ΔK_{eff}

curves were obtained for values of R = 0.1 and R = 0.5 for the AC and NSC materials tested in air as well as in the NaCl solution.

On the other hand, increasing the R-ratio from 0.1 to 0.5 appeared to have little influence on the threshold values of the HT materials. This unusual behaviour (which is sufficiently unusual as to justify further verification) therefore suggest that the threshold value of these HT materials is less strongly influenced by the type of crack closure which largely determines the ultra-low da/dN portion of the log da/dN - log ΔK curve for the AC and NSC materials. Based on the results obtained in the present study, the most probable explanation for the lack of influence of the R-ratio on the threshold behaviour of the HT material would be that, for this material, the threshold values are to a much larger extent determined by crack deviation and crack branching effects. The metallographic observations carried out in the region of the crack surface demonstrated the importance of such crack deviation and crack branching effects at low growth rates in the HT materials.

The influence of an increasing grain size to increase the threshold value of stress intensity factor for fatigue crack propagation is probably a combination of three distinct effects. Two of these are often considered in the present literature. These are the influence of the grain size on the surface roughness and roughness-induced crack closure and the influence of crack deviations on the modes I and II components of ΔK. The third effect which appears important is less rarely considered. A crystallographic crack propagating in a polycrystalline material, however, consists of segments within the individual grains which must remain connected at each grain boundary across the specimen thickness. As the grain size increases, the difference in distance (perpendicular to the crack surface) between crystallographic crack fronts in two neighbouring grains tends to increase, requiring

additional energy to maintain such crack segments connected as part of a macroscopic crack front. In the large grain size HT material, the difficulty in joining up the different crack segments at lateral grain boundaries was clearly observable.

4.6 Oscillations in the log da/dN vs log ΔK curves

Some of the curves obtained on the NSC and especially on the HT materials presented oscillations in the log da/dN vs log ΔK curves towards da/dN values of 10^{-6} to 10^{-5} mm/cycle. The growth rate would increase sharply with increasing ΔK and then suddenly decrease by a factor of ≈ 2-5 and then reincrease and again redecrease sharply. This effect was associated with fracture surfaces which presented large facets. Similar effects at similar crack growth rates have been previously observed on other materials having large grain sizes (10,11). In the present study, it was demonstrated by the metallographic observations carried out near the fracture surface that this behaviour was a grain boundary effect associated with very crystallographic cracking. As the crack crosses a boundary between the large β-grain, the orientation of the average crack plane tends to change drastically. Difficulty in crossing such a boundary then results, as observed for the secondary cracks stopping at β-grain boundaries. In the case of the primary crack, this difficulty in crossing the grain boundary often results at low growth rates in the nucleation of several cracks in the β-grain encountered. The important change in orientation of the crack plane on crossing a β-grain boundary strongly influences the mode I and mode II components of ΔK which effectively act in the crack tip region in this new grain. The crack branching that accompanies this change in crack orientation decreases or further decreases the effective value of ΔK for mode I cracking. As a result, a sudden and important decrease in da/dN results. Therefore, when very facetted crack growth is obtained

in large grain size material on ordinary size specimens, such oscillations in da/dN can be expected slightly above the threshold region. Increasing the specimen thickness should reduce the relative influence of the encounters with the individual β-grain boundaries on the macroscopic crack propagation rate.

4.7 The influence of the Mn content

The difference in Mn content in general shows little influence on the fatigue crack growth results other than in the threshold region for the AC and HT conditions. For the AC condition, the 14% Mn material generally had higher threshold values than the 12% Mn alloy, which is opposite to the behaviour expected based on consideration of the β grain size. The AC materials present a relatively fine β grain size and a relatively small facet size. One possible explanation is that for these grain sizes, the corrosion-product wedging effect is relatively more important than for the larger β grain sizes for the other conditions tested and that a thicker corrosion product is produced for the 14% Mn alloy. For the larger grain size, the roughness induced crack closure effects cause more important premature contact of the opposite fracture surfaces at asperities. The corrosion product tending to accumulate in depressions on the fracture surface then is less effective in contributing to the crack closure. Although not as important as that produced in the NaCl solution, the low fatigue crack growth rates also produce a significant thickness of corrosion product in air. This explanation is suggested by the larger difference in the 14% Mn alloy between the threshold values in air and in the 3.5% NaCl solution. For the HT material and their larger β-grain sizes, it is the 12% Mn alloy which gives the higher threshold values, as can be explained by the influence of grain size.

Some of the results in the salt solution suggest a slightly more important corrosion-fatigue effect for the 14% Mn alloy, while other results (for example, the tests on the NSC materials in 3.5% NaCl solution at R = 0.5 and f = 1 Hz) show essentially identical log da/dN vs log ΔK curves for the two alloy compositions.

5. CONCLUSIONS

From the present study the following conclusions can be drawn:

1. Corrosion-fatigue crack propagation occurs at high growth rates in the two Mn-Ni-Al bronzes studied whether in the as-cast (AC), normalized (NSC) or heat-treated at 690°C (HT) conditions. In the AC and NSC conditions, corrosion-fatigue causes fine slots to proceed ahead of the macroscopic crack front along α-β interfaces,which aids the nucleation of fatigue cracking in α-grains ahead of this macroscopic crack front. In the HT condition, corrosion-fatigue also results from facilitated initiation of fatigue cracking in the α-grains. For this material condition in which important amounts of cracking occurs in the β-phase, the presence of the α-grains hinders the fatigue crack propagation in air, especially for the 12% Mn alloy where the β-ligaments between the α-grains is smaller, thus permitting a more important influence of the cracking in the α-grains.

2. At the low growth rates, fatigue crack propagation for a given ΔK value occurs more slowly and the ΔK_{th} values are higher in the NaCl solution than in air. As well, for these rates, the log da/dN vs log ΔK curves obtained in air tend to present a very steep slope. These effects are shown macrofractographically to be associated with important corrosion product induced crack closure effects. This corrosion product appears to have the characteristics of that produced by fretting corrosion. The threshold values obtained in the NaCl solution are to a large extent controlled by the importance of the crack closure effects in the AC and NSC materials.

3. The threshold values obtained in air are to an important extent controlled by the β-grain size and three different contributions to this influence of grain size are proposed. For the HT materials, crack branching and crack deviation effects are particularly important and little influence of the R-ratio on the threshold value was obtained for this condition.

4. The present study demonstrated the feasibility of employing best-fit techniques to determine K_{op} and ΔK_{eff} values in a completely objective manner.

5. The curves of log da/dN vs ΔK_{eff} values demonstrate that the corrosion-fatigue accelerated crack propagation can best be seen on a ΔK_{eff} basis, since the more important corrosion-product induced crack closure effects partially mask the corrosion fatigue effects when the crack growth rates are compared on a ΔK basis.

6. The comparison of the crack growth data on a ΔK basis demonstrate that, for tests in air and in 3.5% NaCl solution, the influence of the R-ratio on the crack growth rates for the AC and NSC materials results simply from the influence of an increased R-ratio to decrease the ineffective portion of ΔK.

7. At least for the AC and NSC materials, a decrease in cycling frequency from 20 Hz to 1 Hz results in an increase in the crack propagation rate for the higher values of ΔK, which effect is typical of corrosion-fatigue.

8. The higher resistance to fatigue crack propagation for the HT alloys compared to the AC and NSC alloys is associated with the

important amounts of crack propagation in the β-phase in these HT alloys. As well, the duplex microstructure of these alloys causes the α-grains to hinder the fatigue crack propagation for tests carried out in air, especially in the case of the 12% Mn alloy in the HT condition. For the 14% Mn alloy, the larger β-grain ligaments between α-grains appear to decrease somewhat the relative influence of the α-grains.

9. For the NSC and HT alloys which have large β-grain sizes, a number of the log da/dN vs log ΔK curves presented oscillations in da/dN towards rates of 10^{-6} - 10^{-5} mm/cycle. It was demonstrated that this effect is associated with difficulty that the crack encounters in crossing β-grain boundaries at these rather low growth rates. Crack deviation and crack branching result on crossing such grain boundaries at these da/dN values but are less important at higher da/dN values.

10. Other than in the threshold region, there was little influence of the Mn content (12% as compared to 14%) on the crack propagation results. For the AC condition, the threshold values are higher for the 14% Mn alloy, which may be a result of a more important corrosion product wedging effect for this alloy. For the HT condition, the threshold values are higher for the 12% Mn alloy, which effect is related to its larger β-grain size and larger fracture facet size.

ACKNOWLEDGMENTS

The authors wish to thank Messrs Jean Claudinon, Jean-Philippe Bouchard, Jacques Desrochers, René Veillette and Gérard Guérin, who provided technical help during the course of the present study.

This work was performed for the Physical Metallurgy Research Laboratories, CANMET, Energy, Mines and Resources Canada under Supply and Services Canada Contract 03SQ.23440-2-9017. The authors are indebted to PMRL, CANMET for the provision of experimental materials. The authors also acknowledge the support received from Dr. M. Sahoo, PMRL, in the scientific administration of the contract.

Any data presented, opinions, findings, conclusions, or recommendations expressed in this report are those of the authors and do not necessarily reflect the views of CANMET.

Crown copyright of this report is reserved.

REFERENCES

1. P. COLLINS and D.J. DUQUETTE, Corrosion (NACE), 34, (1978) 119.

2. J.S. MSHANA, O. VOSIKOVSKY and M. SAHOO, Canadian Metallurgical Quarterly, 23 (1984) 7.

3. D. TAYLOR and J.F. KNOTT, Metals Technology, 9 (1982) 221.

4. R.N. PARKINS and Y. SUZUKI, Corrosion Science, 23 (1983) 577.

5. J.I. DICKSON, L. HANDFIELD, J.P. BAÏLON and M. SAHOO, Fatigue 84, Proceedings of an International Conference, Birmingham, England, September 1984, in press, EMAS Ltd Publishers.

6. A. COUTURE and M. SAHOO "Ice-Breaker Propellers" Copper Symposium, CIM Conference of Metallurgists, Quebec, August 1984.

7. Y. BLANCHETTE, L. HANDFIELD, J.I. DICKSON and J.P. BAÏLON, to be published.

8. C. BATHIAS in "La fatigue des matériaux et des structures", Chapiter 5, Maloine S.A., Paris, p. 163 (1980).

9. S. SURESH, presented at "Fatigue 84",, Birmingham, England, September 1984, published in Conference Proceedings, EMAS LTD, (1985).

10. D. TROMANS, University of British Columbia, personnal communication.

11. M.AIT BASSIDI, Ph. D. Thesis, École Polytechnique de Montréal, (1984).

CDT
Centre de
Développement
Technologique
École Polytechnique
de Montréal

APPENDIX

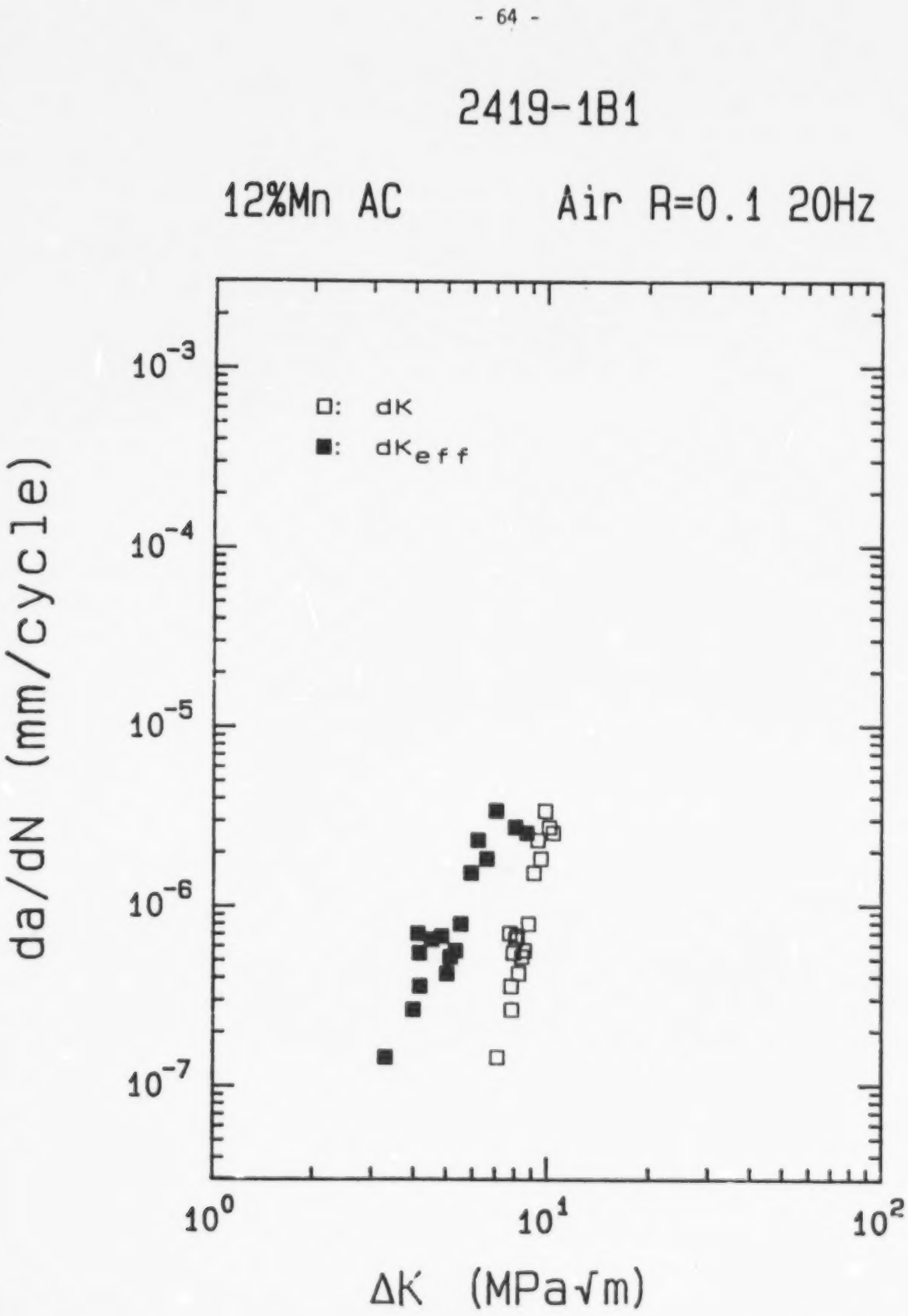
2419-1B1
12%Mn AC
Air R=0.1 20Hz
□: dK
■: dK$_{eff}$
da/dN (mm/cycle)
10^{-3}
10^{-4}
10^{-5}
10^{-6}
10^{-7}
10^{0}
10^{1}
10^{2}
ΔK (MPa√m)

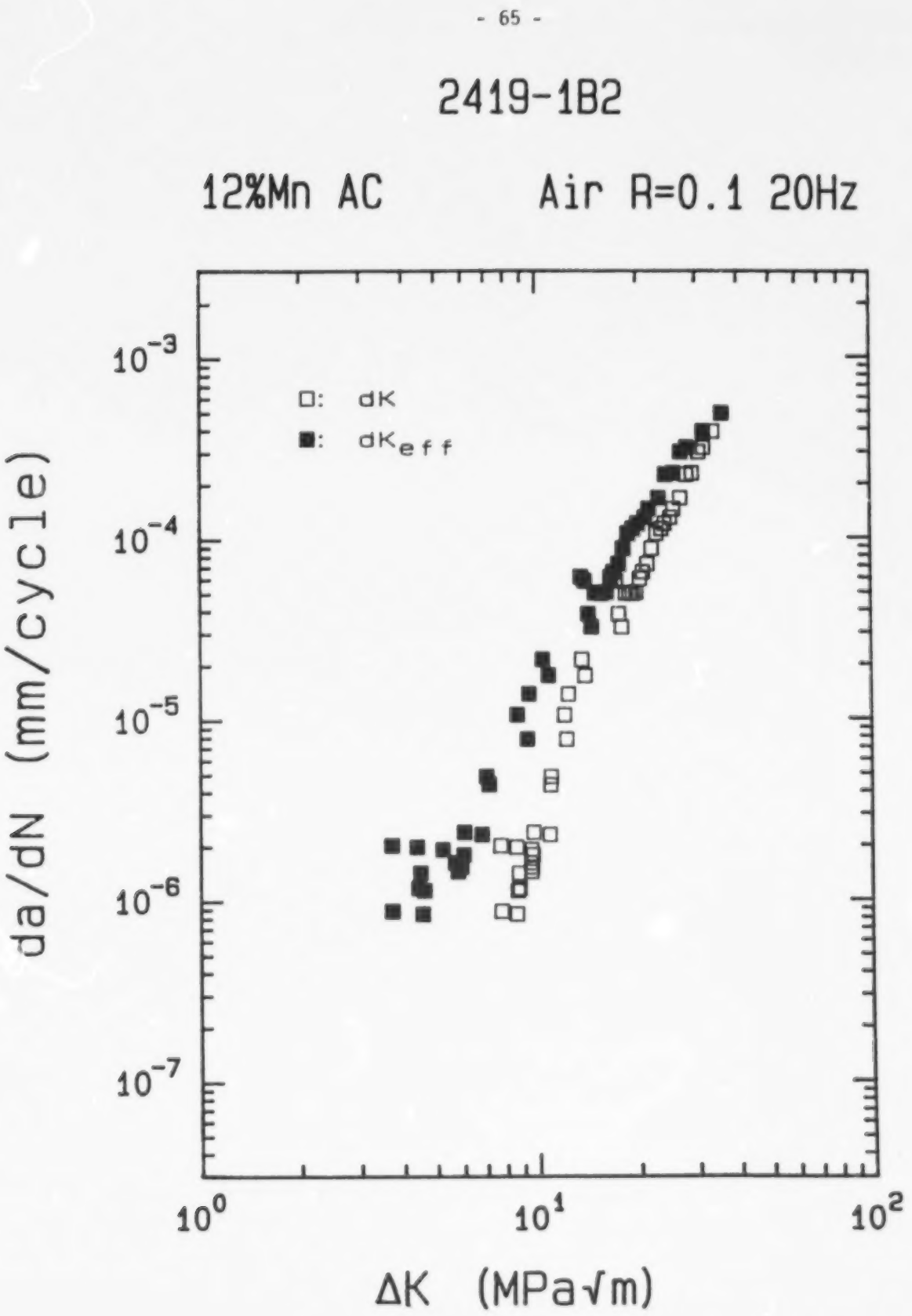
2419-1B2
12%Mn AC
Air R=0.1 20Hz
□: dK
■: dK eff
da/dN (mm/cycle)
10^-3
10^-4
10^-5
10^-6
10^-7
10^0
10^1
10^2
ΔK (MPa√m)

2419-1B2

12% Mn AC Air R=0.1 20Hz

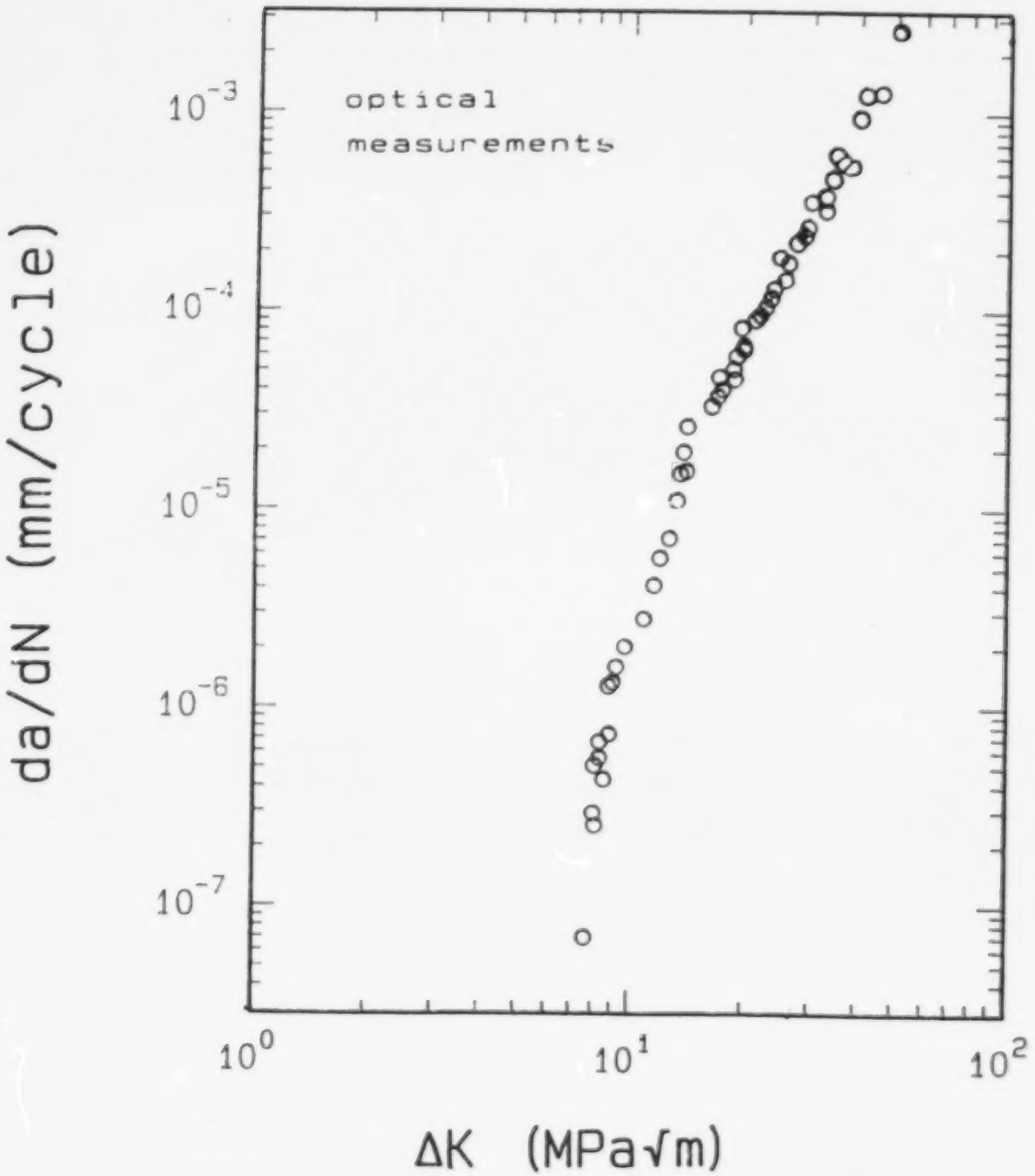

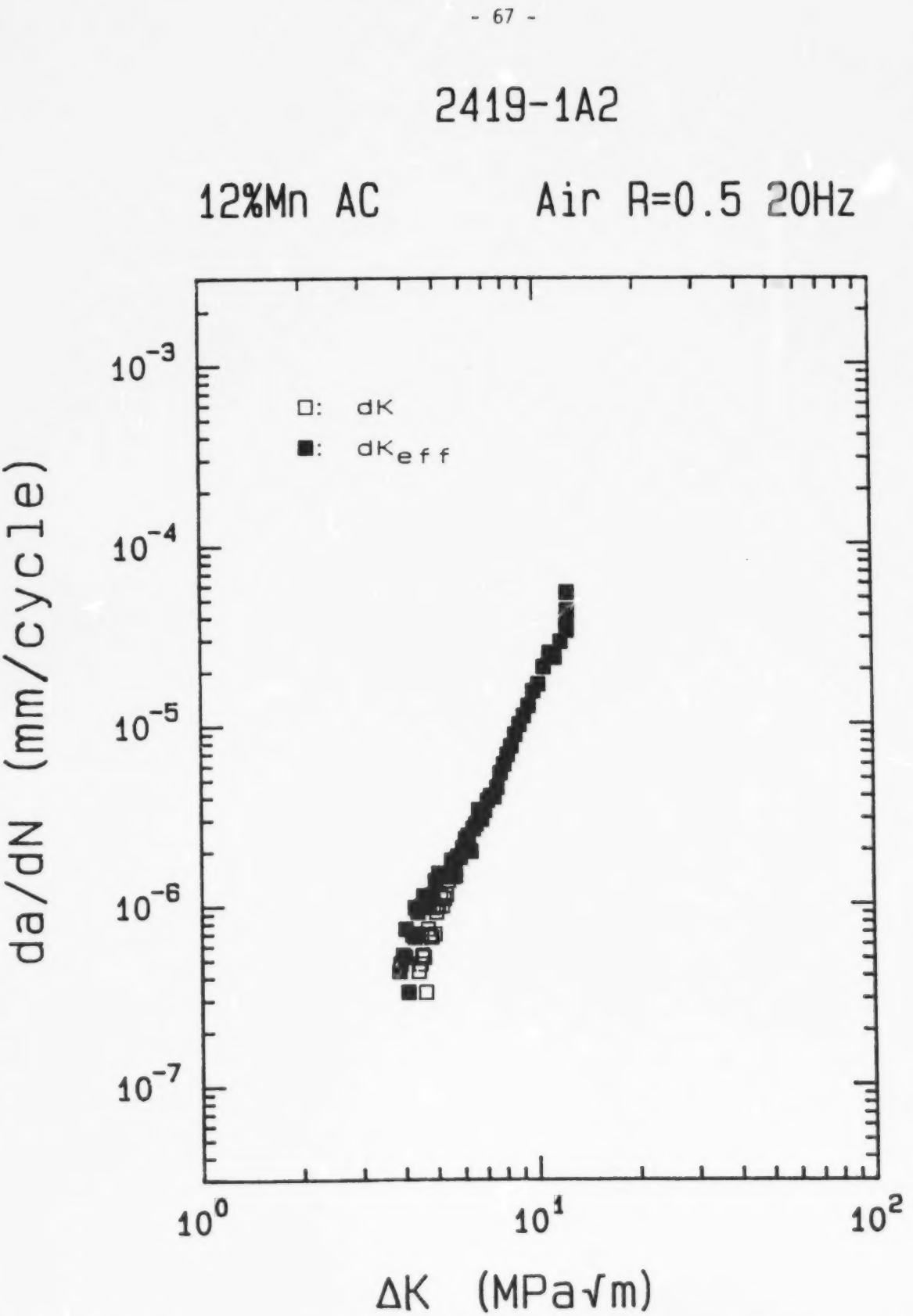
2419-1A2
12%Mn AC
Air R=0.5 20Hz
□: dK
■: dK$_{eff}$
da/dN (mm/cycle)
10^{-3}
10^{-4}
10^{-5}
10^{-6}
10^{-7}
10^{0}
10^{1}
10^{2}
ΔK (MPa√m)

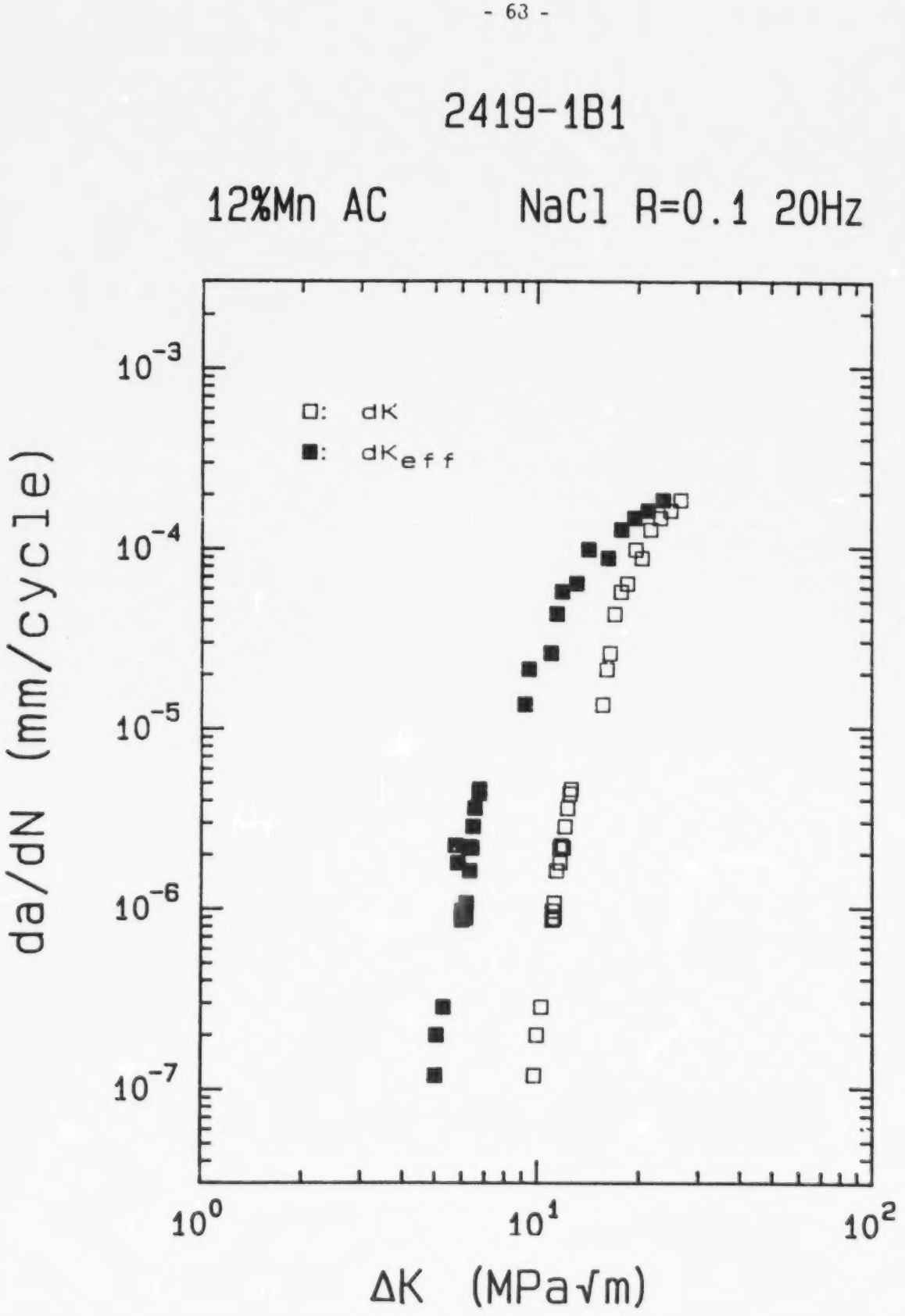
2419-1B1
12%Mn AC
NaCl R=0.1 20Hz
□: dK
■: dK eff
da/dN (mm/cycle)
10-3
10-4
10-5
10-6
10-7
100
101
102
ΔK (MPa√m)

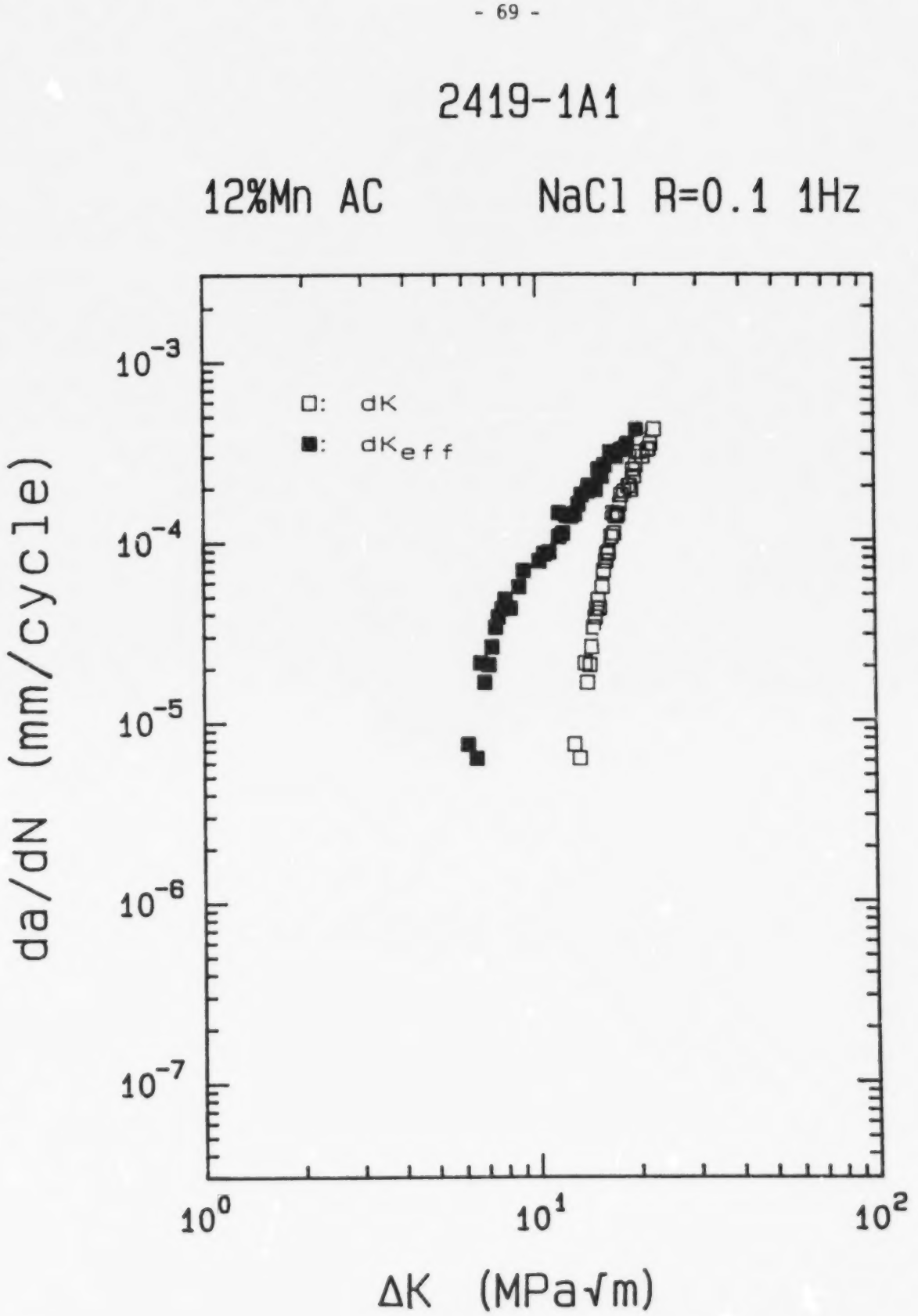
2419-1A1
12%Mn AC
NaCl R=0.1 1Hz
□: dK
■: dK eff
da/dN (mm/cycle)
10^-3
10^-4
10^-5
10^-6
10^-7
10^0
10^1
10^2
ΔK (MPa√m)

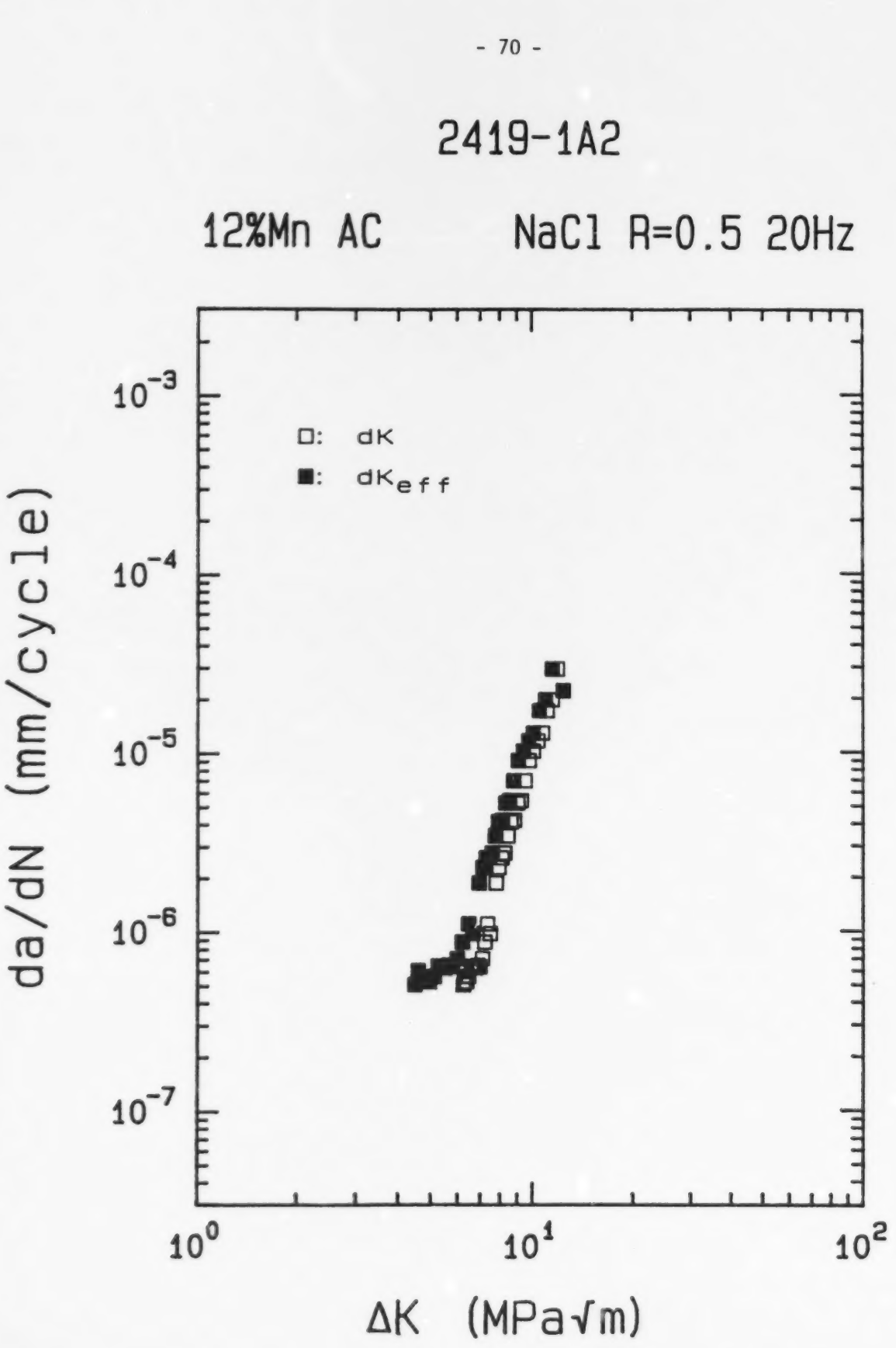
2419-1A2
12%Mn AC
NaCl R=0.5 20Hz
□: dK
■: dK eff
da/dN (mm/cycle)
10^-3
10^-4
10^-5
10^-6
10^-7
10^0
10^1
10^2
ΔK (MPa√m)

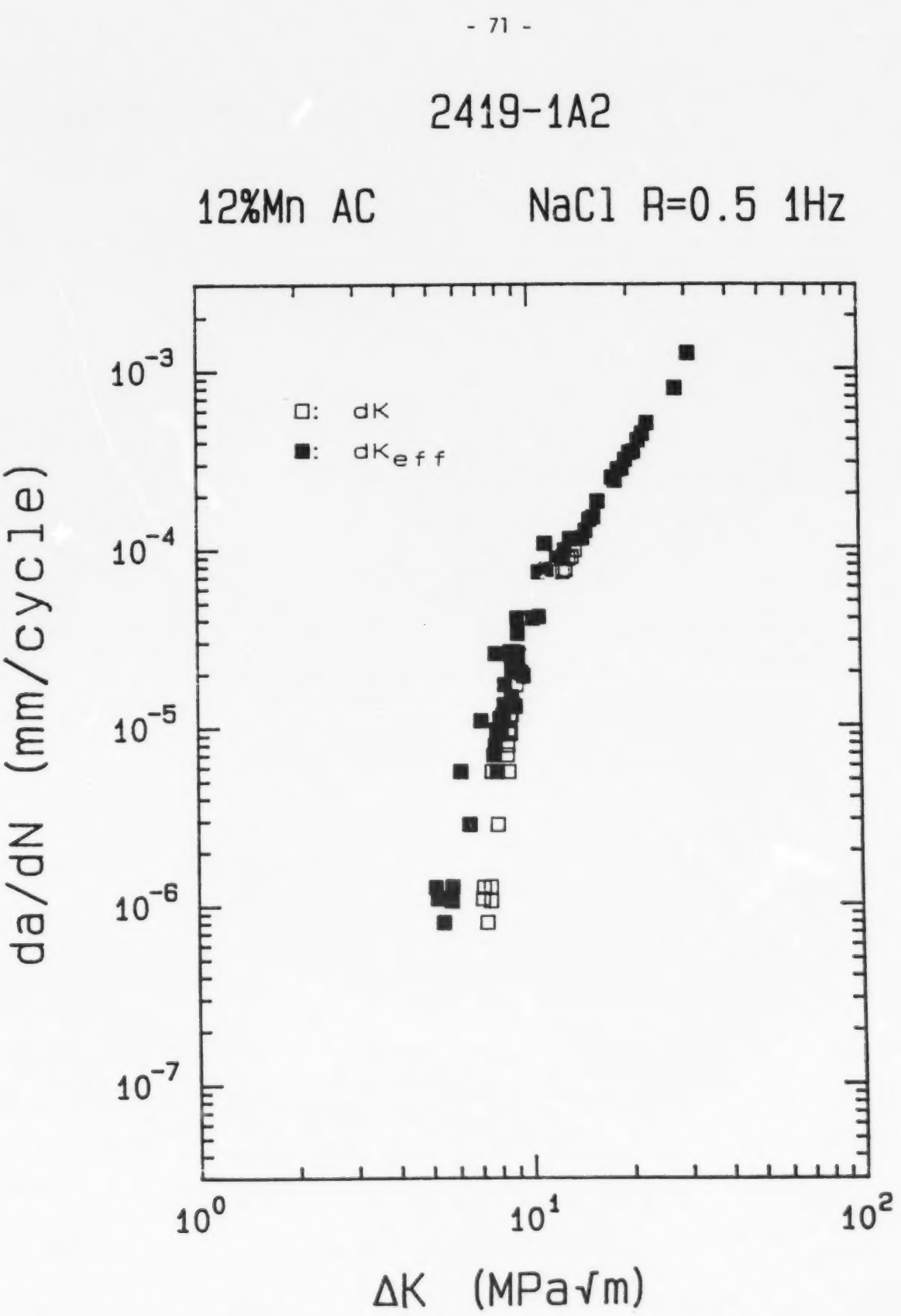
2419-1A2
12%Mn AC
NaCl R=0.5 1Hz
□: dK
■: dK$_{eff}$
da/dN (mm/cycle)
10^{-3}
10^{-4}
10^{-5}
10^{-6}
10^{-7}
10^{0}
10^{1}
10^{2}
ΔK (MPa√m)

2628-1A2

12%Mn NSC Air R=0.1 20Hz

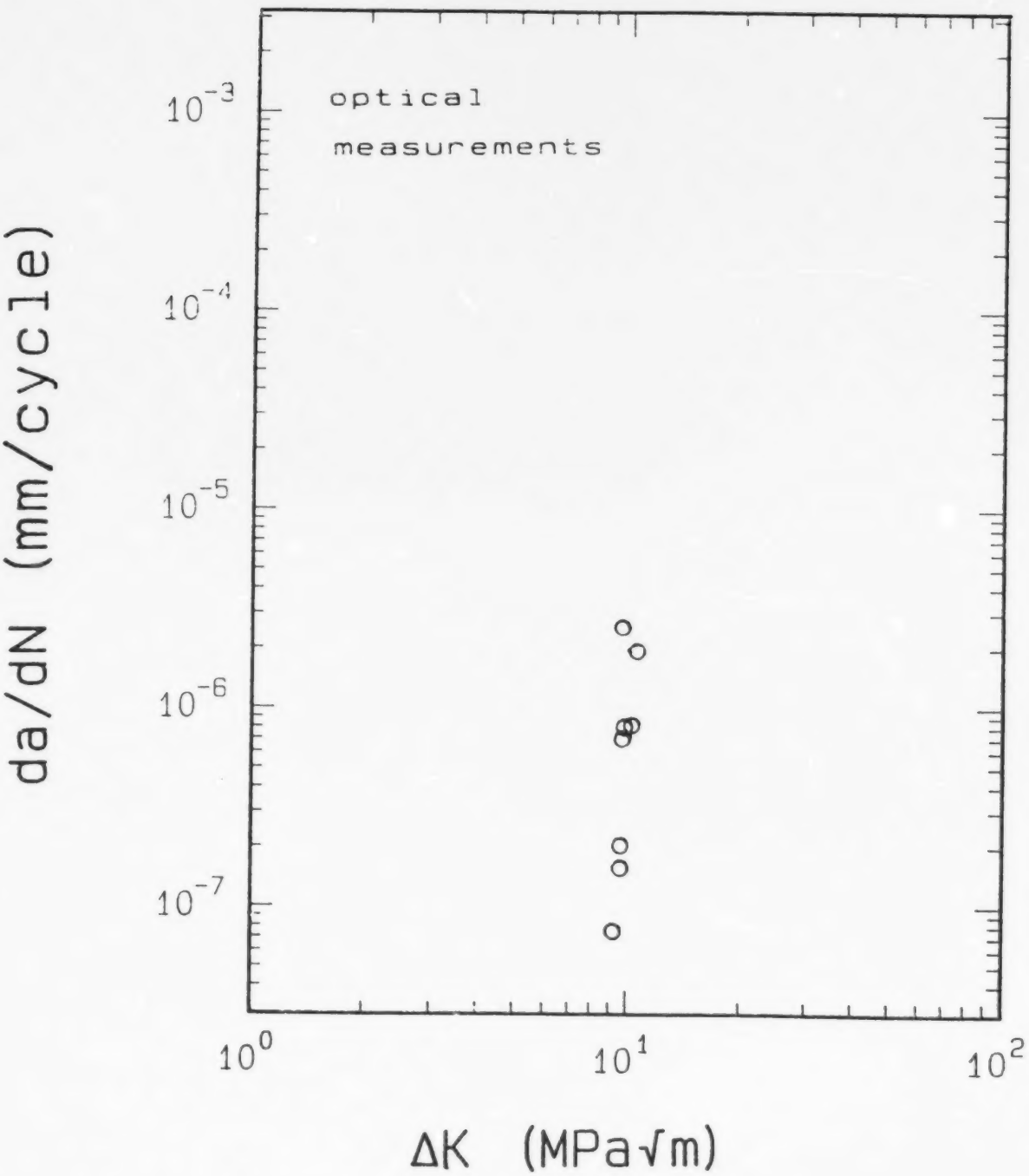

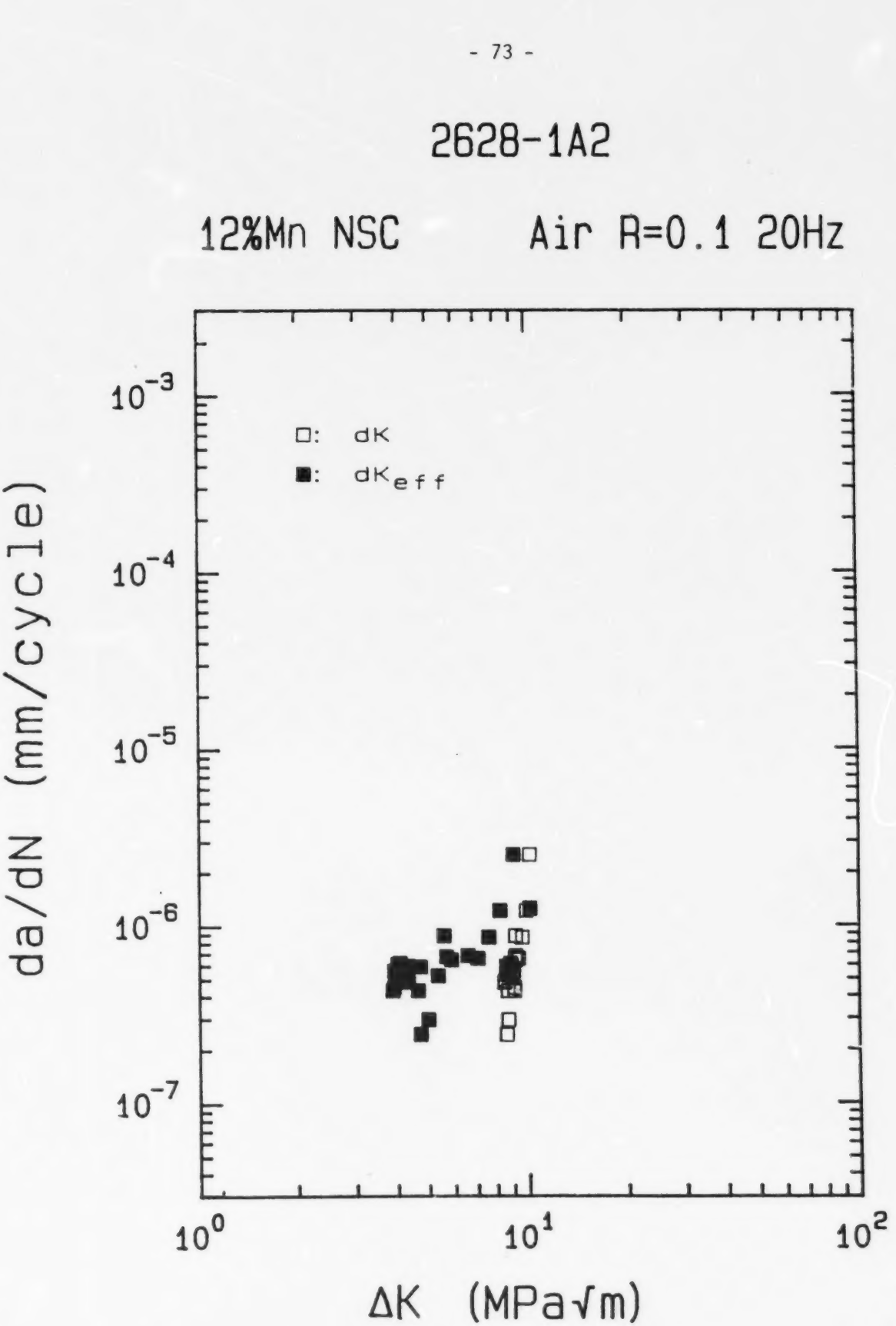
2628-1A2
12%Mn NSC
Air R=0.1 20Hz
□: dK
■: dK eff
da/dN (mm/cycle)
10^-3
10^-4
10^-5
10^-6
10^-7
10^0
10^1
10^2
ΔK (MPa√m)

2628-1A1

12%Mn NSC Air R=0.1 20Hz

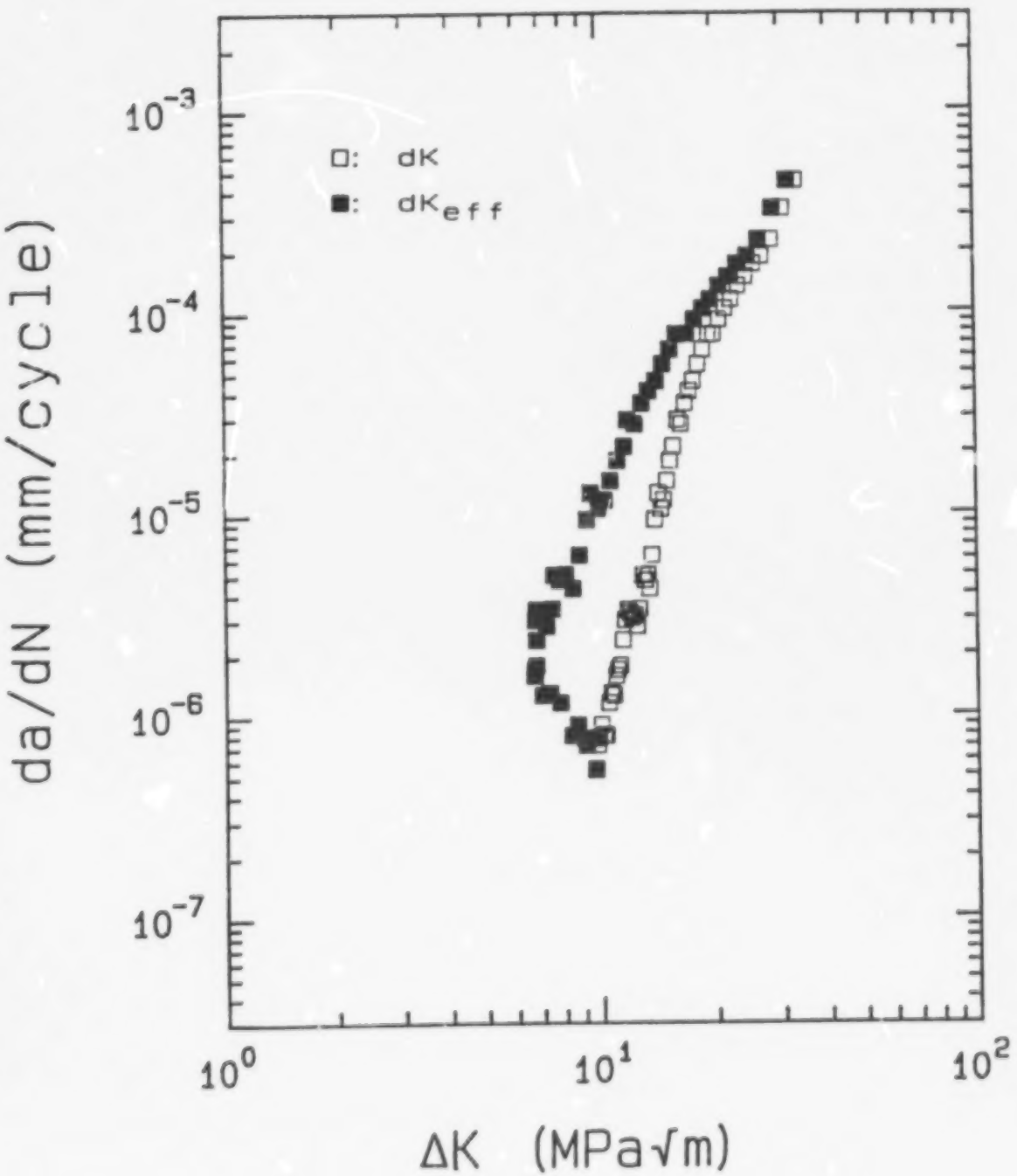

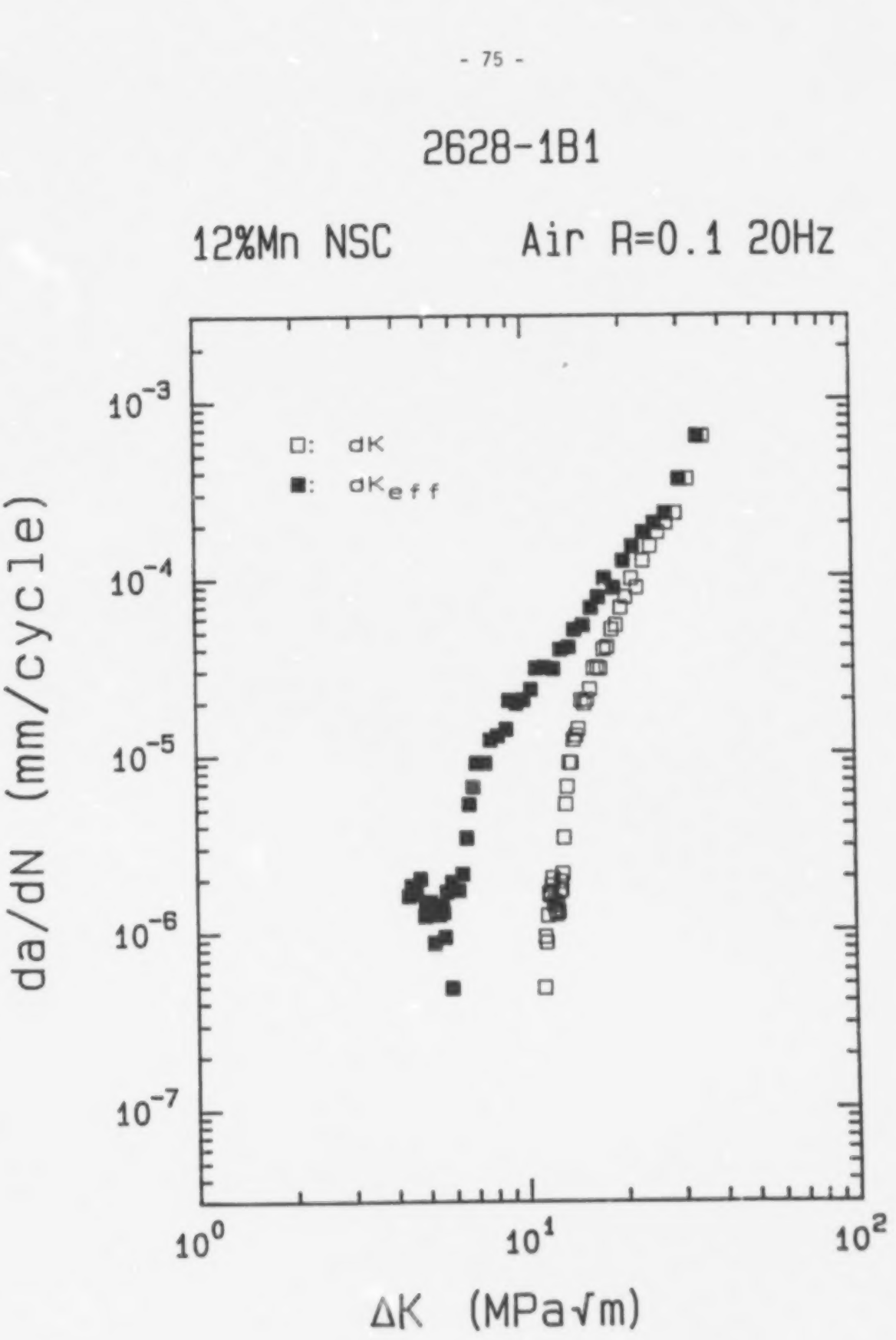
2628-1B1
12%Mn NSC
Air R=0.1 20Hz
□: dK
■: dK$_{eff}$
da/dN (mm/cycle)
10^{-3}
10^{-4}
10^{-5}
10^{-6}
10^{-7}
10^{0}
10^{1}
10^{2}
ΔK (MPa√m)

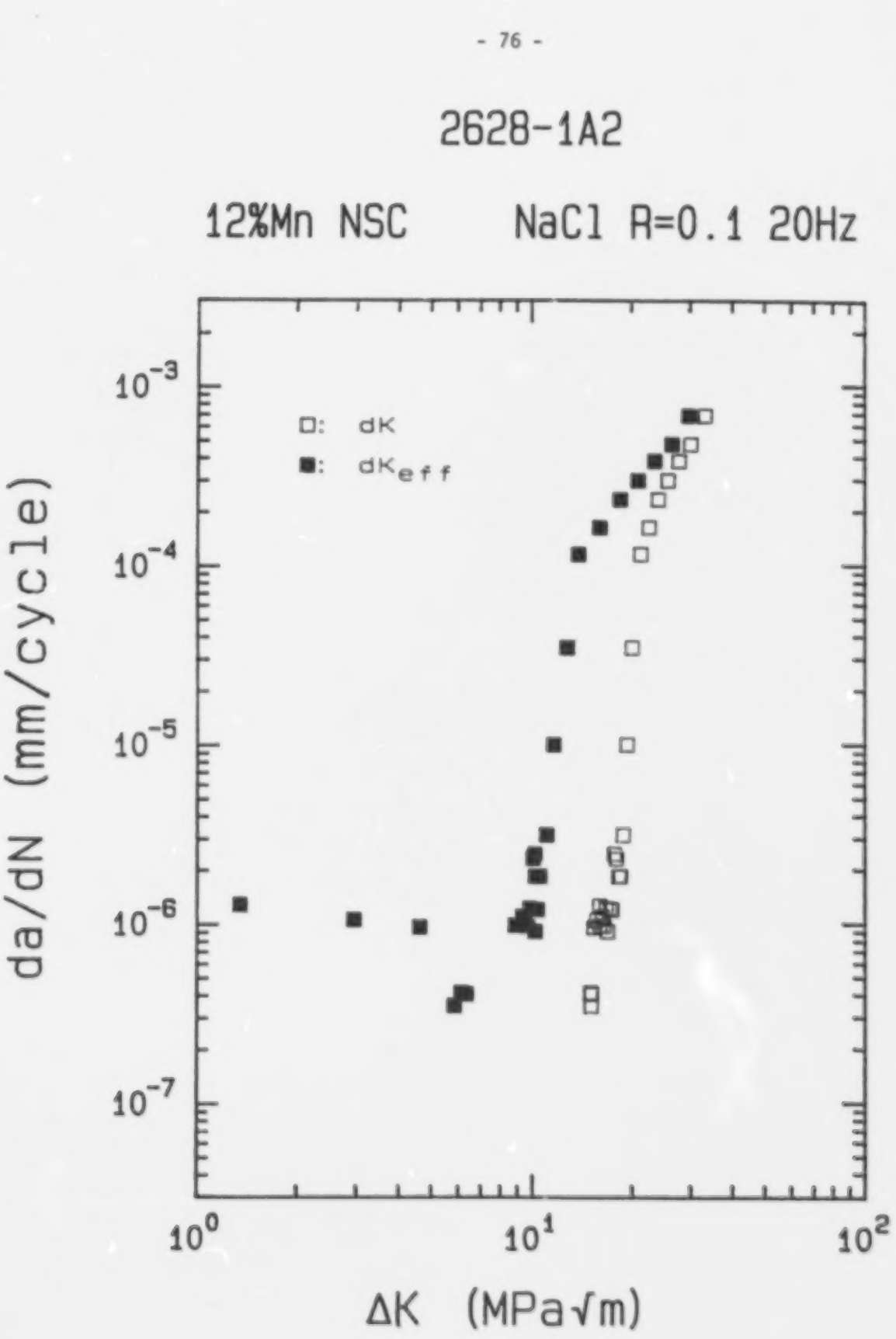
2628-1A2
12%Mn NSC
NaCl R=0.1 20Hz
□: dK
■: dK$_{eff}$
da/dN (mm/cycle)
10^{-3}
10^{-4}
10^{-5}
10^{-6}
10^{-7}
10^{0}
10^{1}
10^{2}
ΔK (MPa√m)

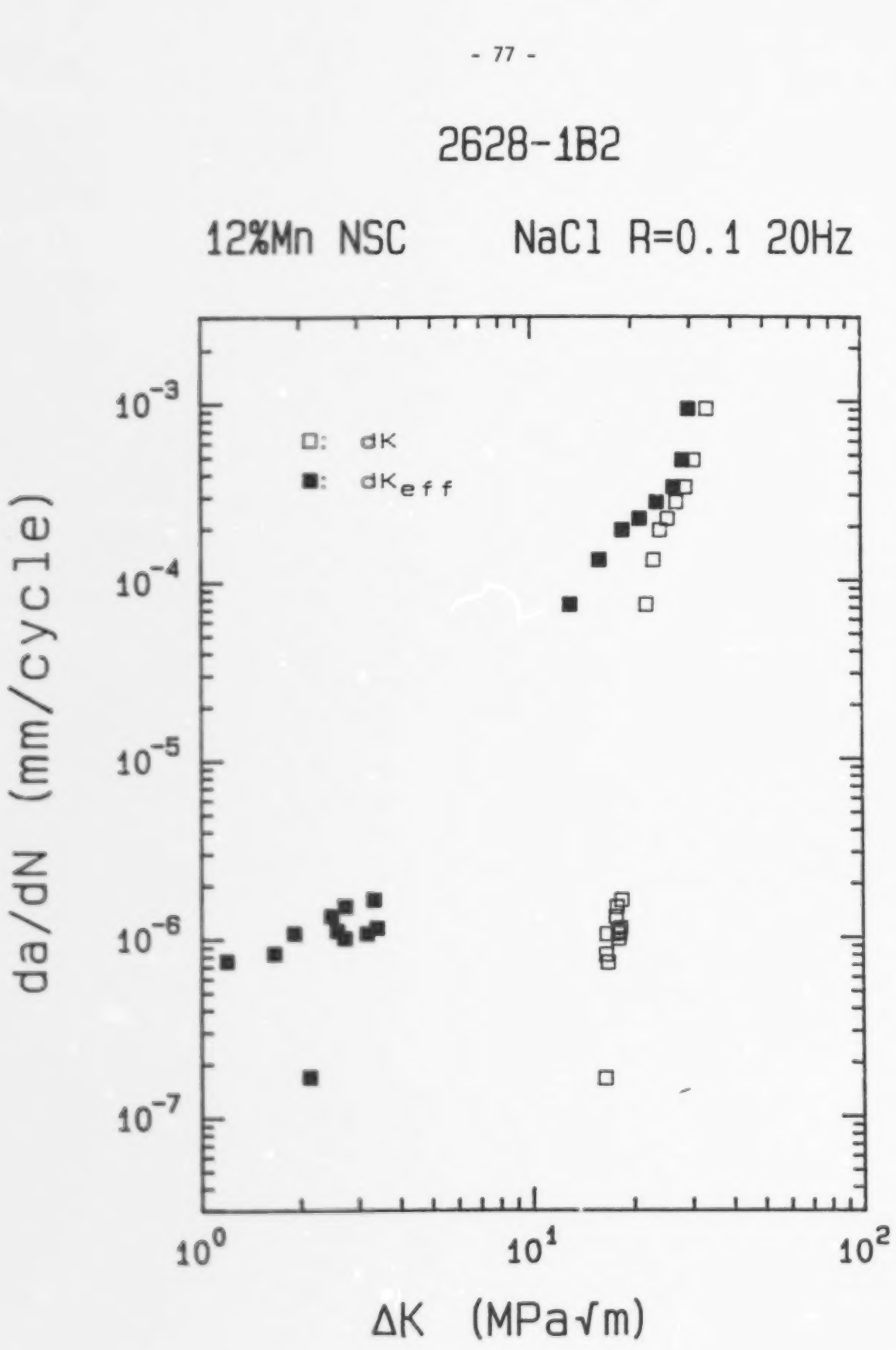
2628-1B2
12%Mn NSC
NaCl R=0.1 20Hz
□: dK
■: dKeff
da/dN (mm/cycle)
10-3
10-4
10-5
10-6
10-7
10^0
10^1
10^2
ΔK (MPa√m)

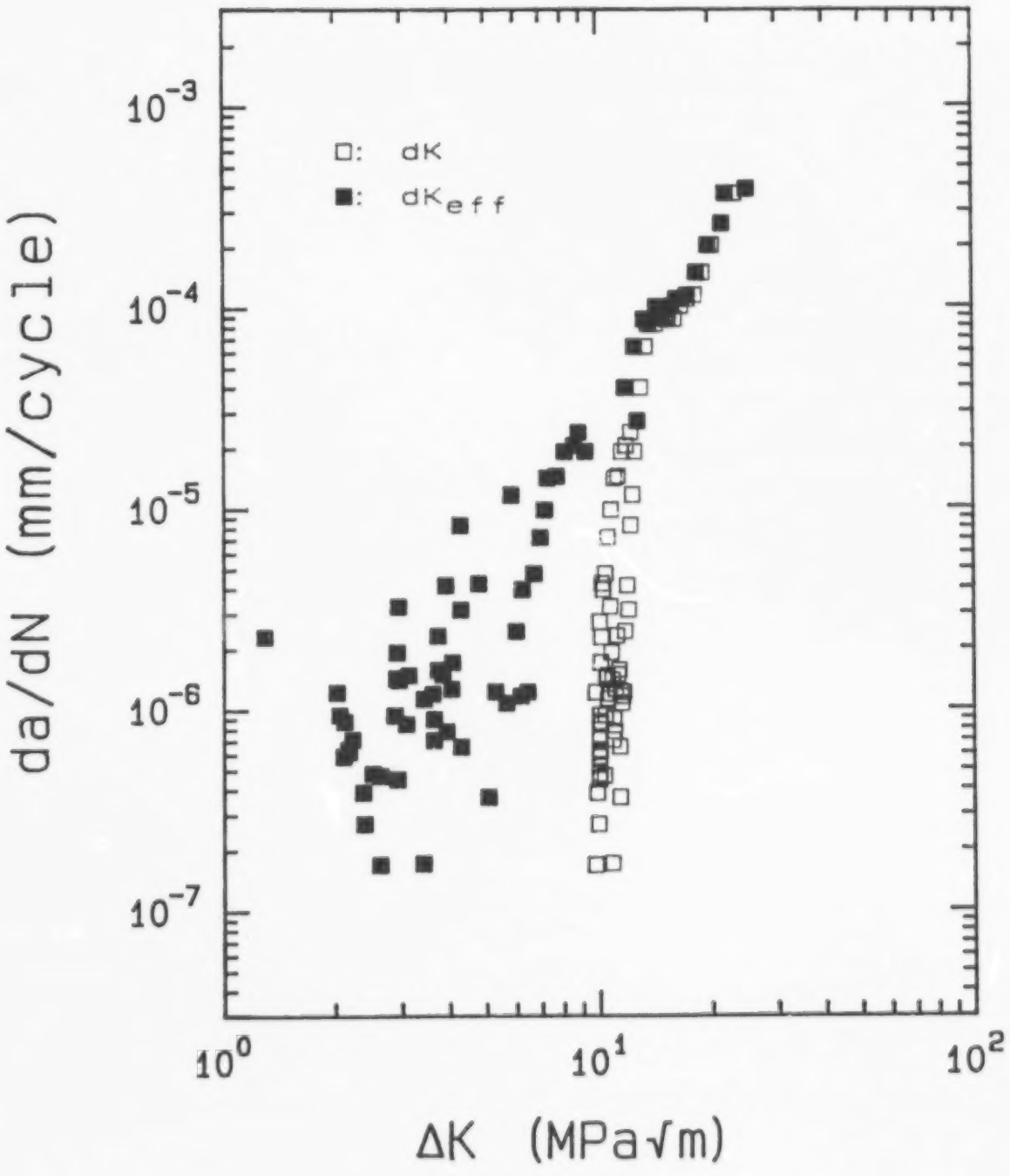
2628-2A2
12%Mn NSC NaCl R=0.5 20Hz
□: dK
■: dK$_{eff}$
da/dN (mm/cycle)
10^{-3}
10^{-4}
10^{-5}
10^{-6}
10^{-7}
10^{0}
10^{1}
10^{2}
ΔK (MPa√m)

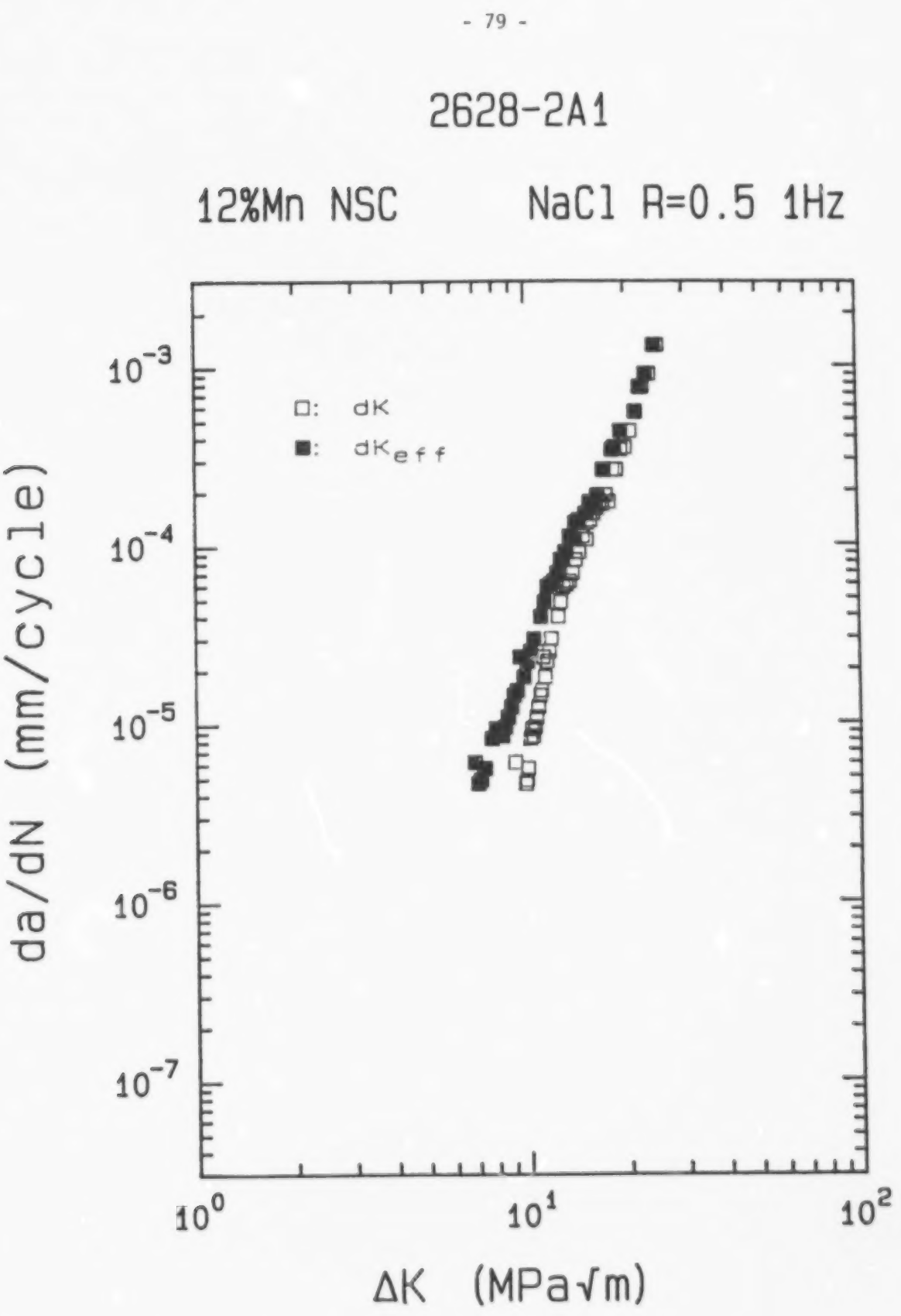
2628-2A1
12%Mn NSC
NaCl R=0.5 1Hz
□: dK
■: dK$_{eff}$
da/dN (mm/cycle)
10^{-3}
10^{-4}
10^{-5}
10^{-6}
10^{-7}
10^{0}
10^{1}
10^{2}
ΔK (MPa√m)

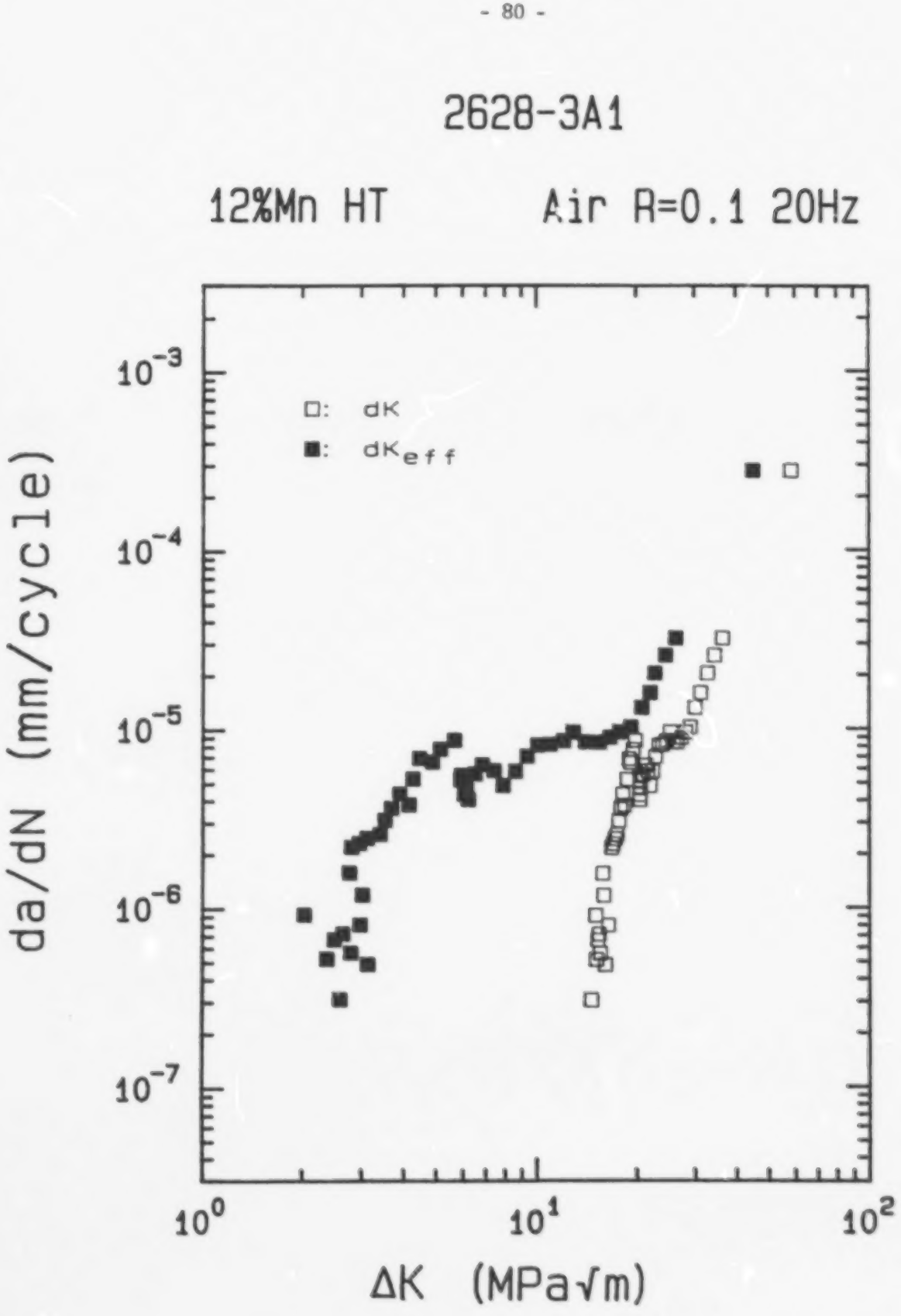
2628-3A1
12%Mn HT
Air R=0.1 20Hz
□: dK
■: dK eff
da/dN (mm/cycle)
10^-3
10^-4
10^-5
10^-6
10^-7
10^0
10^1
10^2
ΔK (MPa√m)

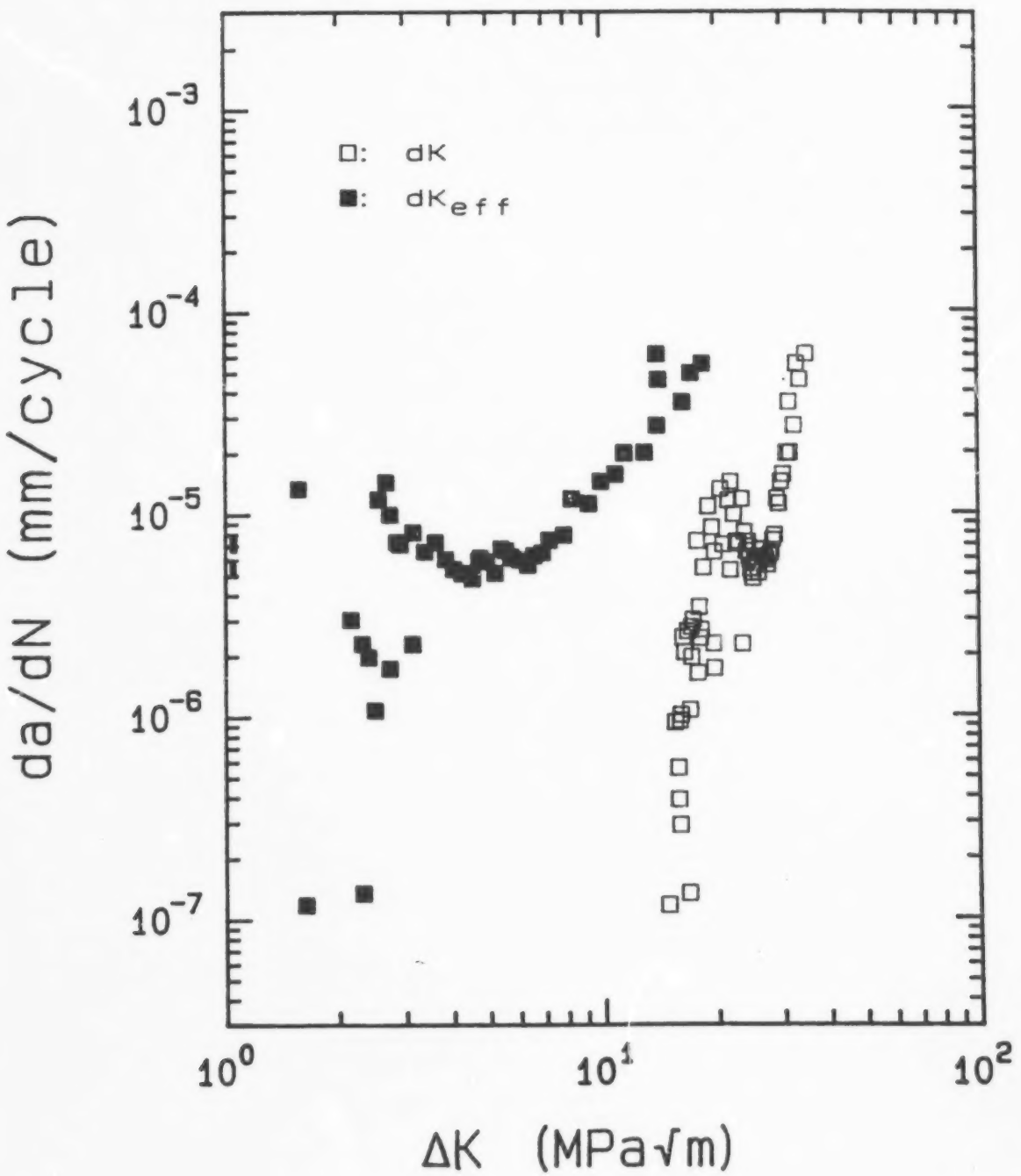
2628-3A3
12%Mn HT
Air R=0.1 20Hz
□: dK
■: dK eff
da/dN (mm/cycle)
10^-3
10^-4
10^-5
10^-6
10^-7
10^0
10^1
10^2
ΔK (MPa√m)

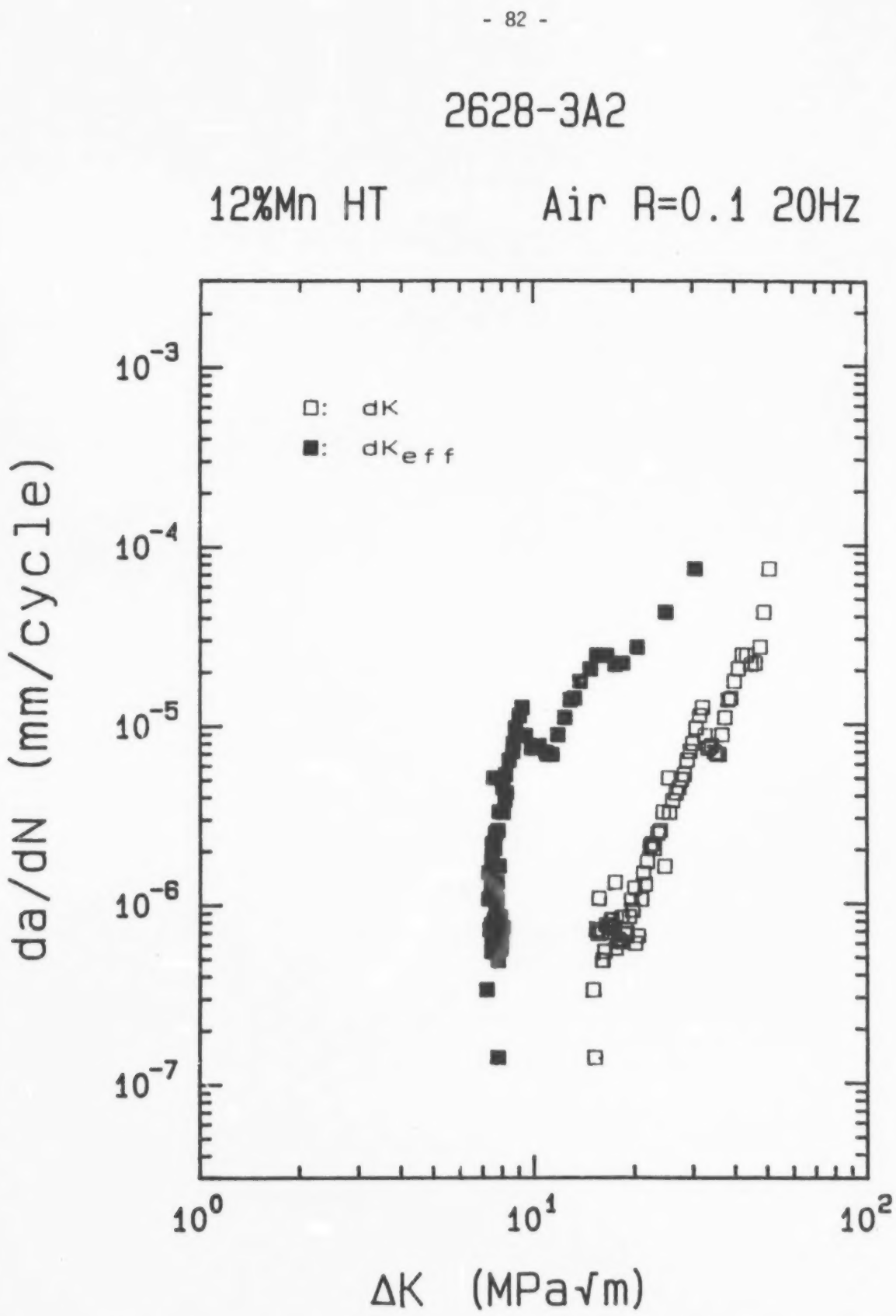
2628-3A2
12%Mn HT
Air R=0.1 20Hz
□: dK
■: dK eff
da/dN (mm/cycle)
10^-3
10^-4
10^-5
10^-6
10^-7
10^0
10^1
10^2
ΔK (MPa√m)

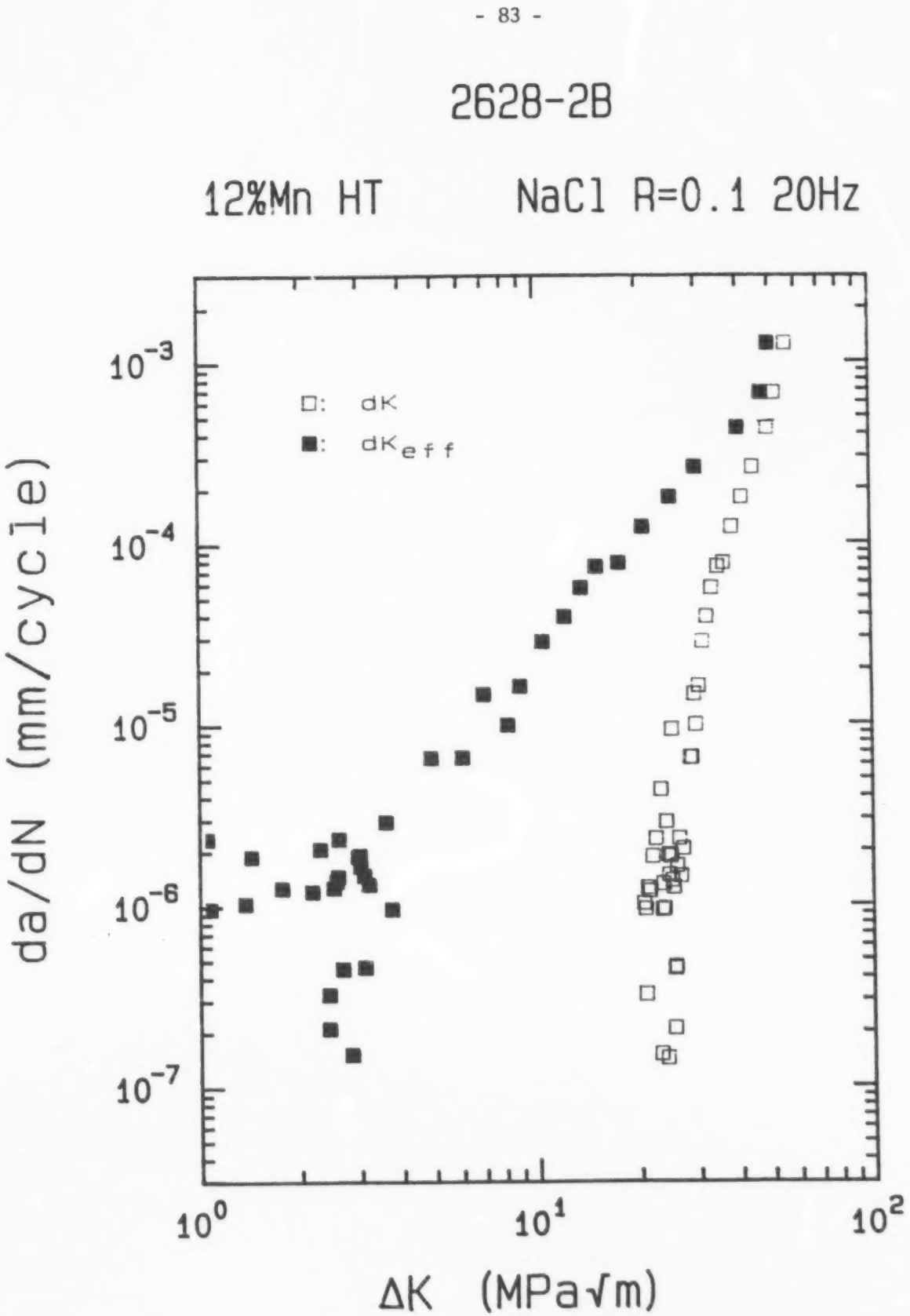
2628-2B
12%Mn HT
NaCl R=0.1 20Hz
□: dK
■: dK eff
da/dN (mm/cycle)
10^-3
10^-4
10^-5
10^-6
10^-7
10^0
10^1
10^2
ΔK (MPa√m)

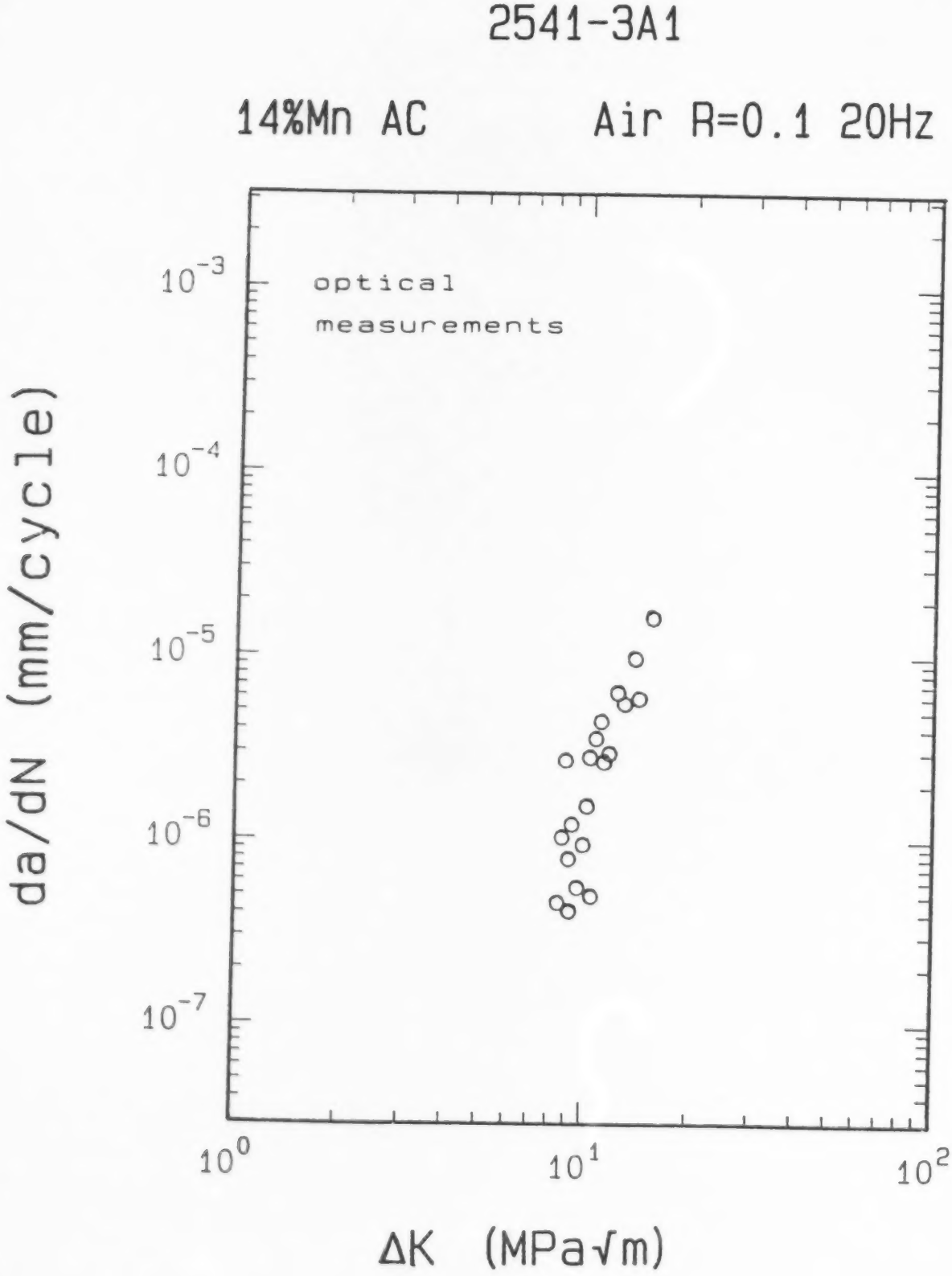
2541-3A1
14%Mn AC
Air R=0.1 20Hz
optical
measurements
da/dN (mm/cycle)
10^{-3}
10^{-4}
10^{-5}
10^{-6}
10^{-7}
10^{0}
10^{1}
10^{2}
ΔK (MPa√m)

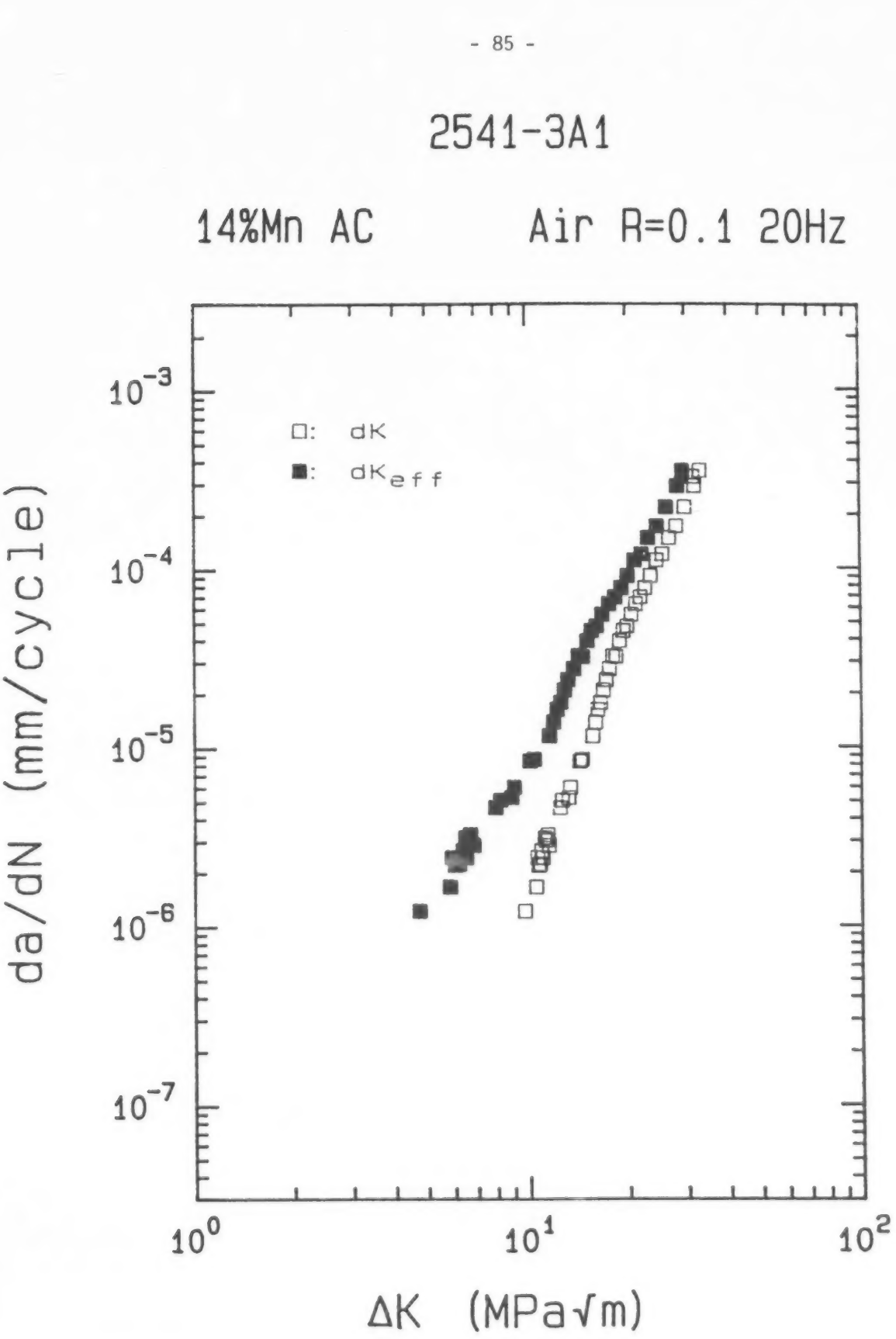
2541-3A1
14%Mn AC
Air R=0.1 20Hz
□: dK
■: dKeff
da/dN (mm/cycle)
10-3
10-4
10-5
10-6
10-7
100
101
102
ΔK (MPa√m)

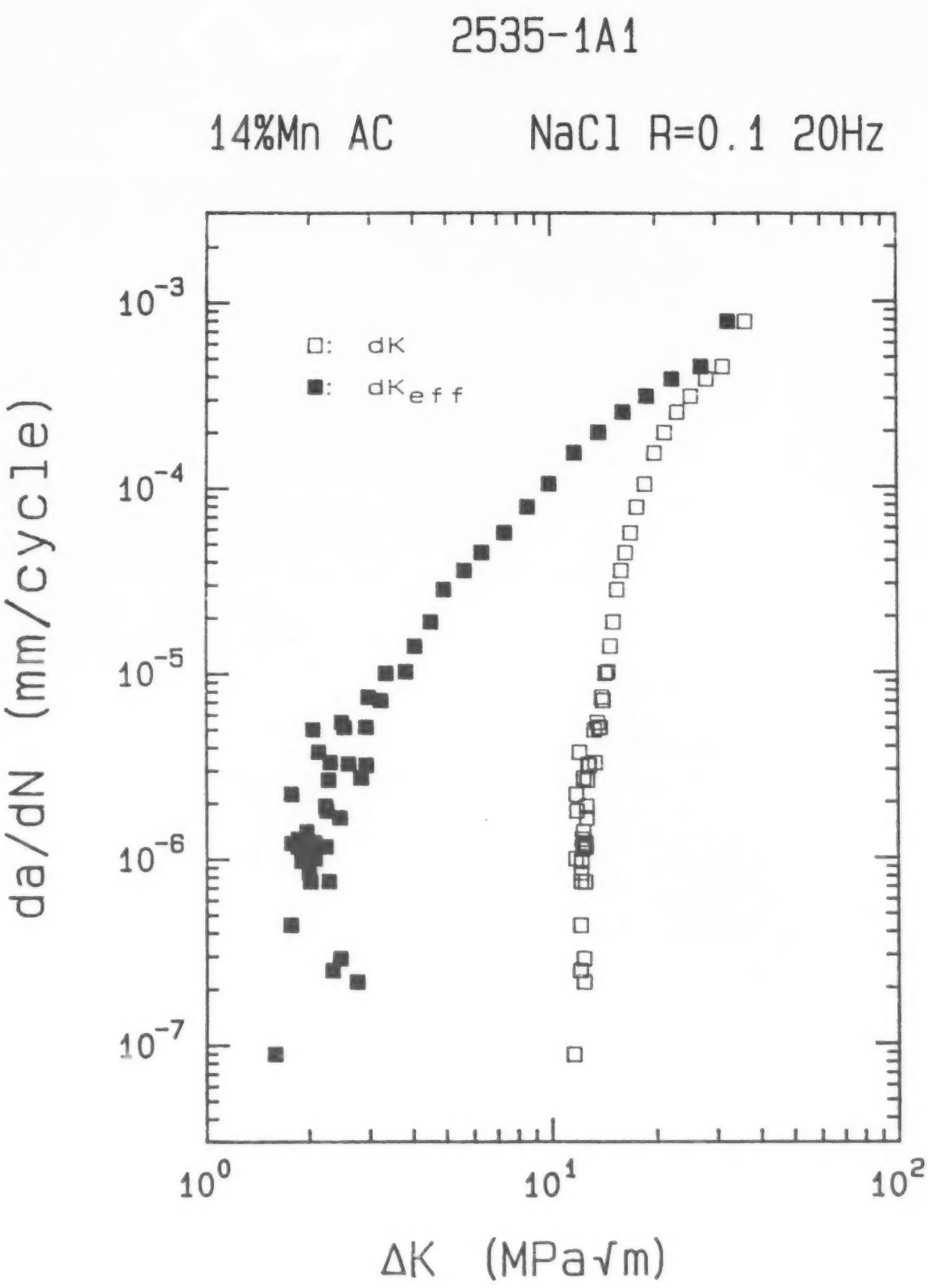
2535-1A1
14%Mn AC
NaCl R=0.1 20Hz
□: dK
■: dK eff
da/dN (mm/cycle)
10^-3
10^-4
10^-5
10^-6
10^-7
10^0
10^1
10^2
ΔK (MPa√m)

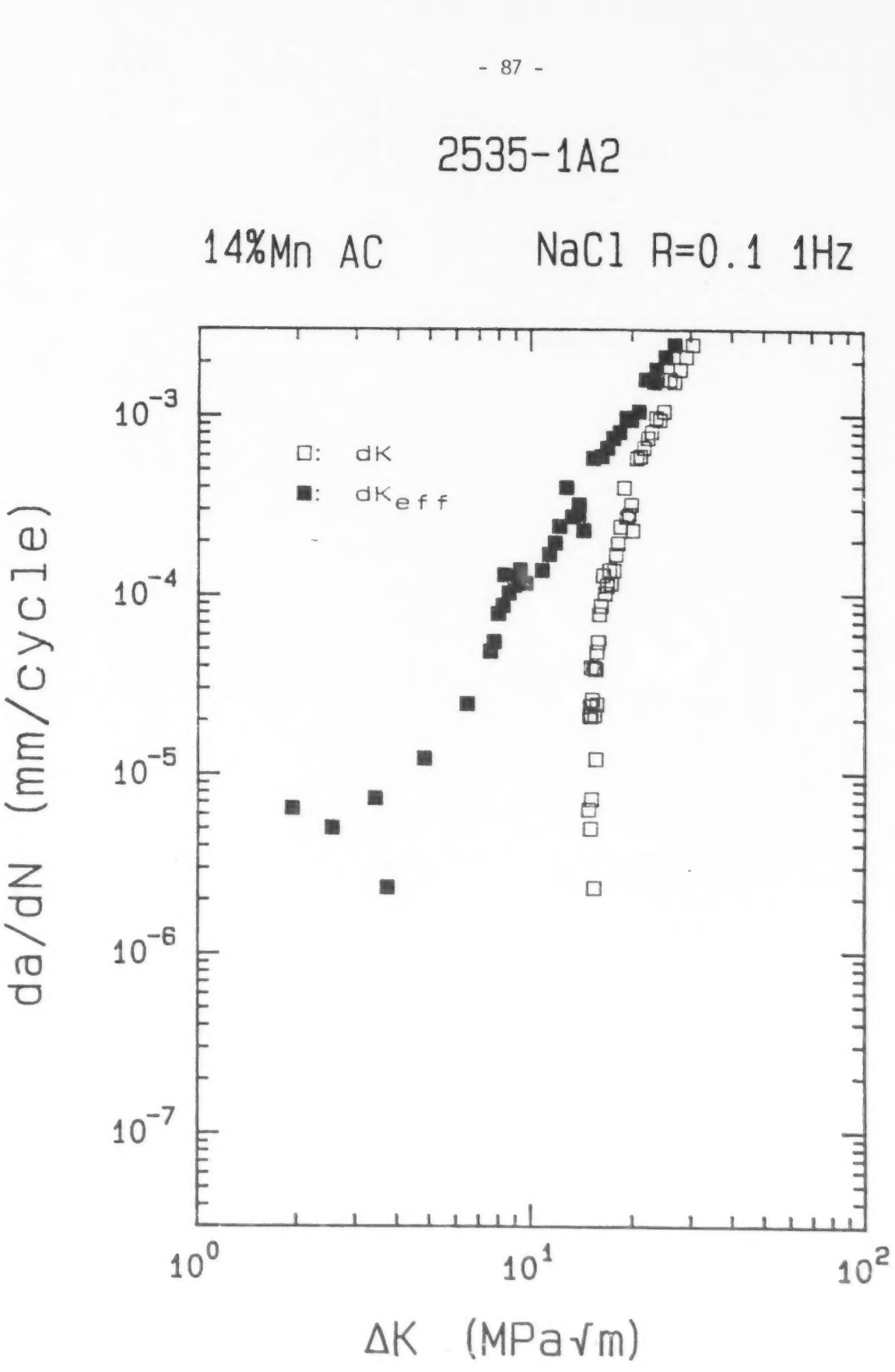
2535-1A2
14%Mn AC
NaCl R=0.1 1Hz
□: dK
■: dK eff
da/dN (mm/cycle)
10^-3
10^-4
10^-5
10^-6
10^-7
10^0
10^1
10^2
ΔK (MPa√m)

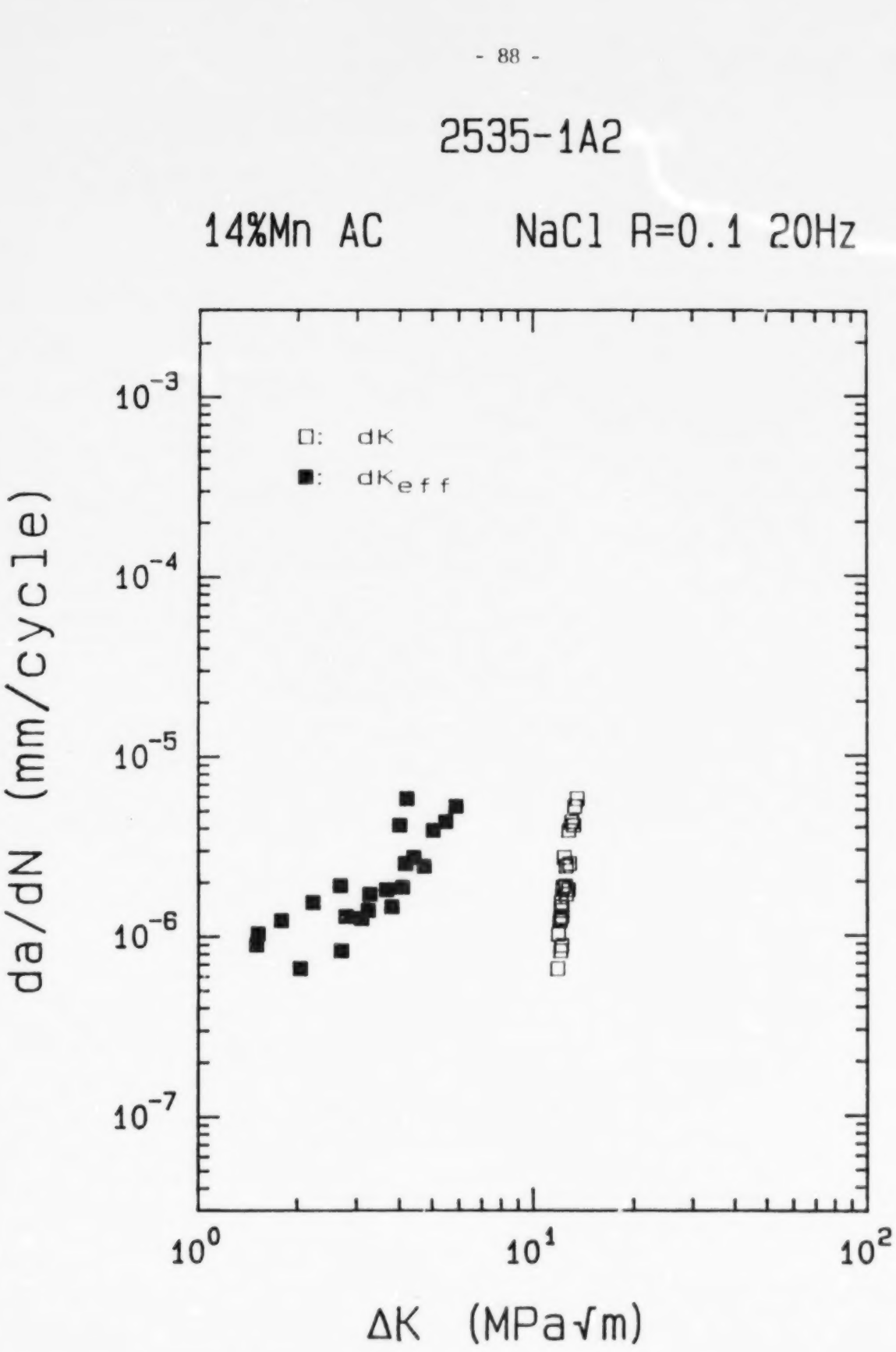
2535-1A2
14%Mn AC
NaCl R=0.1 20Hz
□: dK
■: dK eff
da/dN (mm/cycle)
10^-3
10^-4
10^-5
10^-6
10^-7
10^0
10^1
10^2
ΔK (MPa√m)

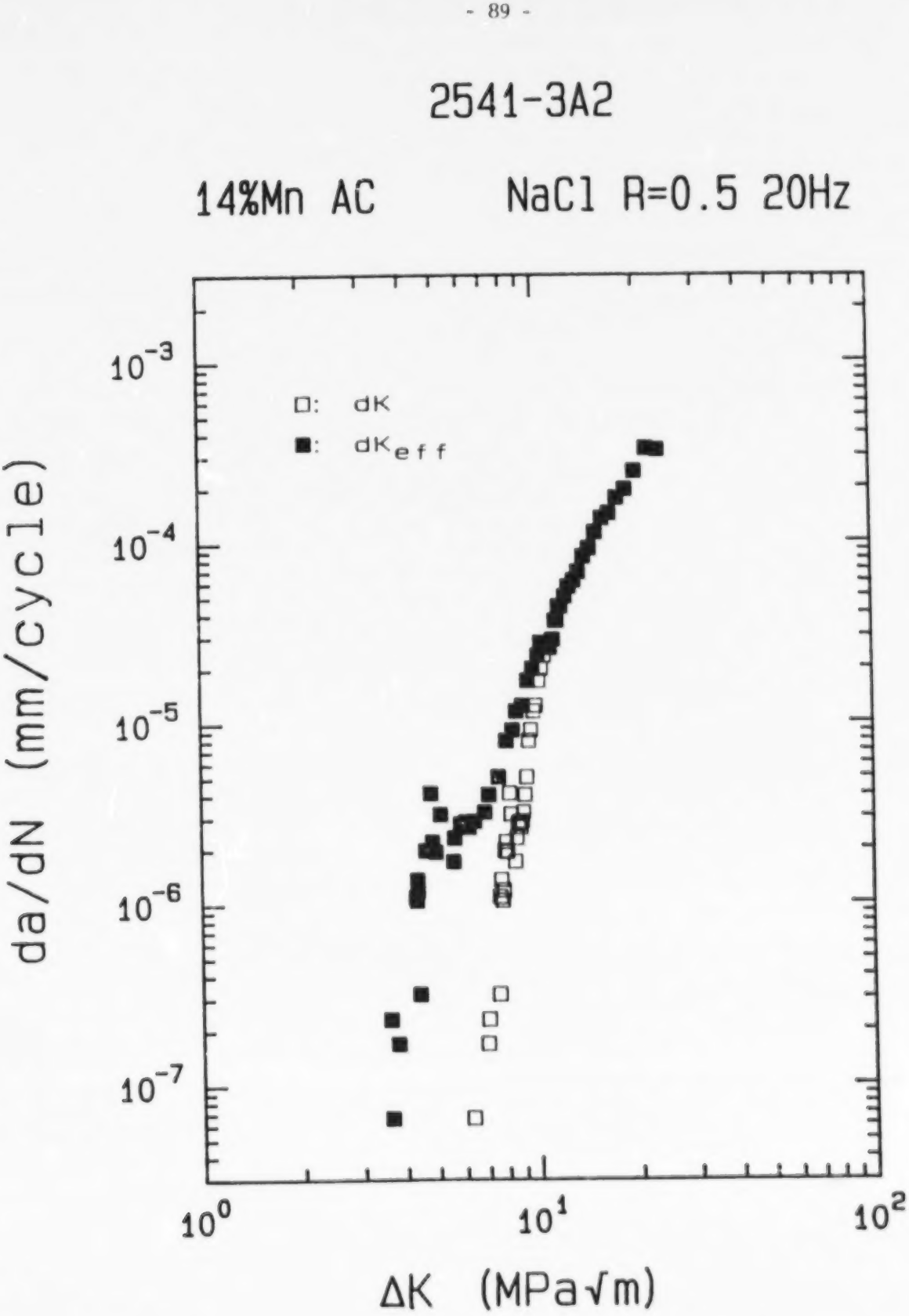
2541-3A2
14%Mn AC
NaCl R=0.5 20Hz
□: dK
■: dKeff
da/dN (mm/cycle)
10-3
10-4
10-5
10-6
10-7
100
101
102
ΔK (MPa√m)

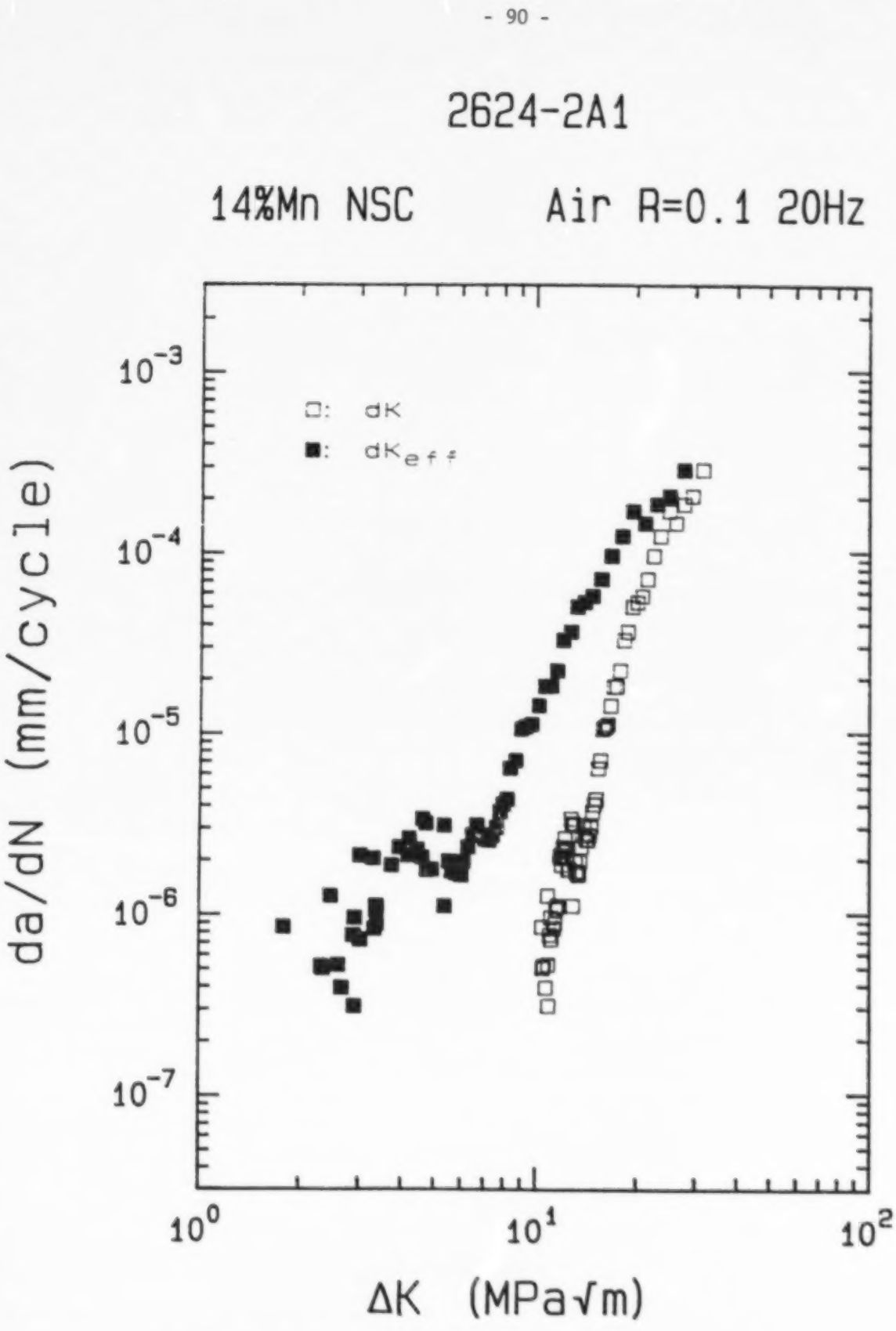
2624-2A1
14%Mn NSC
Air R=0.1 20Hz
□: dK
■: dK$_{eff}$
da/dN (mm/cycle)
10^{-3}
10^{-4}
10^{-5}
10^{-6}
10^{-7}
10^{0}
10^{1}
10^{2}
ΔK (MPa√m)

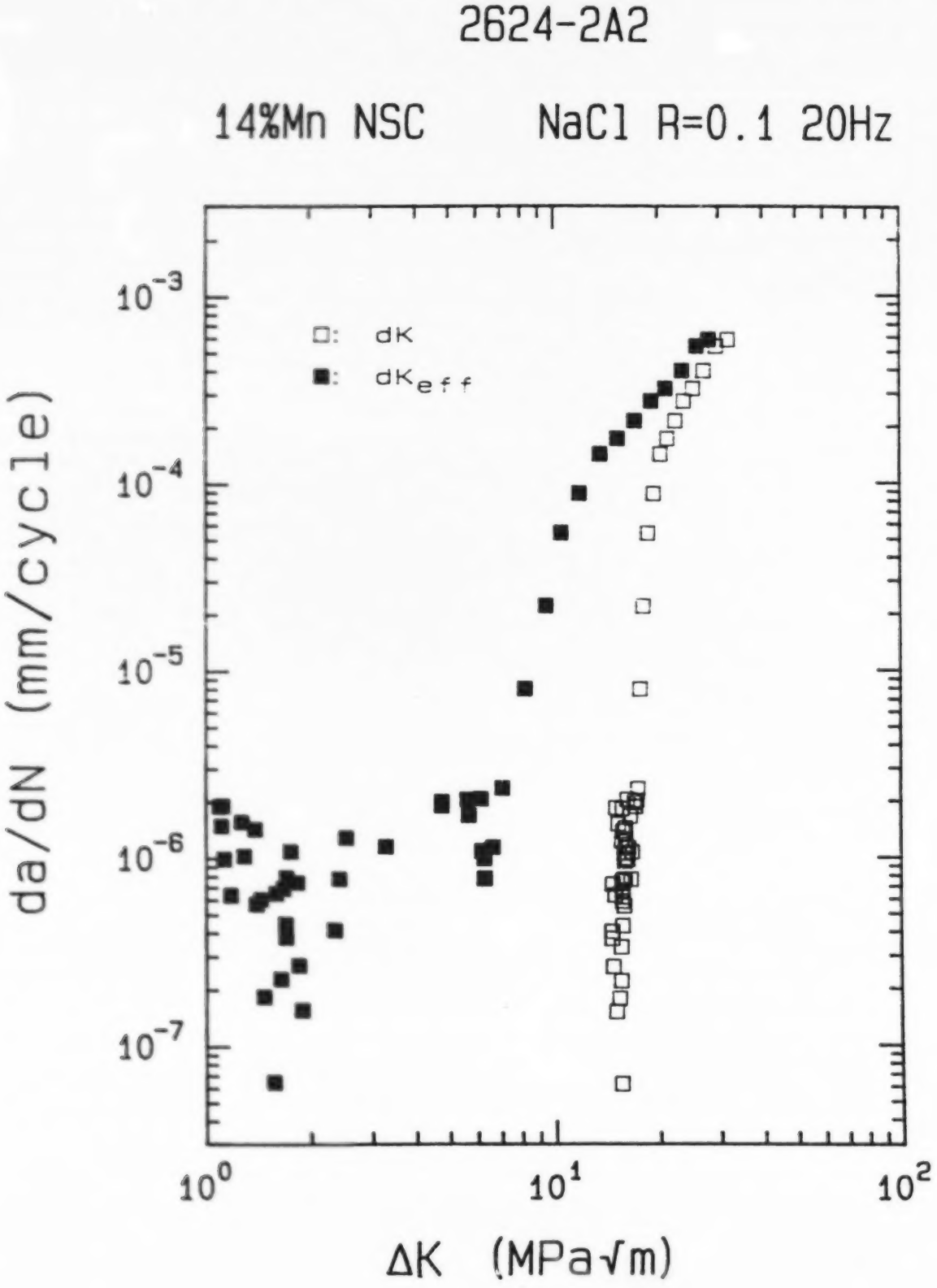
2624-2A2
14%Mn NSC NaCl R=0.1 20Hz
□: dK
■: dK eff
da/dN (mm/cycle)
10^-3
10^-4
10^-5
10^-6
10^-7
10^0
10^1
10^2
ΔK (MPa√m)

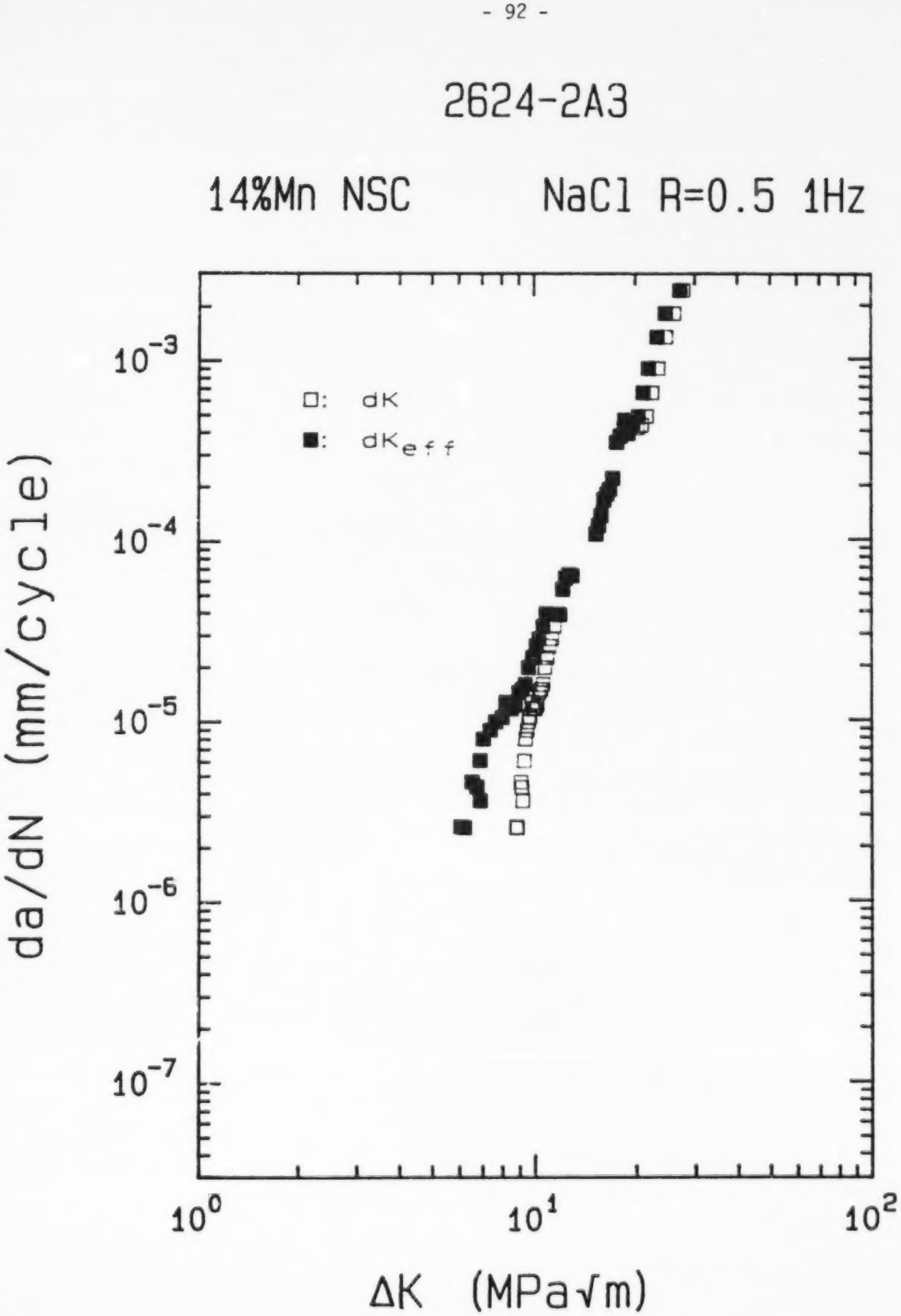
2624-2A3
14%Mn NSC
NaCl R=0.5 1Hz
□: dK
■: dK$_{eff}$
da/dN (mm/cycle)
10^{-3}
10^{-4}
10^{-5}
10^{-6}
10^{-7}
10^{0}
10^{1}
10^{2}
ΔK (MPa√m)

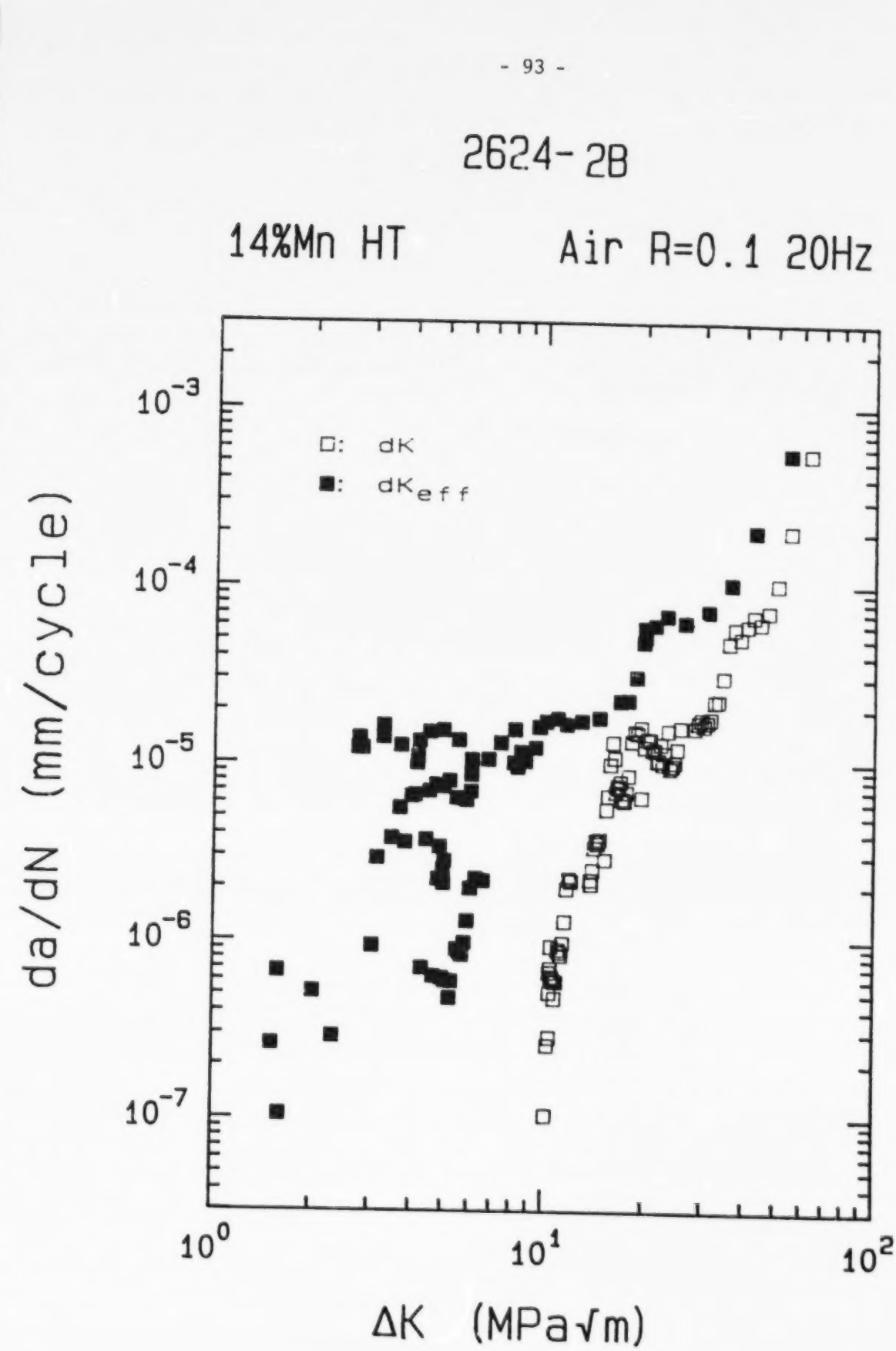
2624-2B
14%Mn HT
Air R=0.1 20Hz
□: dK
■: dK eff
da/dN (mm/cycle)
10^-3
10^-4
10^-5
10^-6
10^-7
10^0
10^1
10^2
ΔK (MPa√m)

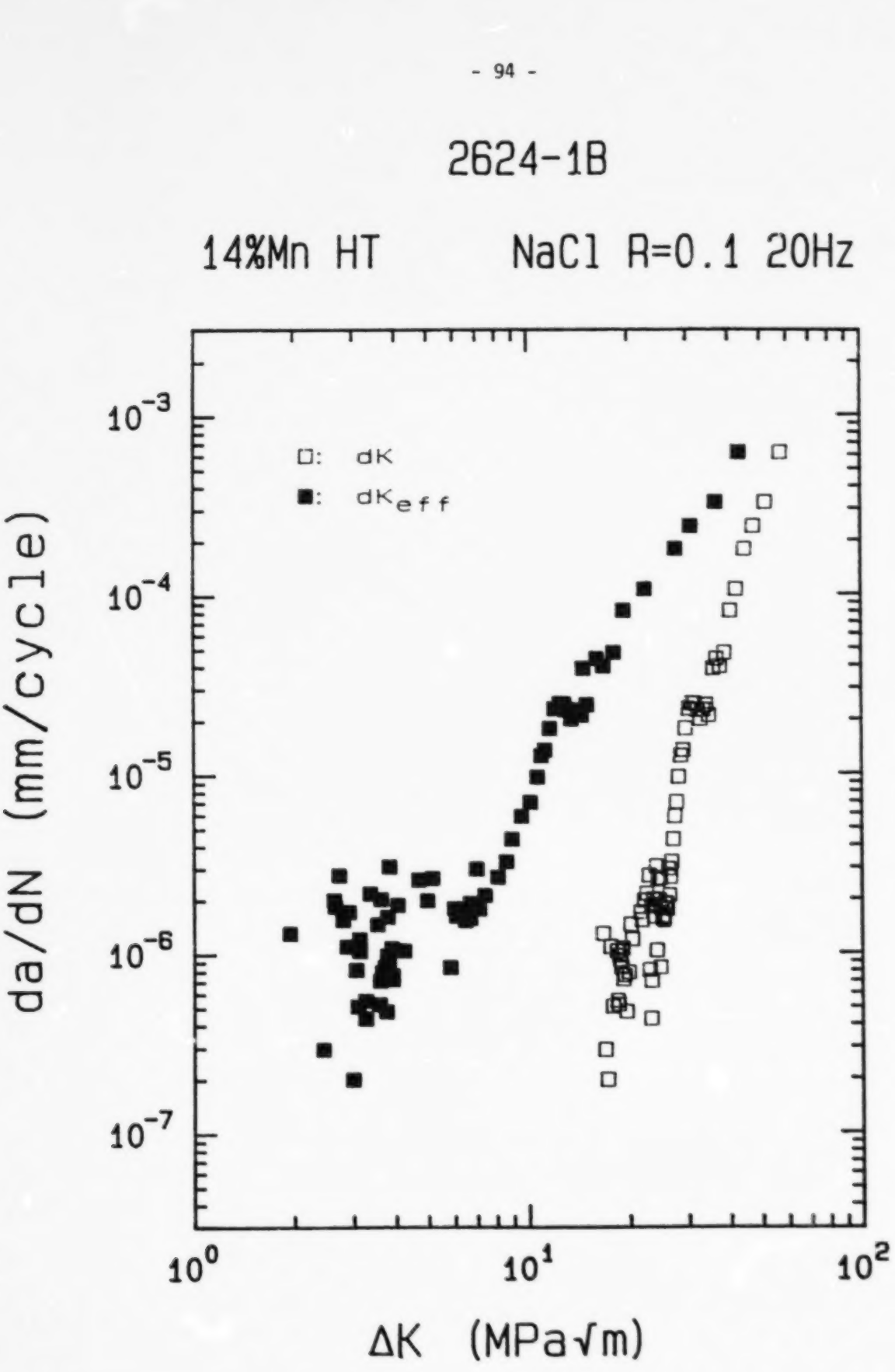
2624-1B
14%Mn HT
NaCl R=0.1 20Hz
□: dK
■: dK$_{eff}$
da/dN (mm/cycle)
10^{-3}
10^{-4}
10^{-5}
10^{-6}
10^{-7}
10^{0}
10^{1}
10^{2}
ΔK (MPa√m)

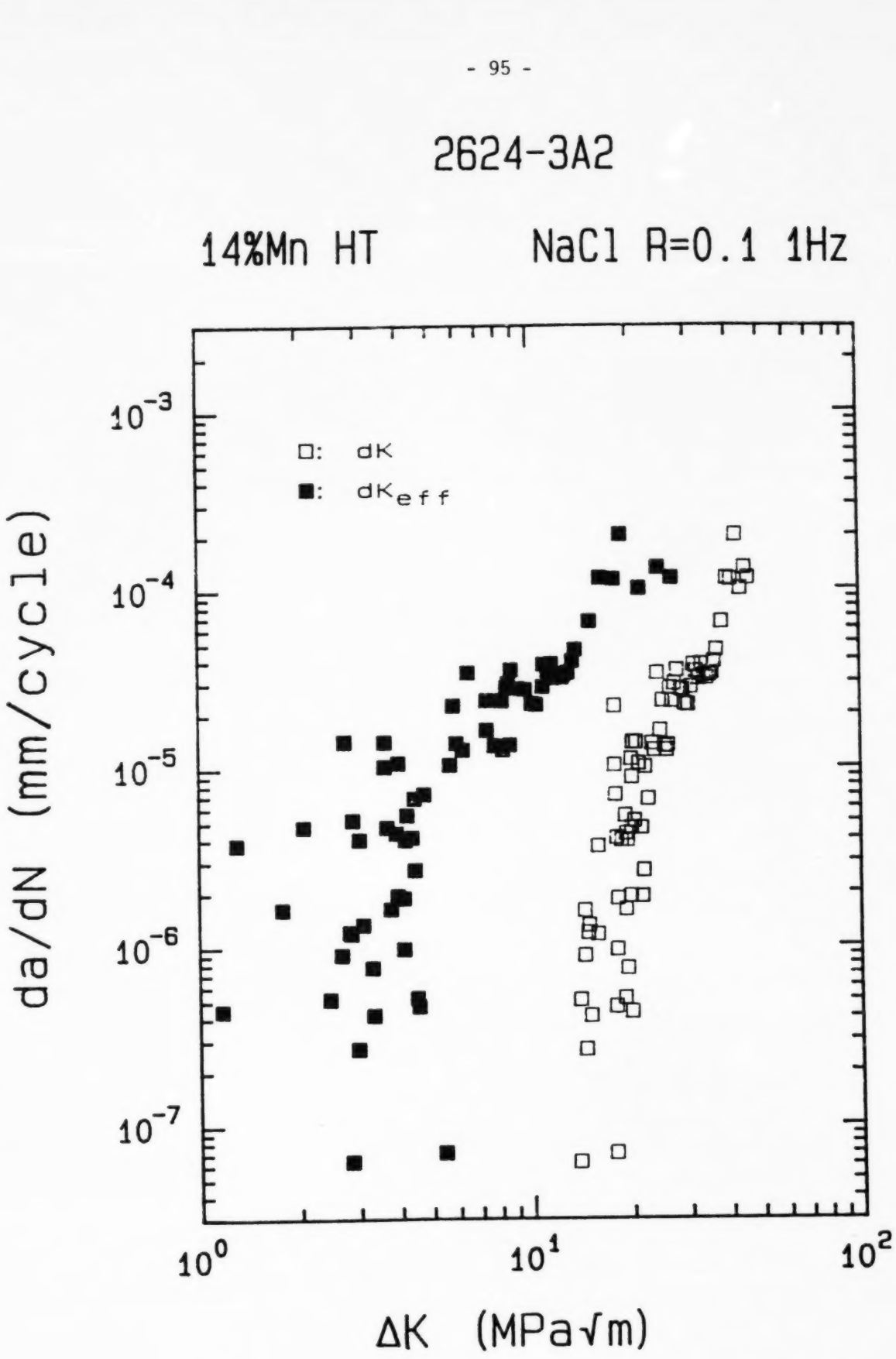
2624-3A2
14%Mn HT
NaCl R=0.1 1Hz
□: dK
■: dK eff
da/dN (mm/cycle)
10^-3
10^-4
10^-5
10^-6
10^-7
10^0
10^1
10^2
ΔK (MPa√m)

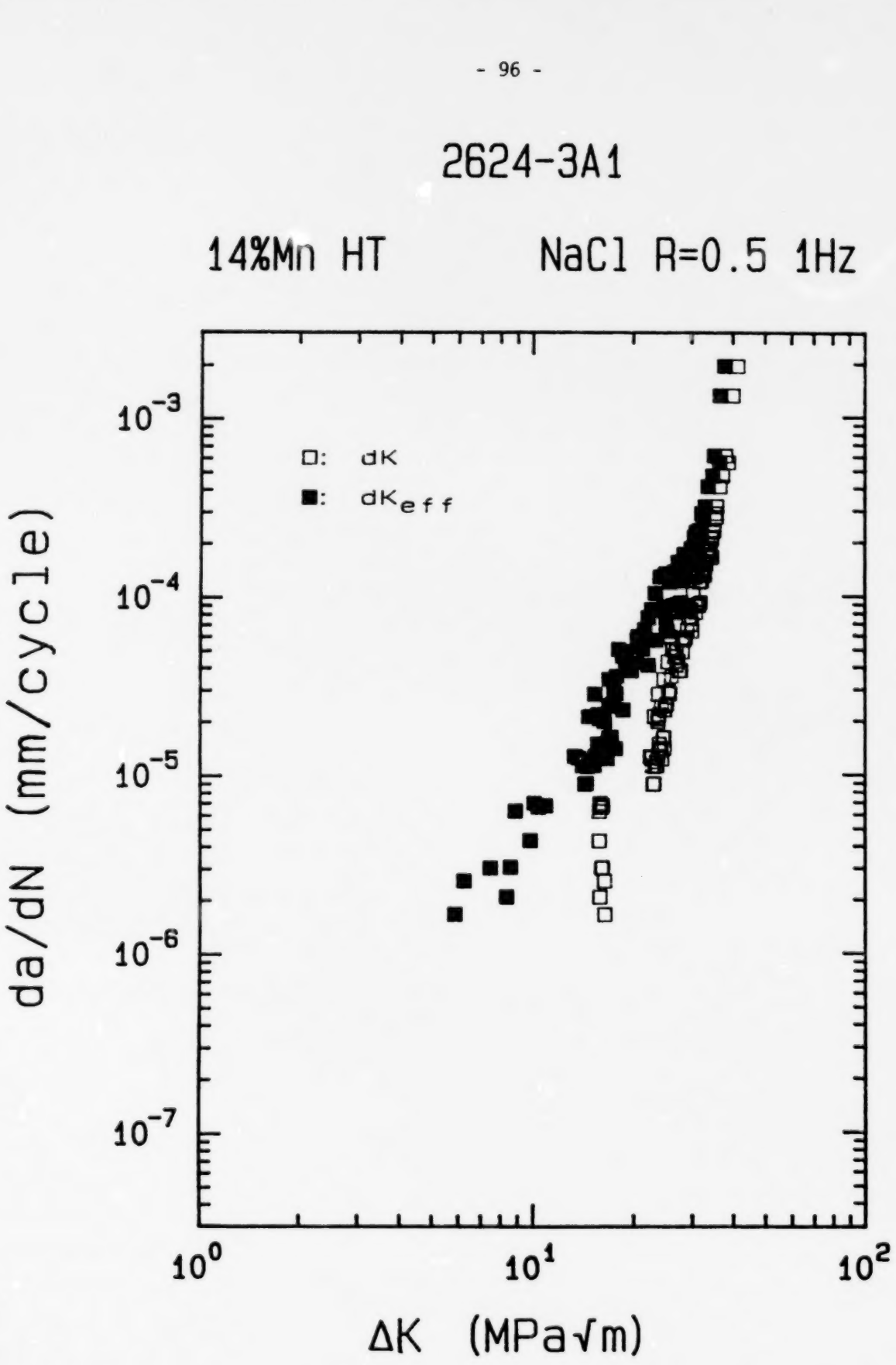
2624-3A1
14%Mn HT
NaCl R=0.5 1Hz
□: dK
■: dK eff
da/dN (mm/cycle)
10-3
10-4
10-5
10-6
10-7
100
101
102
ΔK (MPa√m)